Università degli Studi di Firenze
Scuola di Ingegneria
DIEF - Department of Industrial Engineering of Florence

PhD School: *Energetica e Tecnologie Industriali ed Ambientali Innovative*
Scientific Area: ING-IND/08 - *Macchine a Fluido*

On the modelling of liquid fuel ignition and atomization in aero engine combustors

PhD Candidate: Ing. Lorenzo Palanti

Tutor: Dr. Ing. Antonio Andreini
Co-Tutor: Prof. Ing. Bruno Facchini
PhD School Coordinator: Prof. Ing. Giampaolo Manfrida

XXXIII PhD School Cycle - 2017-2020

@ Università degli Studi di Firenze – Faculty of Engineering
Via di Santa Marta, 3, 50139 Firenze, Italy.

Tutti i diritti riservati. Nessuna parte del testo può essere riprodotta o trasmessa in qualsiasi forma o con qualsiasi mezzo, elettronico o meccanico, incluso le fotocopie, la trasmissione fac simile, la registrazione, il riadattamento o l' uso di qualsiasi sistema di immagazzinamento e recupero di informazioni, senza il permesso scritto dell' editore.

All rights reserved. No part of the publication may be reproduced in any form by print, photoprint, microfilm, electronic or any other means without written permission from the publisher.

A Lisa, soprattutto.
E a Lucia, Stefano e Niccolò.

... l'arte di scriver storie sta nel saper tirar fuori da quel nulla che si è capito della vita tutto il resto; ma finita la pagina si riprende la vita e ci si accorge che quel che si sapeva è proprio un nulla.
(Italo Calvino - Il cavaliere inestistente)

Acknowledgements

La scrittura dei ringraziamenti è indubbiamente una delle attività più temute nella stesura di una qualsivoglia tesi. E' un dato di fatto che solo alcuni lettori vi si soffermeranno, magari distrattamente, sperando di trovarvi qualche spunto che dia un volto, una umanità all'autore, prima di immergersi nella marea di sterili nozioni tecniche che seguono. La maggior parte, semplicemente, li ignorerà. Ad ogni modo non è per loro che queste poche parole anticipano il testo.

Paradossalmente, i ringraziamenti sono per coloro che la tesi mai la leggeranno: amici, parenti, colleghi... E' da lì che viene quella pressione, quell'ansia di non dimenticare nessuno, di riservare a tutti il giusto spazio, senza esagerare o essere troppo stringati. E magari di scrivere qualcosa di vagamente significativo, che susciti un'emozione, una sensazione a chi si prenderà la briga di leggerli tutti, o solo la parte in cui riconoscerà il proprio nome. E c'è quella brutta bestia dell'italiano, padroneggiato fino alla fine del liceo, ma ormai ridotto all'osso di una comunicazione giornaliera che avviene per frasi brevi, fatte e semplificate.

Allora stavolta mi prenderò il permesso di cercare di strappare un sorriso al lettore, senza badare troppo alla forma richiesta ad una tesi, puntando piuttosto alla sostanza, ai momenti e alle circostanze che mi legano alle persone che intendo ringraziare.

Inzio con le istituzioni: al Prof. Facchini vanno i miei ringraziamenti più sinceri per l'affetto paterno con cui gestisce i suoi dottorandi e collaboratori vari, incluso il sottoscritto. Una guida cordiale nelle avversità sceintifiche e, ahimè, burocratiche del dottorato. E grazie anche per le buonezze ai pranzi di Natale, sappia che ho sempre tanto apprezzato (e credo si sia notato).

Il ringraziamento successivo è per il Prof. Andreini, autentico faro tecnico nelle attività di questi tre anni e ineasuribile fonte di sapere su combustione, simulazioni e programmazione. Alla luce del rapporto attuale, mi fa sorridere pensare al timore che ci incutevi a lezione. Mai avuta tanta

strizza ad un esame! Sono già passati 4 anni, ma lo ricordo come se fosse ieri.
Per concludere il trittico dei supervisor, ringrazio il Prof. Demoulin per la quantità di idee vulcaniche con cui ha bombardato i miei giorni a Rouen, per i chiarimenti teorici e per le tante volte in cui mi ha incoraggiato, nonostante il mio pessimismo cosmico. E grazie anche per i consigli di enogastronomia francese.
Sempre in ambito universitario, desidero ringraziare un altro trittico, composto da tre figure chiave che, come guide sherpa (anche se un po' infami), mi hanno condotto nella scalata di questo monte chiamato PhD. A Stefano, storico relatore della tesi magistrale, compagno di bevute in Francia e amico vero. Grazie per i consigli (scientifici e non) e per avermi convinto ad affrontare questa impresa: nonostante mi piaccia sostenere il contrario, ne è valsa la pena. Un ringraziamento sentito anche a Davide e Lorenzo ("Mazze") per le innumerevoli verità tecniche e per le volte che avete subito i miei sproloqui.
Dato che non c'è due senza tre, i miei ringraziamenti più cari anche al terzo ed ultimo trittico di questo dottorato: i miei amichetti e compagni di corso Matteo, Tommaso e Simone. Al futuro rettore Matteo, un grazie di cuore per il supporto informatico h24, per gli infallibili consigli per gli acquisti e per aver lavorato (gratuitamente!) come mio chauffeur in innumerevoli occasioni. Solo una nota di demerito per quella volta che a correre... Grazie al buon Tommaso per la collaborazione numerico-sperimentale che ci ha fatto discutere, crescere e pubblicare. E che risate a Poitiers con quello squilibrato di Arun! Infine, la vera scoperta di questo PhD: Simone. Da quel momento in cui eri il tipo taciturno e un po' sfavato nell'angolo del LDCF sono passate innumerevoli serate, nuove conoscenze e una vacanza indimenticabile. Te lo prometto, finito questo maledett pandemia, torneremo a farci chiamare dai carabinieri. Tutti e tre, ormai, siete amici veri.
E per concludere con i ringraziamenti in ambito accademico, vorrei ringraziare gli altri compagni di avventura, attuali ed ex-membri della grande famiglia chiamata HTC-group. Tutto l'ufficio B, che non è un luogo, ma uno state of mind: Leonardo ("il lamento"), Alberto ("una mezz'ora fatta bene") e Andrea. Se c'è una cosa che lo smart-working mi ha insegnato, è che con delle persone così si vive meglio (e si lavora meno). E poi un grazie a tutti gli altri che sono sempre stati lì per un consiglio, due parole di incoraggiamento o banalmente per giudicarmi severamente durante un'abbuffata: Lorenzo Cocchi, Sabrina, Tommaso Fondelli, Carlo Carcasci, Carlo Alberto, Piercarlo, Tommaso Diurno e Daniele. E poi un ringraziamento e un grande in bocca al lupo a Matteo Amerighi, tesista,

probabile erede e imprescindibile aiuto negli ultimi giorni di dottorato.
Fuori dall'ambito accademico, devo ringraziare gli amici di sempre. Testimoni di momenti imbarazzanti, di tassi alcolemici illegali e di acconciature rivedibili. Persone che ci sono da sempre e che a volte ti mancano da paura. Qualcuno è più vicino, qualcuno, a breve, sarà più (troppo!) lontano. Ma la nostra amicizia è come quel maledetto FIFA a cui non giochiamo da un pezzo: è più vecchia, più polverosa e noi siamo sempre più impediti. Ma certi automatismi non li perdi mai. E quindi un gigantesco grazie ad Ando, Torro e Mugno. In questi tre anni ci siamo laureati e abbiamo iniziato a lavorare; qualcuno si è sposato e tutti siamo andati a convivere. Ma quello che ci lega va oltre le distanze, gli impegni e le responsabilità.
Le penultime persone da ringraziare, come da buona tradizione sono i genitori e gli eventuali fratelli/sorelle. Perché sono coloro che ti hanno pagato gli studi e loro malgrado hanno sopportato i tuoi scleri pre-esame (insieme al soggetto tradizionalmente lasciato per ultimo nei ringraziamenti). Ma non solo: sono coloro che ti hanno plasmato, cresciuto e (ahilorò!) nutrito. E son sempre coloro che, nonstante tu sia ormai prossimo ai trenta, cercano di guidarti nella tua vita, a volte con consigli opinabili, a volte palesemente sbagliati, ma comunque sempre e solo per il tuo bene. E quindi un grande abbraccio alla Mamma e al Babbo, per tutto. E un abbraccio anche a Niccolò, seguito o preceduto da un nocchino, come preferisci.
E infine, il ringraziamento più grande è per Lisa, detta "Pollo Verde" all'epoca della stesura di questa tesi, al secolo "Ouizzi" più altri stupidi nomignoli che ormai ci siamo scordati. Com'è noto, ringraziare la propria ragazza, scadendo nel banale di frasi fatte, trite e ritrite, è più semplice che far scoppiare Fluent. Cioè dannatamente semplice. E dato che questo errore l'ho già fatto in altre due tesi, inanellando parole inutili e concetti vaghi, cercherò a questo giro di buttarla sul semplice. Ti ringrazio per avermi cucinato tutti quei manicaretti: grazie a loro hai reso affrontabile il PhD, la breve ma non banale ricerca di un nuovo lavoro e questi stramaledetti lockdown. Perché lo sai che a pancia piena vivo meglio. E poi ti ringrazio anche per tutte le cene fuori, le vacanze e le gite fuoriporta: perché quando siamo a zonzo io e te si sta bene. E infine grazie per supportarmi sempre, senza riserve, in tutte le fittonate e le attività stupide che intraprendo. E anche nelle cose serie, che con il tuo "anatemino" non possono andar male. Ti voglio bene.
E ora che i ringraziamenti sono finiti, veniamo al sodo. Caro lettore, buona lettura!

Abstract

A fast and reliable relight of aero engines burners is one of the most critical points to ensure aircraft safety. The so-called altitude relight is the process that allows the combustor to be re-ignited after a flame-out during flight. Several expensive tests must be carried out to obtain the required certifications, which makes important to fully understand the problem of the flame onset. To speedup the design process, Computational Fluid Dynamics established as valid alternative to the experiments to investigate the complex phenomena involved in the ignition process.
In this work, a fully reactive Large Eddy Simulation of the ignition process is attempted with the aim of validating the setup for future applications within an advanced design process. In this line, a throughout validation is carried out against some detailed experimental results of a lean spray flame. At first, a non-reactive and reactive simulations are carried out to validate the cold flow field and the stabilized flame structure. Then, an ignition simulation is performed, from initial spark deposition up to flame stabilization. The obtained results are extensively compared with the available experimental data, showing that the employed simulation setup can describe quite well the phenomena involved in the rig ignition. However, this procedure does not allow to perform statistical studies, such as the optimization of the igniter position. This issue is critical since it can help to minimize the amount of energy required for ignition and to increase the durability of the hardware. In fact, several spark discharges must be simulated for each position, to account for different realizations due to the turbulent flow field. Therefore, the previous Large Eddy Simulation approach is not feasible in this scenario, due to the excessive computational effort. In scientific literature, specific low-order models were developed to provide an affordable estimation of the local ignition probability. Due to the large amount of assumptions they clearly sacrifice part of the accuracy and of the physical consistency, but the short turnaround time makes them the first choice at low Technology Readiness

Level. In this thesis, a low-order design model is implemented and used to investigate the ignition probability of the same test rig simulated in detail, showing that it can provide good results if a careful sensitivity study is firstly conducted. This set of simulations represents a first attempt in the scientific literature to carefully validate a low-order model using a flow-field from LES and very accurate experimental data. Moreover, the LES of the ignition process is used to further validate the model and highlight its main shortcomings. To the best of the author knowledge, such in-depth validation was not attempted so far.
The last step of the thesis concerns the development of a simulation and post-processing methodology to investigate the primary breakup of the spray in altitude relight conditions. Such activity is motivated by the fundamental importance of spray initialization in full chamber simulations. In fact, due to the very poor atomization quality and the negligible evaporation process, the droplets ejected from the nozzle can travel all along the combustion chamber and finally reach the combustor walls. Under these conditions, the ignition tools already described might fail if the spray is injected with a wrong distribution. Therefore, a tentative approach to evaluate the spray size distribution is proposed in the last section of this work. It is based on a run-time evaluation of distributed variables such as liquid/gas density of interface or locally defined variables as the curvature of the interface. In the present work, the Eulerian Lagrangian Spray Atomization model is used as a basis to test such technique. An academic planar prefilmer configuration is selected to evaluate the accuracy of the post-processing, thanks to the availability of experimental measurements in the proximity of the injector. The reported results include a brief description of the simulated liquid structures, the predicted Sauter Mean Diameter, the evolution of interface curvature and a final proposal to derive the spray size distribution. The novelty of this last section is mainly represented by the use of the interface curvature to analyze and postprocess the primary breakup. At the best of the author knowledge, this is the first time that such an approach is attempted to an actual atomizing device.
Overall, the aim of this work is to validate and to develop a set of tools to improve altitude relight design in aero engines. Although much work is still needed, this thesis represent a first step towards the use of more advanced numerical tools to optimize this process and to more easily meet the required certifications.

Contents

List of Figures

List of Tables

Nomenclature

Acronyms

ARC	Analytically Reduced Chemistry
ATF	Artificially Thickened Flame
CFD	Computational Fluid Dynamics
CS-E	Certification Specifications for Engines
Dof	Depth of Field
DNS	Direct Numerical Simulation
EASA	European Union Aviation Safety Agency
ELSA	Eulerian-Lagrangian Spray Atomization
ED	Energy Deposition
HIT	Homogeneous Isotropic Turbulence
HS	High-Speed
HS-PIV	High-Speed Particle Image Velocimetry
ICM	Interface Capturing Method
IRQ	Interface Resolved Quality
IRZ	Inner Recirculation Zone
ITS	Institut für Thermische Strömungsmaschines
KIAI	Knowledge for Ignition, Acoustics and Instabilities
KIT	Karlsruhe Institute of Technology
LDI	Lean Direct Injection
LIMIT	Lagrangian Ignition Map using Inverse Time
LES	Large Eddy Simulation
MIE	Minimum Ignition Energy
MIST	Model for Ignition STatistics
NDF	Number Density Function
NSE	Navier-Stokes Equations
OH-PLIF	Planar Laser Induced Fluorescence on OH
ORZ	Outer Recirculation Zone
PDA	Perfectly Stirred Reactors
PEA	Partial Equilibrium Assumption
PSR	Perfectly Stirred Reactors
RANS	Reynolds Averaged Navier Stokes

RQL	Rich-Quench Lean
SBES	Stress-Blended Eddy Simulations
SCD	Surface Curvature Distribution
SMD	Sauter Mean Diameter
SJZ	Swirled Jet Zone
SOPRANO	Soot Processes and Radiation in Aeronautical innovative combustors
SPH	Smoothed Particle Hydrodynamics
SRS	Scale-Resolving Simulation
SST	Shear Stress Transport
TFM	Thickened Flame Model
Toluene-PLIF	Planar Laser Induced Fluorescence on Toluene
UDFs	User Defined Functions
URANS	Unsteady RANS
USAXS	Ultra Small Angle X-ray Scattering
VoF	Volume of Fluid
WALE	Wall-Adapting Local-Eddy viscosity

Introduction

Before introducing the problem of the ignition in aero engine, it is worth recalling the most common architectures of burners, used in modern turbofan. During the last decades, the main challenge related to combustor design was the reduction of the pollutant emissions, in particular the one of NO_x. The most relevant mechanism of NO_x production is the so-called *Zeldovich mechanism* which has an exponential dependence from temperature. It should be remembered that the maximum combustion temperature is usually achieved for a mixture close to stoichiometry. Hence, to avoid such condition, two main burner configurations have been developed and are currently in use (Fig. 1):

- *Rich Quench Lean* (RQL) burners are characterized by a rich burning primary zone close to the injector, which ensures a very stable flame anchoring. The passage from rich to lean conditions is achieved through the controlled introduction of air down the length of the combustor, in order to produce a mixture rich of oxygen to complete the combustion process. The rich zone ensures low NO_x emissions because of the low temperature and oxygen concentration, while the sudden addition of secondary air moves the mixture towards a lean combustion, which is again characterized by low pollutant emissions. Anyway, it is really difficult to completely avoid the local creation of stoichiometric conditions and therefore a particular attention must to be devoted to make the quench as fast as possible.

- *Lean burn combustors* were originally designed for heavy-duty gas turbines, where the reduction of NO_x is achieved burning a mixture with a low equivalence ratio. In lean conditions, the relatively low temperature ensures the containment of the pollutant emissions. Among lean burn combustion concepts, an established technique to obtain an efficient mixing between air and fuel is the Lean Premixed Pre-vaporized system. This technology represents the actual

standard in ground-based gas turbines. Here, the fuel is completely evaporated and homogeneously mixed with air before being injected into the combustion chamber. However, the high operating pressure of typical aero engine combustors, strongly increases the risk of flashback, with excessive safety risks. Thus, in the aeronautical context the attention moved to direct injection systems, called *Lean Direct Injection* (LDI), where the liquid fuel is directly injected into the combustion chamber.

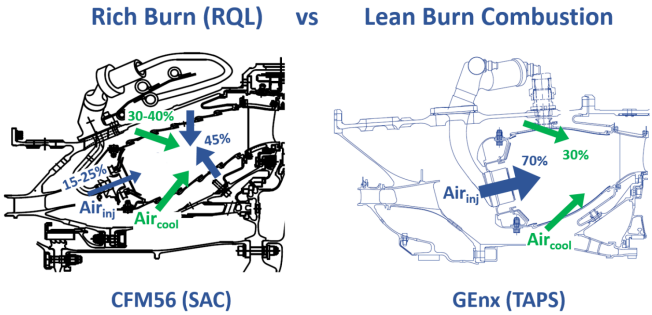

Figure 1: Comparison between LDI and RQL combustor architecture [1].

The ignition of such devices is clearly subject to certifications: in the *Certification Specifications for Engines* (CS-E) issued by the *European Union Aviation Safety Agency* (EASA) the problem of altitude relight in turbojet and turbofan engines is the object of a specific section (910). It states that "*the Engine constructor must recommend an envelope of conditions for Engine relighting in flight, and must substantiate it by appropriate tests or other evidence. The recommendation must state all the conditions applicable, e.g., altitude, air speed, Engine windmilling rotational speed, whether starter assistance is required, the recommended drill*"[2]. It is worth noting that the CS-E 910 been recently integrated with some of the specifications from an *Acceptable Means of Compliance* document that specifies how the certification must be issued. In short it states that either "*engine altitude testing or engine flight testing are considered to be acceptable means of demonstrating compliance*"[3] which states that altitude testing are strictly required to certify the engine before the entry into service.
The concept of envelope is introduced by the present certification: it

is defined as the range of conditions in which the engine manufacturer certifies that the engine can be relighted. A typical relight envelope of an annular combustor is reported in Fig. 2: It is important to note that

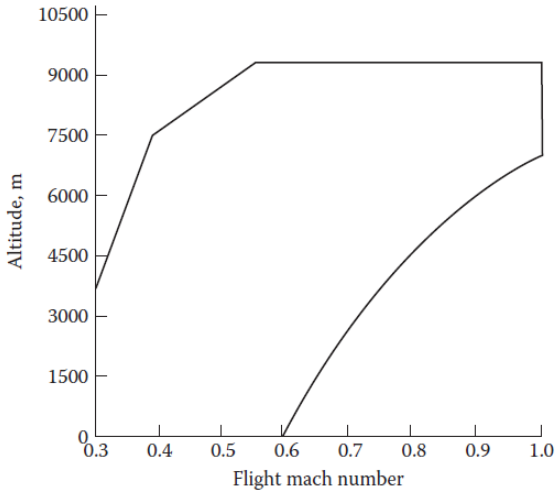

Figure 2: Typical altitude relight curve of a annular combustor [4].

ground starting is always accomplished by making the compressor and the turbine rotate with a starter device (which may differ among different types of engine). Instead, the in-flight restart is usually achieved thanks to the auto-rotation of the engine induced by the air flowing through the gas turbine [5], called *windmilling*. This explains the need of specifying the flight Mach number in the horizontal axis. Instead, the varying altitude (vertical axis) substantiates the external conditions in terms of pressure and temperature. As it will be shown later, the lower the pressure the worst the atomization process. Similarly, a low temperature mitigates the evaporation process providing less and less fuel vapour to intiate the combustion.

According to the EASA [3], recent design trends such as the growth of the *Bypass Ratio* may increase the air speed to ensure windmilling. Similarly, the aforementioned LDI technology [6] and the interest towards alternative fuels [7] may hinder the ignition process, possibly further reducing the area of this envelope. Clearly, this not only depends on the combustor design, but it is also affected by the global architecture of the machine which is not discussed here for the sake of brevity. However, this brief overview of

required certifications easily explains the interest on ignition by engine manufacturer. In fact, a proper design of the combustion chamber, of the liquid fuel injection system and or the ignition system are fundamental to accomplish the required certification.

Aim of the work

It should be clear by now the primary importance of tools to improve the design of the combustion chamber with respect to the altitude relight performances. In this context, the use of numerical tools gained more and more importance in the last years, as they reduce the time and the costs needed to set up experiments. As already pointed out before, experimental tests are still needed for the final certification of the engine, but simulations represent nowadays an essential tool to speed-up the design process. Moreover, they can help to gain a deeper insight on the complex physical phenomena that may take place during the simulated process which may also help in the design of a component. Hence, this works aim at developing and validating numerical approaches to improve the altitude relight performances. A large amount of numerical tools could be considered to this purpose, although here the attention is limited to the *Computational Fluid Dynamic* (CFD).

Outline of the thesis

A consistent part of this work is devoted to the study of the flame development within the ignition under atmospheric conditions process. To this purpose, two existing simulation techniques are tested and validated. The obtained results show that they are ready to provide important insights on the process of ignition under atmospheric conditions. But once the the focus is shifted towards altitude relight, the approach used to take the spray into account may not be reliable. Therefore, a novel method to investigate the initial evolution of the liquid fuel inside the combustion chamber is developed as well.
The thesis is structured as follows:

- **Chapter 1** deals with the problem of the detailed simulation of the ignition in gas turbines. At first, the main steps that lead to flame relight are described, so that the reader may familiarize with all the elements involved in such process. Then, the issue is tackled from a numerical perspective, by highlighting the governing equations and the models that are employed in this work.

- **Chapter 2** addresses a further step to be considered in the improvement of the ignition performances, namely the computation of the ignition probability. In fact, the ignition in gas turbines is not always successful and the first part of this chapter is devoted to explain the the main sources of stochasticity and the possible modes of failure. Keeping that in mind, the existing models to compute the ignition probability are revised: even if many of them are currently available, only one is selected for implementation in this thesis. After that, some further explanations on this model are provided along some details of its implementation into a commercial software.

- **Chapter 3** introduces the first test case studied in this work: it consists of a lean spray flame operated under atmospheric conditions. The models presented in the previous two chapters are applied and validated against the large amount of experimental data available. The reported results highlight that the employed tools are accurate enough to be used during the design process, if atmospheric pressure is of interest.

- **Chapter 4** starts with a practical example to point out the importance of the atomization process under altitude relight conditions. After this short statement, the phenomenology of the atomization process is briefly described. Then, a recent publication is reviewed to further stress the motivation of studying primary breakup when the altitude relight is considered.

- **Chapter 5** reports the development of a novel approach to post-process primary breakup simulations. The aim of this chapter is to propose an alternative method to analyze the atomization process based on locally distributed variables. The validation of the approach is carried out considering a prefilmer atomizer, demonstrating that it may constitute a promising tool to improve altitude relight simulations.

In the last chapter, some conclusions about this research are drawn along with some recommendations for future works.

Chapter 1

Modelling the ignition process in gas turbines

In this chapter, the problem of the detailed modelling of the ignition process is discussed. The purpose is to show the set of equations and models that are used in simulations, whereas the additional problem of computing the ignition probability (that will be defined later) is left to the next sections of this thesis.
At first, the phenomena involved in the forced ignition of spray flames are briefly introduced. Some main steps are identified in scientific literature and each one of them is shortly described.
Later, a first set of governing equations are presented: *Navier-Stokes Equations* (NSE) are provided for a multi-species reacting flow, firstly without including the spray and the ignition modelling. The direct solution of these equations is not feasible and the filtering procedure is introduced to move into more convenient LES framework.
The several unclosed terms and the additional source terms (used for the combustion process, the spray and the spark) require a large modelling effort. Therefore, a large attention is devoted to discuss these additional models required for ignition simulations.
At the end of this chapter, the reader should have a clear picture of the solved set of governing equations, to better appreciate the results of the simulations presented in the following of this work.

1.1 Forced ignition of spray flames

The term *forced ignition* is used to indicate the initiation and the following establishment of the combustion process after that an external source provides some initial amount of energy or radical species (or both) [8]. Such external source may be an electrical or laser-induced spark, a plasma jet or a heated surface. For the sake of brevity, the discussion here is limited to spray ignition, but many fundamentals processes are also the base for solid [9] and gaseous [10] fuels.
It is important not confuse the forced ignition with the so-called autoignition [11, 12]: it commonly refers to the process where the fuel or the oxidizer (or both) are at such high initial temperature that chemical reactions can start without any external source of energy. Instead, in the forced ignition, the chemical composition is basically frozen before the spark is released and only after that the combustion proceeds autonomously (once that spark is removed).
The forced ignition is conventionally divided into three steps, involving different time and spatial scales and physical processes [4, 8, 10]. The boundaries between these stages are not uniquely defined, but they can be roughly divided into:

- kernel generation,
- flame growth,
- burner-scale flame establishment.

These three phases are briefly described in the next sections, since they are of interest in the present work. Another phase must be considered in annular and linear combustors: the light-around. It consists of the flame propagation from the first ignited burner up to the whole combustion chamber and is clearly of interest of multiple burners only [8]. Such final phase is not considered in this thesis and also its description is omitted for the sake of brevity. Moreover, the ignition process is largely stochastic due to many influencing parameters. In the next, the description is kept as deterministic as possible, assuming that all the steps are successful. In reality, might fail for many reasons, which are detailed in Ch. 2 where the concept of ignition probability is introduced.

1.1.1 Kernel generation

The kernel generation is the first phase of ignition and it is one of the fundamental problems in combustion [8]. A flammable mixture can be

ignited if a enough energy is released to raise the temperature of a region, with approximately the size of the laminar flame thickness, above the adiabatic flame temperature [13]. The minimum ignition to accomplish that is called *Minimum Ignition Energy* (MIE). If electrical sparks are considered, they tend to last for a relatively long time (hundreds of μs or ms) and the kernel may significantly interact with the flow before the source of energy is stopped [14]. This introduces additional uncertainties regarding spark modelling in simulations that are not fully addressed yet. Conversely, laser-induced sparks have a shorter duration (usually ns) and a smaller and more controlled kernel is generated when the laser stops [15]. The main modelling issue resides in the generation of some amount of plasma, which involves chemical species that are usually not accounted in standard reaction mechanisms. This issue is usually tackled by neglecting the plasma phase, as it will be shown later, although some authors attempted to simulate this stage as well [16] in gaseous mixtures. The spark deposition is usually followed by a shock wave [8], which is normally not strong enough to cause autoignition, but can trigger the breakup of droplets [17]. This is particularly interesting in altitude relight conditions: in fact, as it will be shown in Ch. 4, a very poor atomization quality must be expected and such shock wave may improve the ignition performances. Shock waves and heat loss phenomena are not normally included in simulations, which explains why a lower amount of energy is normally used [18]. A successful ignition implies that enough energy is provided to the flow to promote spray evaporation and initiate the combustion. If so, after the deposition of energy, a small kernel of hot gases will be found in the spark place, normally leading to the second phase.

1.1.2 Flame growth

While most of the processes involved in the first stage of kernel generation are usually overlooked, in technical simulations the flame growth can be simulated with a greater confidence. In fact, the flame growth is accomplished because the kernel has enough energy to vaporize the surrounding droplets and promote the expansion of the combustion process, that can take place thanks to the local high temperature. Under laminar conditions, the flame propagation speed depends (in addition to pressure and temperature) on the spray size distribution, the overall equivalence ratio (comprising both the liquid and the vaporized fuel) and the degree of pre-evaporation [8]. Under turbulent conditions, the flame propagation is also strongly influenced by the turbulence, not only because of the intrinsic effect of turbulence on the flame, but also because

of its influence on local flow velocity, spray distribution and fluctuations in gaseous mixture fraction [8]. Although rather common combustion models are commonly used to model this stage, detailed analysis (e.g., [19]) revealed some peculiarities of the ignition process, that are normally overlooked in studies of flame propagation. For instance, it is shown that under the same equivalence ratio, the ignition propagation may be faster if the mixture is composed by liquid only, due to the presence of very small stoichiometric regions between droplets [19]. In fact, some of the processes taking place at inter-droplet distance may strongly influence the flame propagation, but their simulation is not feasible in current LES, as it would require to finely discretize the space between droplets. In this thesis, it is assumed that second stage is largely influenced by the turbulence and therefore LES is already sufficient to provide a realistic prediction. Anyway, the reader is warned that the use of a detailed chemistry or a more refined modelling of the evaporation process, may strongly improve this point.

1.1.3 Burner-scale flame establishment

The first two stages are extensively studied on a more fundamental level, because of the very small scales involved [8]. This latter stage is instead of interest in realistic configurations, characterized by complex flow structures. Once that the kernel is generated and the flame is sufficiently grown, it starts to interact with the underlying flow field, still largely influenced by turbulent fluctuations but also by the mean flow motion. In this last stage, it is fundamental that the flame moves in the right direction: for instance, ignition is usually accomplished when the flame reaches the inner recirculation zone, if present. Therefore, the convection of the flame caused by the flow field is somehow more relevant than the flame propagation itself [20]. Clearly, this last step is strongly dependent on the geometrical configuration and will be widely discussed in Ch. 3 for the test case here considered.

1.2 Governing equations for a multi-species reacting flow

It is worth introducing the governing equations that should be solved while considering a reactive flow. First of all, it is worth recalling the main assumptions [21]:

- the continuum hypothesis is valid;

- the considered mixture is single-phase;
- the flow is not hyper-sonic;
- the radiative heat transfer can be neglected;
- the considered fluid is Newtonian;
- no external sources of mass, momentum, energy and species are considered.

Under these assumptions, the governing equations can be introduced, considering a multi-species reactive mixture. Compressible Navier-Stokes equations are used for the conservation of mass, momentum, and energy, as well as $1 - n_{spec}$ transport equations for the n_{spec} species composing the mixture [22]. These differential equations are usually supplemented by an algebraic equation, namely the equation of state.
The continuity equation reads (Eq. 1.1):

$$\frac{\partial \rho}{\partial t} + \boldsymbol{\nabla} \cdot (\rho \boldsymbol{U}) = 0 \tag{1.1}$$

ρ stands for the mixture density and $\boldsymbol{U}$ for the mixture velocity.
The momentum equation can be expressed as (Eq. 1.2):

$$\frac{\partial \rho \boldsymbol{U}}{\partial t} + \boldsymbol{\nabla} \cdot (\rho \boldsymbol{U}\boldsymbol{U}) = -\boldsymbol{\nabla} P + \boldsymbol{\nabla} \cdot \boldsymbol{\tau} + \rho \boldsymbol{g} \tag{1.2}$$

Where P is the pressure and $\boldsymbol{g}$ the gravity vector. $\boldsymbol{\tau}$ is the viscous stress tensor (Eq. 1.3) where μ stands for the dynamic viscosity:

$$\boldsymbol{\tau} = \mu \left[\left(\boldsymbol{\nabla} \boldsymbol{U} + \boldsymbol{\nabla} \boldsymbol{U}^T \right) - \frac{2}{3} \left(\boldsymbol{\nabla} \cdot \boldsymbol{U} \right) \boldsymbol{I} \right] \tag{1.3}$$

The transport equation for the mass fraction Y_k the k-th species reads (Eq. 1.4):

$$\frac{\partial \rho Y_k}{\partial t} + \boldsymbol{\nabla} \cdot (\rho \boldsymbol{U} Y_k) = -\boldsymbol{\nabla} \cdot \boldsymbol{J}_k + \dot{\omega}_k \quad \text{for } k = 1, 1 - n_{spec} \tag{1.4}$$

Here, $\dot{\omega}_k$ is the reaction rate of the k-th species and $\boldsymbol{J}_k$ represents its diffusion flux. In ANSYS Fluent® [23], it is modelled as (Eq. 1.5):

$$\boldsymbol{J}_k = -\rho D_{k,m} \boldsymbol{\nabla} Y_k - D_{k,th} \frac{\boldsymbol{\nabla} T}{T} \tag{1.5}$$

Where $D_{k,m}$ and $D_{k,th}$ stand for the mass and the thermal diffusion respectively. The first term in Eq. 1.5 accounts for the species diffusion

due to the gradient in concentration. In ANSYS Fluent [23] a dilute approximation or *Fick's law* is applied to model such additional transport. Conversely, the second term of Eq. 1.5 accounts for the so-called *Soret effect*. The use of Eq. 1.5 may generate inconsistencies with mass conservation related to the differential diffusion of the species. To avoid that, an inert species (N_2 in this case) is not transported across the domain and its mass fraction is computed as $Y_{N_2} = 1 - \sum_{k=1}^{1-n_{spec}} Y_k$
Finally, the energy equation reads (Eq. 1.6):

$$\frac{\partial \rho E}{\partial t} + \boldsymbol{\nabla} \cdot [\boldsymbol{U}(\rho E + P)] = -\boldsymbol{\nabla} \cdot \boldsymbol{q} + \boldsymbol{\nabla} \cdot (\boldsymbol{\tau} \cdot \boldsymbol{U}) + \dot{\omega}_t \tag{1.6}$$

Where E is the specific total energy defined as in Eq. 1.7 and $\dot{\omega}_t$ is the heat of reaction, namely the heat-released by the reaction process.

$$E = h - \frac{P}{\rho} + \frac{\boldsymbol{U}^2}{2} \quad , \quad h = \sum_{k=1}^{n_{spec}} h_k Y_k \tag{1.7}$$

h stands for the sensible enthalpy (i.e. does not include the enthalpy of formation) of the mixture that can be retrieved from the enthalpy of each species and the mixture composition. Finally, the heat flux reads (Eq. 1.8):

$$\boldsymbol{q} = -\lambda \boldsymbol{\nabla} T + \sum_{k=1}^{n_{spec}} h_k Y_k \boldsymbol{J}_k \tag{1.8}$$

Where λ is the thermal conductivity of the mixture. The first term represents the heat diffusion expressed by the *Fourier's Law* whereas the second term is associated with the diffusion of species with different enthalpies, which can be relevant in multi-species mixtures.

1.3 Filtering procedure

The direct solution of the equations presented so far is not feasible in turbulent systems of technical interest. So far, LES represents to most promising tool to investigate the phenomena involved in gas turbine combustion. Regarding the ignition process, the need to simulate the unsteady process of flame establishment rules out the use of steady RANS simulations from the very beginning. Because of that, only the URANS approach can be seen as a viable alternative, although the advantage in terms of computational cost is less relevant. Moreover, if compared to LES, RANS simulation cannot provide the same accuracy while dealing with complex turbulent flows like the one present in gas turbine combustors.

Therefore, the LES framework established as the current standard in ignition simulations.
The aim of LES is to explicitly resolve the largest turbulent structures of the flow field whereas the effect of the smallest ones is included through models [22]. To this aim, a filtering procedure is applied which introduces a scale separation between the *resolved scales* and modelled *Sub-Grid Scales* (SGS) of the flow.
Filtering the $\phi(\mathbf{x})$ quantity consists in [22] (Eq. 1.9):

$$\bar{\phi}(\mathbf{x}) = \int \phi\left(\mathbf{x}'\right) F\left(\mathbf{x}-\mathbf{x}'\right) d\mathbf{x}' \tag{1.9}$$

where $\bar{\phi}(\mathbf{x})$ is the resolved part, $F\left(\mathbf{x}-\mathbf{x}'\right)$ is the filter and the non-resolved part can be expressed as $\phi'(\mathbf{x}) = \phi(\mathbf{x}) - \bar{\phi}(\mathbf{x})$. Although the filtering process can be carried out on a temporal/spectral basis or on physical space [21, 22], in ANSYS Fluent [23] only the latter is considered and a box filter [22] is used (Eq. 1.10) based on the grid size Δ.

$$F(\mathbf{x}) = F\left(x_1, x_2, x_3\right) = \begin{cases} 1/\Delta^3 & \text{if} \quad |x_i| \leq \Delta/2, i = 1,2,3 \\ 0 & \text{otherwise} \end{cases} \tag{1.10}$$

where (x_1, x_2, x_3) are the spatial coordinates of the location $\mathbf{x}$. This filter corresponds to an averaging over a cubic box of size Δ. As variable density flows is considered, Favre-filtering operation (weighted by the density) is preferred in this case (Eq. 1.11):

$$\bar{\rho}\tilde{\phi}(\mathbf{x}) = \int \rho\phi\left(\mathbf{x}'\right) F\left(\mathbf{x}-\mathbf{x}'\right) d\mathbf{x}' \tag{1.11}$$

For the sake of brevity, such section was strongly simplified and the reader interested into a detailed discussion about filtering procedure in compressible flows is addressed to [21].

1.4 Governing equations in the LES framework

It is now of primary importance to introduce the governing equations solved within the LES framework. It is worth to already introduce in the equations the additional source terms employed in such work, in particular the ones related to the interaction with the spray and with the spark, even if their formulation will be explicated in the next sections.

After the filtering process, the continuity equation reads (Eq. 1.12):

$$\frac{\partial \bar{\rho}}{\partial t} + \boldsymbol{\nabla} \cdot (\bar{\rho}\tilde{\boldsymbol{U}}) = \overline{\dot{S}}_{mass} \tag{1.12}$$

Where $\overline{\dot{S}}_{mass}$ is the filtered source term that accounts for the mass transfer due to the evaporation of the spray.
The momentum equation can be written as Eq. 1.13:

$$\begin{aligned} \frac{\partial \bar{\rho}\tilde{\boldsymbol{U}}}{\partial t} + \boldsymbol{\nabla} \cdot (\bar{\rho}\tilde{\boldsymbol{U}}\tilde{\boldsymbol{U}}) = \\ -\boldsymbol{\nabla}\overline{P} + \boldsymbol{\nabla} \cdot \overline{\boldsymbol{\tau}} + \bar{\rho}\boldsymbol{g} - \boldsymbol{\nabla} \cdot \left(\bar{\rho}\widetilde{\boldsymbol{U}\boldsymbol{U}} - \bar{\rho}\tilde{\boldsymbol{U}}\tilde{\boldsymbol{U}}\right) + \overline{\dot{S}}_{mom} \end{aligned} \tag{1.13}$$

$\overline{\dot{S}}_{mom}$ is the source term related to exchange of momentum with the liquid phase due to the aerodynamic forces. The term associated with the sub-grid Reynolds stress $\bar{\boldsymbol{\tau}}_{sgs} = \bar{\rho}\widetilde{\boldsymbol{U}\boldsymbol{U}} - \bar{\rho}\tilde{\boldsymbol{U}}\tilde{\boldsymbol{U}}$ is not closed and must be modeled.
After filtering, the conservation equation for the k-th species reads (Eq. 1.14):

$$\begin{aligned} \frac{\partial \bar{\rho}\tilde{Y}_k}{\partial t} + \boldsymbol{\nabla} \cdot \left(\bar{\rho}\tilde{\boldsymbol{U}}\tilde{Y}_k\right) = -\boldsymbol{\nabla} \cdot \overline{\boldsymbol{J}}_k \\ -\boldsymbol{\nabla} \cdot \left(\bar{\rho}\widetilde{\boldsymbol{U}Y_k} - \bar{\rho}\tilde{\boldsymbol{U}}\tilde{Y}_k\right) + \overline{\dot{\omega}}_k + \overline{\dot{S}}_{spec,k} \quad \text{for } k = 1, 1 - n_{spec} \end{aligned} \tag{1.14}$$

Similarly to the previous equations $\overline{\dot{S}}_{spec,k}$ is used to account for the evaporation from the liquid phase of the fuel species. The filtered diffusion flux reads (Eq. 1.15):

$$\overline{\boldsymbol{J}}_k = -\bar{\rho}D_{k,m}\boldsymbol{\nabla}\tilde{Y}_k - D_{k,th}\frac{\boldsymbol{\nabla}\tilde{T}}{\tilde{T}} \tag{1.15}$$

Also the unresolved species fluxes $\bar{\rho}\widetilde{\boldsymbol{U}Y_k} - \bar{\rho}\tilde{\boldsymbol{U}}\tilde{Y}_k$ and the filtered reaction rate $\overline{\dot{\omega}}_k$ must be modelled.
Finally, the filtered energy equation reads (Eq. 1.16):

$$\begin{aligned} \frac{\partial \bar{\rho}\tilde{E}}{\partial t} + \boldsymbol{\nabla} \cdot \left(\bar{\rho}\tilde{\boldsymbol{U}}\tilde{E} + \overline{P\boldsymbol{U}}\right) = \\ -\boldsymbol{\nabla} \cdot \bar{\boldsymbol{q}} + \boldsymbol{\nabla} \cdot \left(\overline{\boldsymbol{\tau} \cdot \boldsymbol{U}}\right) - \boldsymbol{\nabla} \cdot \left(\bar{\rho}\widetilde{\boldsymbol{U}E} - \bar{\rho}\tilde{\boldsymbol{U}}\tilde{E}\right) + \overline{\dot{\omega}}_t + \overline{\dot{S}}_{energy} \end{aligned} \tag{1.16}$$

$\overline{\dot{S}}_{energy}$ is used to account for the heat transfer with the liquid phase and the energy released by the spark. The filtered heat flux is expressed as

(Eq. 1.17):

$$\bar{\boldsymbol{q}} = -\lambda \boldsymbol{\nabla} \tilde{T} + \bar{\rho} \sum_{k=1}^{n_{spec}} \tilde{h}_k \tilde{Y}_k \overline{\boldsymbol{J}}_k \tag{1.17}$$

Similarly to the previous equation, the unresolved heat flux $\bar{\rho}\widetilde{\boldsymbol{U}E} - \bar{\rho}\tilde{\boldsymbol{U}}\tilde{E}$ and the filtered heat of reaction $\overline{\dot{\omega}_t}$ must be modelled. A simple approach is employed for the remaining unclosed term $\overline{\boldsymbol{\tau} \cdot \boldsymbol{U}} = \overline{\boldsymbol{\tau}} \cdot \tilde{\boldsymbol{U}}$ and $\overline{P\boldsymbol{U}} = \overline{P}\tilde{\boldsymbol{U}}$.

1.5 Turbulence Modelling

According to the Boussinesq assumption, the sub-grid Reynolds stres tensor arising from the filtering procedure can be recast as:

$$\bar{\boldsymbol{\tau}}_{sgs} - \frac{\boldsymbol{I}}{3}\bar{\boldsymbol{\tau}}_{sgs} = \mu_{sgs}\left(\boldsymbol{\nabla}\tilde{\boldsymbol{U}} + \boldsymbol{\nabla}\tilde{\boldsymbol{U}}^T\right) \tag{1.18}$$

In this work, the *Wall-Adapting Local Eddy-viscosity* (WALE) model [24] is used to model the turbulent sub-grid viscosity μ_{sgs}.

$$\mu_{sgs} = \bar{\rho}\left(C_w \Delta\right)^2 \frac{\left(\boldsymbol{S_d}\boldsymbol{S_d^T}\right)^{3/2}}{\left(\bar{\boldsymbol{S}}\bar{\boldsymbol{S}}^{\boldsymbol{T}}\right)^{5/2} + \left(\boldsymbol{S_d}\boldsymbol{S_d^T}\right)^{5/4}} \tag{1.19}$$

Where $C_w = 0.325$ in ANSYS Fluent [23] and Δ is the grid size. $\boldsymbol{S_d}$ and $\bar{\boldsymbol{S}}$ are the traceless symmetric part of the square of the velocity gradient tensor and the deformation tensor of the resolved field respectively [24]. Although similar to the Smagorinsky-Lilly [25], the WALE model provides the correct wall asymptotic behavior for wall bounded flows and returns a zero turbulent viscosity for laminar shear flows, allowing the correct treatment of laminar zones in the domain [24].
Finally, the remaining unclosed fluxes are modelled in ANSYS Fluent [23] as:

$$\left(\bar{\rho}\widetilde{\boldsymbol{U}E} - \bar{\rho}\tilde{\boldsymbol{U}}\tilde{E}\right) = -\frac{\mu_{sgs} C_p}{\mathrm{Pr}_{sgs}} \boldsymbol{\nabla}\tilde{T} \tag{1.20}$$

and:

$$\left(\bar{\rho}\widetilde{\boldsymbol{U}Y_k} - \bar{\rho}\tilde{\boldsymbol{U}}\tilde{Y}_k\right) = -\frac{\mu_{sgs}}{\mathrm{Sc}_{sgs}} \boldsymbol{\nabla}\tilde{Y}_k \tag{1.21}$$

Where C_p is the specific heat at constant pressure of the mixture, Pr_{sgs} and Sc_{sgs} are the sub-grid Prandtl and Schmidt number respectively.

1.6 Combustion modelling

After the filtering procedure of the governing equations shown in the previous sections, two terms still need to be closed, namely the filtered reaction rate $\overline{\dot{\omega}}_k$ in the species transport equation and the filtered heat-release $\overline{\dot{\omega}}_t$ in the energy equation. Turbulent combustion models were developed to tackle this issue but it is beyond the scope of this work to review all the proposed models (the interested reader is addressed to specific literature [22, 26]).

1.6.1 Thickened Flame Model

In this work, the *Thickened Flame Model* (TFM) (also known as *Artificially Thickened Flame* (ATF) model) is adopted. This model was derived for fully premixed flames [27] and then extended to partially premixed and non-premixed ones [28]. The main idea behind the TFM model is to artificially thicken the flame front in order to be able to resolve it on the LES grid. From the dimensional analysis conducted by [29], the laminar flame speed s_l and the laminar flame thickness δ_l are proportional to:

$$s_l \propto \sqrt{D_{th}\dot{\omega}} \qquad\qquad \delta_l \propto \sqrt{\frac{D_{th}}{\dot{\omega}}} \tag{1.22}$$

It is possible to artificially thicken the flame, preserving the correct laminar flame speed, by increasing the thermal diffusivity D_{th} and reducing the reaction rate $\dot{\omega}$ by a factor $\mathcal{F} = N\Delta/\delta_l$:

$$\begin{aligned} s_l \propto \sqrt{\mathcal{F} D_{th} \frac{\dot{\omega}}{\mathcal{F}}} \quad &\rightarrow \quad s_l^{TFM} \propto \sqrt{D_{th}\dot{\omega}} = s_l \\ \delta_l \propto \sqrt{\frac{\mathcal{F} D_{th}}{\frac{\dot{\omega}}{\mathcal{F}}}} \quad &\rightarrow \quad \delta_l^{TFM} \propto \mathcal{F}\sqrt{\frac{D_{th}}{\dot{\omega}}} = \mathcal{F}\delta_l \end{aligned} \tag{1.23}$$

The parameter N identifies the number of points in the flame while the superscript TFM indicates the thickened state. For a sufficiently large thickening factor $\mathcal{F}$, the flame front is resolved over the LES grid (Fig. 1.1). The choice of $\mathcal{F}$ is a function of the grid size and the laminar flame thickness [23].
The thickening from δ_l to δ_l^{TFM} causes a significant change in the interaction between the chemistry and turbulence [27]. In fact, the Damköler number Da, which represents the ratio between the turbulent τ_t and

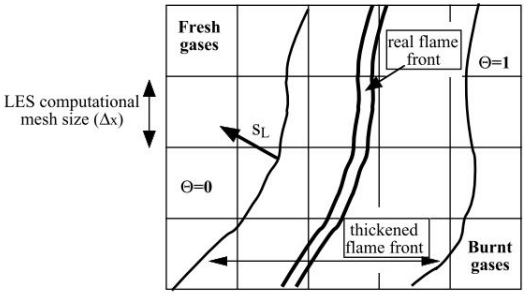

Figure 1.1: Sketch of thickened flame approach concept (adapted from [22]).

chemistry τ_c time scale, changes as:

$$\mathrm{Da} = \frac{\tau_t}{\tau_c} = \frac{l_t}{u'}\frac{s_l}{\delta_l} \quad \rightarrow \quad \mathrm{Da}^{TFM} = \frac{l_t}{u'}\frac{s_l^{TFM}}{\delta_l^{TFM}} = \frac{\mathrm{Da}}{\mathcal{F}} \tag{1.24}$$

Because of that, the eddies smaller than δ_l^{TFM} do not properly interact with the flame, reducing the wrinkling caused by the turbulence (Fig. 1.2). This could lead to an erroneous reduction of the reaction rate due to the underestimation of the flame surface. In order to mitigate this issue,

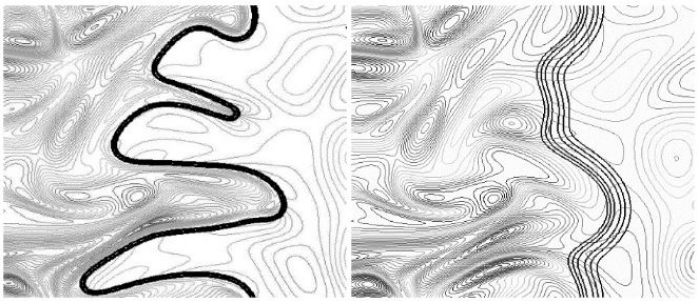

Figure 1.2: Flame/turbulence interaction: reference non-thickened flame (left) and thickened flame with $\mathcal{F} = 5$ (right) [22]

D_{th} and $\dot{\omega}$ can be multiplied by an efficiency function $\mathcal{E}$. By recasting Eq. 1.23, it can be shown that laminar flame speed is enhanced by the

introduction of $\mathcal{E}$, whereas the initial thickening is preserved:

$$s_l^{TFM} \propto \mathcal{E} s_l \qquad \delta_l^{TFM} \propto \mathcal{F} \delta_l \tag{1.25}$$

The efficiency function identifies the ratio between the wrinkling factor of the non-thickened flame and the thickened one:

$$\mathcal{E} = \frac{\Xi(\delta_l)}{\Xi(\delta_l^{TFM})} \tag{1.26}$$

Several formulations were proposed in the literature for $\mathcal{E}$. One of the most used is the one of Charlette [30, 31]:

$$\Xi(\delta_l) = \left(1 + min\left[\frac{\Delta}{\delta_l}, \Gamma\left(\frac{\Delta}{\delta_l}, \frac{u'_\Delta}{s_l}, Re_{\Delta_e}\right)\frac{u'_\Delta}{s_l}\right]\right)^\beta \tag{1.27}$$

with β the exponent parameter, u'_Δ the characteristic turbulent velocity at the filter scale Δ and Γ a function that mimics the unresolved strain rate. The second $\mathcal{E}$ formulation was proposed by Colin et al. [27]:

$$\Xi(\delta_l) = 1 + \alpha(Re_t)\Gamma\left(\frac{\Delta}{\delta_l}, \frac{u'_\Delta}{s_l}\right)\frac{u'_\Delta}{s_l} \tag{1.28}$$

with α a parameter depending on the turbulent Reynolds number. In this work, the second formulation is chosen for the reactive simulations.
Additionally, the thickening procedure introduces another issue in the regions far from the flame where erroneous heat transfer may occur due to the artificially enhanced thermal diffusivity. Therefore, the flame is dynamically thickened only in a narrow band around the reaction zone employing a sensor factor [28]. In ANSYS Fluent such sensor factor $\mathcal{S}$ is defined as [23]:

$$\mathcal{S} = \tanh\left(\beta^* \frac{|\bar{R}|}{max(|\bar{R}|)}\right) \tag{1.29}$$

with $|\bar{R}|$ the spatially filtered absolute value of the reaction rate, $max(|\bar{R}|)$ is its maximum value of in the domain and $\beta^* = 10$. As a result $\mathcal{S}$ ranges from unity in the band around the flame to zero outside.
Finally, the thermal diffusivity reads:

$$D_{eff} = D_{th}\mathcal{E}[1 + (\mathcal{F} - 1)\mathcal{S}] + D_{th,sgs}(1 - \mathcal{S}) \tag{1.30}$$

where D_{th} and $D_{th,sgs}$ is the laminar and turbulent thermal diffusivity respectively. As reported in Fig. 1.3, away from the flame $\mathcal{S}$ is set equal to zero so the diffusivity assumes the non-thickened value $(D_{th} + D_{th,sgs})$. Conversely, in a narrow band around the flame $\mathcal{S}$ is set equal to 1.0 so the

diffusivity is enhanced by a factor $\mathcal{EF}$. In the end, it is worth pointing

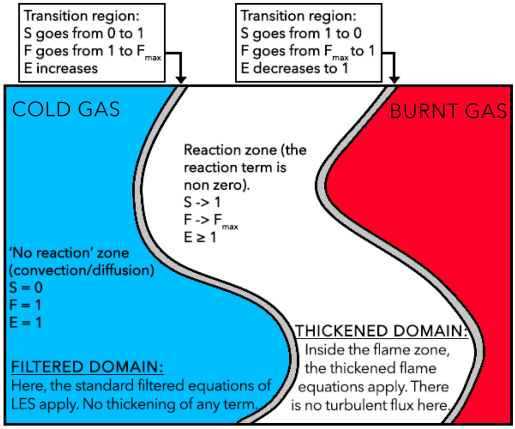

Figure 1.3: Schematic representation of the dynamically thickening procedure [32].

out the modified form used for the chemical source terms in the species equations (Eq. 1.14) and in the energy equation (Eq. 1.16):

$$\widetilde{\dot{\omega}_k^*} = \frac{\mathcal{E}\widetilde{\dot{\omega}_k}}{\mathcal{F}} \qquad \widetilde{\dot{\omega}_t^*} = \frac{\mathcal{E}\widetilde{\dot{\omega}}_t}{\mathcal{F}} \tag{1.31}$$

In this work $\widetilde{\dot{\omega}_k}$ is computed as a laminar reaction rate using the filtered values of temperature and species concentrations.

1.6.2 Reaction mechanism

The oxidation of hydrocarbon molecules normally involves several intermediate species and reactions. So-called *reaction mechanisms* are available to describe this process at a numerical level, with a different number of species and reactions, that ultimately depends on the application and the required accuracy. Clearly, a larger number of species normally implies a higher accuracy of the mechanism but, by using the governing equations shown in Sec. 1.4, a transport equation should be solved for each one of these. Moreover, the the presence of a large number of species also introduces the need of an implicit solution of the chemical source terms. In this way, the computational effort could rapidly be prohibitive

if LES is used. To tackle this issue, a two-step mechanism with six species called $2S\_C_7H_{16}\_DP$ [33] is selected here. This mechanism was obtained in [33] following the methodology presented in [34] and involves six species (C_7H_{16}, O_2, H_2O, CO, CO_2 and N_2) and two reactions:

$$2C_7H_{16} + 15O_2 \rightarrow 14CO + 16H_2O \tag{1.32}$$

$$CO + 1/2O_2 \leftrightarrow CO_2 \tag{1.33}$$

The forward reaction rates exploit the Arrhenius formulation:

$$k_{f,1} = A_1 f_1(\phi) e^{(-E_{a1}/RT)} \left[C_7H_{16}\right]^{n_f} \left[O_2\right]^{n_{O_2,1}} \tag{1.34}$$

$$k_{f,2} = A_2 f_2(\phi) e^{(-E_{a2}/RT)} \left[C_0\right]^{n_{CO}} \left[O_2\right]^{n_{O_2,2}} \tag{1.35}$$

where A is the pre-exponential factor, E_a the activation energy and n the reaction exponents. The employed values for these constants are summarized in Tab. 1.1.

	Reaction 1	Reaction 2
Pre-exponential factor	1.4×10^{11}	5.0×10^{9}
Activation energy	29000 cal/mol	21000 cal/mol
Reaction exponents	$n_f = 0.6$	$n_{CO} = 1$
	$n_{O_2,1} = 0.9$	$n_{O_2,2} = 0.5$

Table 1.1: Coefficients of the reduced scheme $2S\_C_7H_{16}\_DP$.

The functions $f_1(\phi)$ and $f_2(\phi)$ are the pre-exponential adjustments, already proposed by [35] and [36], whose purpose is to recover the correct laminar flame speed in rich mixtures [34]. Their formulation is not reported here for the sake of brevity and the interested reader is addressed to the original reference [33]. This mechanism is now compared against a more detailed mechanism proposed in [37] that involves 106 species and 1791 reactions, hereafter referred as *POLIMI*. It should be pointed out that such mechanism can not be considered detailed as well, but it represents a good candidate to test the performance of $2S\_C_7H_{16}\_DP$. The `freeflame` application of the CANTERA [38] suite is used to simulate a 1D freely-propagating flat flame with the aforementioned mechanisms. In Fig. 1.4 the comparison in terms of laminar flame speed is reported for the two mechanisms, showing that the global one is fairly capable of reproducing the correct speed in the range of ϕ of interest, for the given temperature and pressure (471 K and 101325 Pa). Moreover, in Fig. 1.5 a comparison in terms of species concentrations is reported for the two

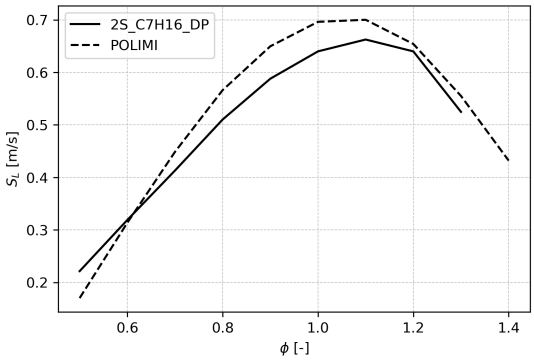

Figure 1.4: Laminar flame speed comparison at 300 K and 101325 Pa between $2S\_C_7H_{16}\_DP$ global mechanism and POLIMI.

mechanism at $\phi = 0.61$ (which corresponds to the nominal conditions of the investigated test case). Two main zones can be identified:

- a first zone where the oxidation of the n-heptane takes place until it is completely consumed (close to the maximum of CO);
- a second one where the CO is slowly oxidized into CO_2.

A good agreement is obtained with the *POLIMI* mechanism in terms of species concentrations (Fig. 1.5). To further assess the validity of the reduced mechanism, an additional comparison in terms of heat-release rate and temperature is reported in Fig. 1.6. Again, a fair agreement can be pointed out, suggesting that the global reaction mechanism can be effectively used to describe the flame under the specified operating conditions.

1.6.3 OH concentration for experimental comparison

One of the most used techniques to investigate the flame structure is the *OH-PLIF*. In this method, images are taken of the intermediate radical OH concentration. A common way to compare against simulation consists in showing both numerical and experimental distributions of OH. Unluckily, the OH radical is not present in the employed mechanism and another strategies must be adopted to retrieve its concentration. To tackle this issue, in this work the *Partial Equilibrium Assumption* (PEA) is used to evaluate it without introducing additional and time-consuming

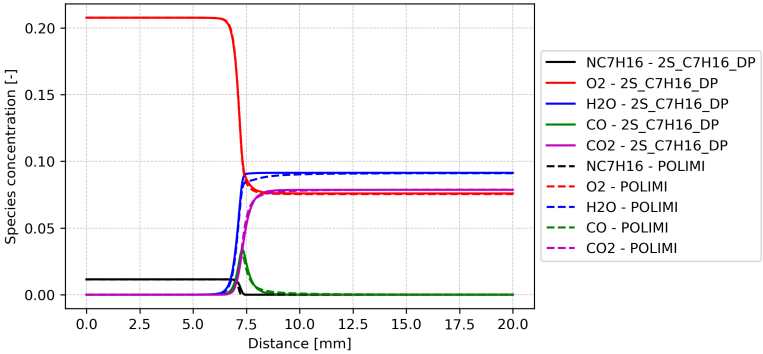

Figure 1.5: Species comparison at $\phi = 0.61$, 300 K and 101325 Pa between $2S\_C_7H_{16}\_DP$ global mechanism and POLIMI.

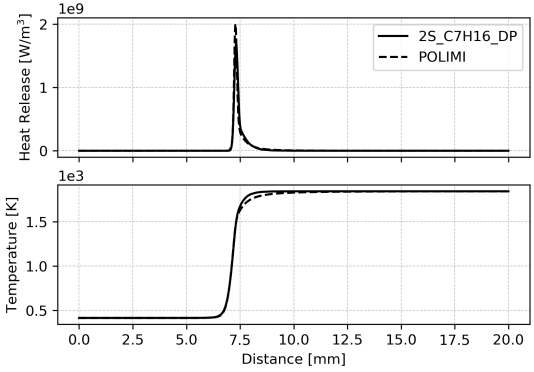

Figure 1.6: Heat-release and temperature comparison at $\phi = 0.61$, 300 K and 101325 Pa between $2S\_C_7H_{16}\_DP$ global mechanism and POLIMI.

transport equations.
The approach here reported is used in [23] to evaluate the OH radical concentration in the Zeldovich NO_x formation mechanism. The molar concentrations O and OH are computed as:

$$[O] = 36.64T^{1/2}[O_2]^{1/2}e^{-27123/T} \tag{1.36}$$

$$[OH] = 2.129 \times 10^2 T^{-0.57} e^{-4595/T}[O]^{1/2}[H_2O]^{1/2} \tag{1.37}$$

Fig. 1.7 shows the O and OH mole fractions for the two mechanism: Even

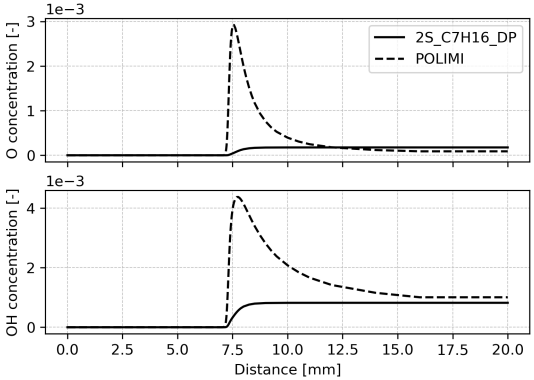

Figure 1.7: Comparison of O and OH mole fraction POLIMI and PEA based on two-step mechanism 2S_C_7H_{16}_DP.

if the initial peak in radical concentration is not reproduced by the PEA, it successfully recovers the correct concentration in the post flame, where the temperature is high. Although not ideal, PEA is used in Ch. 3 to compare against the experimental OH-PLIF: a strong underestimation of the OH radical must be expected close to the flame front, whereas a more accurate prediction should be recovered far from it. Anyway, such simplifications is necessary for a fair comparison with the experimental data. As an alternative, while the heat-release $\overline{\dot{\omega}_t}$ of Eq. 1.16) can beused to identify the flame front, but it does not recover the OH distribution after the flame, largely impairing the comparison.

1.7 Spray modelling

In this set of simulations, the gaseous phase is treated as a continuum whereas the dispersed liquid phase is tracked with a specific set of equations in a Lagrangian framework. The dispersed and carrier phase influence each other through momentum, mass and energy transfers. On the one hand, the source terms acting on the gas phase are constructed by taking into account the particles within the considered computational cell. On the other hand, the forces acting on the single liquid particle are obtained by interpolation of the gas phase variables at the particle location.
In this work, a two way coupling approach is considered and the primary breakup is not modelled (this point will become critical in Ch. 4). The collision between particles and the the secondary breakup are neglected as well, since they are believed to play a minor role in the considered case. Hence, the droplet evolution is described by the following equations:

$$\frac{D\boldsymbol{X_p}}{Dt} = \boldsymbol{u_p} \tag{1.38}$$

$$\frac{Dm_p\boldsymbol{u_p}}{Dt} = \boldsymbol{F_p^{ext}} \tag{1.39}$$

$$\frac{Dm_p}{Dt} = \dot{m}_p \tag{1.40}$$

$$\frac{Dm_p h_p}{Dt} = \dot{\Phi}_p \tag{1.41}$$

where $\boldsymbol{X_p}$, $\boldsymbol{u_p}$, m_p and h_p are the position vector, the velocity vector, the mass and the sensible enthalpy of p-th particle respectively. In these equations the source terms are represented by the external forces acting on the particle $\boldsymbol{F_p^{ext}}$, the evaporation rate $\dot{m}_p$ and of the enthalpy variation due to evaporation and heat transfer $\dot{\Phi}_p$. Specific Lagrangian sub-models are then used to model them.
In this work, the only external forces $\boldsymbol{F_p^{ext}}$ considered are the gravity and the drag. In particular, the non-deformable drag law by Morsi et al. [39] is used to evaluate the drag coefficient.
The well-known Spalding law [40] with the Ambramzon-Sirignano correction [41] is used to model the evaporation process. The main assumptions of the model are:

- the temperature of the droplet is homogeneous.
- the relative velocity between the droplet and the surrounding gas is zero (this one will be removed later).

- the behavior of the gas phase is quasi-steady (time derivative are neglected in the gaseous phase).

- the fuel vapor is in saturation conditions on the droplet surface (equilibrium assumption).

- the droplet is spherical (spherical assumption).

For the sake of clarity, hereafter the eulerian quantity are reported without filtering, although it is clearly applied in the LES framework. Under these assumptions, the evaporation rate can be expressed as:

$$\frac{dm_p}{dt} = -Sh\pi d_p[\rho D_F]\ln(B_M + 1) \tag{1.42}$$

with the Sherwood number Sh equal to 2 (in the quiescent case) and the Spalding transfer number B_M:

$$B_M = \frac{Y_{F,p} - Y_{F,\infty}}{1 - Y_{F,p}} \tag{1.43}$$

$Y_{F,p}$ is the mass fraction of fuel close to the droplet surface, based on the assumption of phase equilibrium, whereas $Y_{F,\infty}$ is the mass fraction found in the surrounding volume far from the droplet (usually assumed equal to the cell value in computations).
The temperature evolution instead can be retrieved through the following expression:

$$\frac{dT_P}{dt} = \frac{1}{m_p C_{p,l}}(\dot{m}_P L_v(T_p) - \lambda\pi Nu d_p(T_p - T_\infty)\frac{\ln(B_T + 1)}{B_T}) \tag{1.44}$$

In Equation 1.44, $L_v(T_p)$ is the latent heat of vaporization, Nu is the Nusselt number and B_T is temperature Spalding transfer number. For B_T two expressions are used:

$$B_T = \begin{cases} B_M & \text{if} \quad Le = 1 \\ (1 + B_M)^{\frac{1}{Le_F}} - 1 & \text{if} \quad Le \neq 1 \end{cases} \tag{1.45}$$

where Le is the Lewis number. In this work a $Le \neq 1$ is adopted.
In common applications, a relative velocity is always present between the two phases, which is in contrast with the second assumptions of the Spalding model. Therefore, in [42] a correction is introduced on the Sherwood Sh and the Nusselt Nu number in Eq. 1.42 and 1.44 respectively. Such modification allows to take into account the enhancement of the

evaporation due to the convection:

$$Sh = 2 + 0.55 Re_p^{1/2} Sc_F^{1/3} \tag{1.46}$$

$$Nu = 2 + 0.55 Re_p^{1/2} Pr^{1/3} \tag{1.47}$$

Sc_F is the Schmidt number of the fuel and Pr the Prandtl number. Re_p is the particle Reynolds number, defined as:

$$Re_p = \frac{\rho_g d_p |\boldsymbol{U} - \boldsymbol{U_p}|}{\mu_g} \tag{1.48}$$

where $|\boldsymbol{U} - \boldsymbol{U_p}|$ is the relative velocity among phases. The Abramzon-Sirignano correction [41] introduces a further modification into the Sh and Nu definitions to take into account for the boundary layer around the droplet aiming at a more accurate evaluation of the mass and the thermal fluxes:

$$Sh^* = 2 + \frac{Sh - 2}{F_M} \tag{1.49}$$

$$Nu^* = 2 + \frac{Nu - 2}{F_T} \tag{1.50}$$

with

$$F_M = (1 + B_M)^{0.7} \frac{\ln(1 + B_M)}{B_M} \tag{1.51}$$

$$F_T = (1 + B_T)^{0.7} \frac{\ln(1 + B_T)}{B_T} \tag{1.52}$$

Finally Eq. 1.42 and Eq. 1.44 read:

$$\dot{m}_p = -Sh^* \pi d_p [\rho D_F] \ln(B_M + 1) \tag{1.53}$$

$$\frac{dT_P}{dt} = \frac{1}{m_p C_{p,l}} (\dot{m}_P L_v(T_p) - \lambda \pi N u^* d_p (T_p - T_\infty) \frac{\ln(B_T + 1)}{B_T}) \tag{1.54}$$

As suggested in [43] and [33] the evaporation model must be corrected to take into account the artificial increase of the diffusivity introduced by the TFM:

$$\frac{dm_P}{dt} = -Sh^* \pi d_p [\rho D_F] \ln(B_M + 1) \frac{1}{\mathcal{F}} \tag{1.55}$$

$$\frac{dT_P}{dt} = \frac{1}{m_p C_{p,l}} (\dot{m}_P L_v(T_p) - \lambda \pi N u^* d_p (T_p - T_\infty) \frac{\ln(B_T + 1)}{B_T} \frac{1}{\mathcal{F}}) \tag{1.56}$$

The correction is not implemented in the solver by default, even if it is necessary to correctly predict the evaporation rate when $\mathcal{F} \neq 1$. Therefore, Eq. 1.55 and Eq. 1.56 are implemented through User Defined Functions

(UDF) and used to model the evaporation process. To validate this new implementation, the experimental data reported in [44] are employed (471 K and 100 kPa). Fig. 1.8 shows the d^2-law and temperature evolution of a single droplet in a quiescent environment. For a better comparison the default evaporation law of ANSYS Fluent [23, 45] is also reported. The implemented model instead is referred as Abramzon-Sirignano in the legend. Both laws are able to fit well the experimental data.

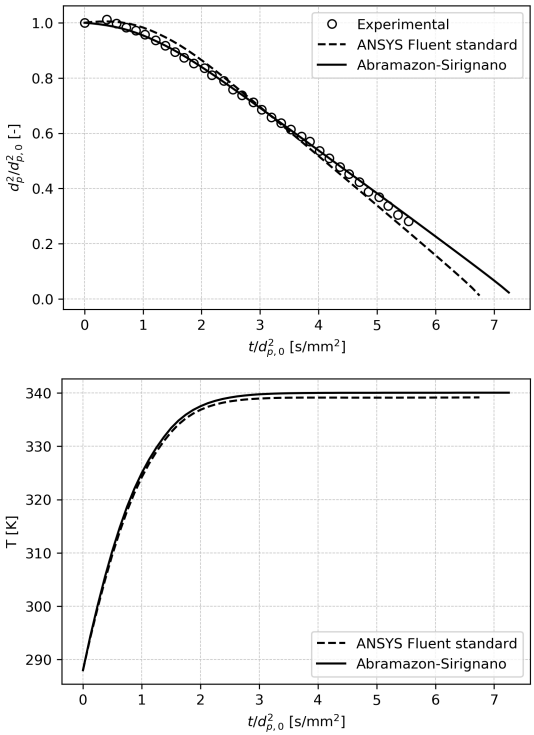

Figure 1.8: Evaporation rate and droplet temperature of a single droplet in a quiescent surrounding environment (non-thickened case, $\mathcal{F} = 1$).

Fig. 1.9 reports the same comparison with $\mathcal{F} = 10$. With the standard model, the droplet immediately reaches the boiling temperature due to the artificially increased diffusivity. Therefore, its evaporation rate is strongly overestimated. Conversely, the custom UDF ensures the proper

evaporation rate to be recovered.

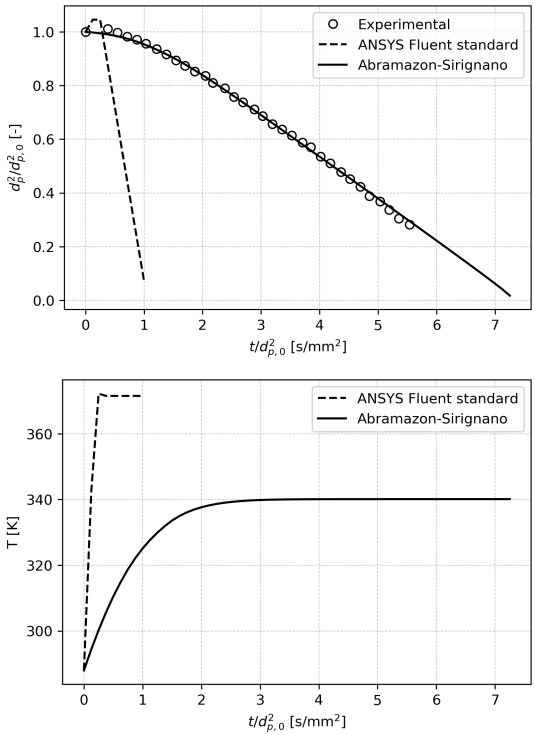

Figure 1.9: Evaporation rate and droplet temperature of a single droplet in a quiescent surrounding environment (thickened case, $\mathcal{F} = 10$).

1.8 Spark modelling

In this work, the *Energy Deposition* (ED) model is used to describe the laser spark [46]. In the ED model, the spark is mimicked by adding an explicit source term in the energy equation, characterized by a Gaussian shape in space and time and letting the LES solver explicitly compute the generation of the initial kernel. To avoid reaching a too high temperature and strong discontinuities in the resolved equations, the deposited energy is smoothed in space and time with respect to the actual spark duration

and size (Fig. 1.10). This is due to the impossibility to model the plasma with a reduced kinetic scheme that includes simplified thermodynamic and transport properties. The volumetric source term $\dot{Q}$ added to the

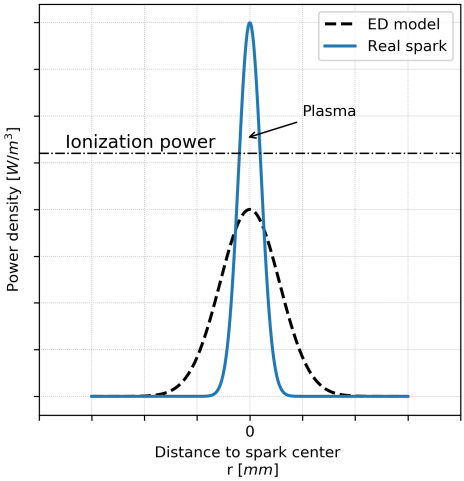

Figure 1.10: Sketch of radial power distribution for a real spark and for the ED model at a given time step.

energy equation (in $\overline{\dot{S}}_{energy}$) is defined as a Gaussian distribution in space and time:

$$\dot{Q}(r,t) = \frac{E_i}{4\pi^2\sigma_t\sigma_s^3} e^{-\frac{1}{2}(\frac{r}{\sigma_s})^2} e^{-\frac{1}{2}(\frac{t-t_0}{\sigma_t})^2} \tag{1.57}$$

where E_i represents the transmitted energy to the mixture. In [47] it is explained that only the 10% of the generated energy is actually transferred to the flow due to the losses generated by the shock wave expansion and the radiative effects. Clearly, this must be taken into account while setting the deposited energy E_i by the ED model, which is entirely transmitted to the flow. The r term is the distance from the spark center while t_0 identifies the time when the power density reaches its maximum. Two additional parameters, σ_s and σ_t, are introduced to manage the size and

the duration of the spark:

$$\sigma_s = \frac{\Delta_s}{a}, \qquad \sigma_t = \frac{\Delta_t}{a} \tag{1.58}$$

Δ_s and Δ_t are the characteristic size and duration of the spark. The constant a is set equal to $4\sqrt{\ln 10}$ to obtain 98% of the deposited energy in $\Delta_s^3 \Delta_t$ [46]. Particular attention must be paid to Δ_s, as it does not represent the size of the spark but it is rather chosen to obtain a maximum fixed temperature close to the spark position in absence of any heat losses:

$$T_{max} \approx \frac{1}{\rho_0 c_p} \int_{-\infty}^{+\infty} \dot{Q}(r=0)dt + T_0 = \frac{1}{\rho C_p} \frac{E_i}{(2\pi)^{3/2}\sigma_s^3} + T_0 \tag{1.59}$$

where T_0 and ρ are the initial temperature and density of the unburnt gas. Therefore, Δ_s can be estimated as:

$$\Delta_s = \sqrt{\frac{a}{\pi}} \sqrt[3]{\frac{E_i}{\rho_0 C_p (T_{k,max} - T_0)}} \tag{1.60}$$

Particular attention must be paid when the ED model is used together with the TFM model. At first, the ED model starts the energy deposition and the local temperature rises. Over a certain temperature, the finite rate chemistry actually starts to generate combustion products and initiate the flame kernel. If the flame thickening was activated from the very beginning, a non-physical dispersion of heat may lead to ignition failure. Therefore, the thickening is not applied during the first instants of the energy deposition, but starts after a while, when the initial flame is actually produced. In this work, the triggering criterion is based on the mass fraction of CO_2:

$$\max Y_{CO_2} = 0.99 Y_{CO_2,equil} \tag{1.61}$$

Therefore, the thickening starts when the maximum value of CO_2 mass fraction in the domain reaches the 99% of the equilibrium value under chemical equilibrium conditions. A similar approach was originally proposed by Barré [32, 48] and further applied in [18, 49], using a different threshold in the mass fraction of the reaction products (90% of the equilibrium one, rather than 99%). In this work, the choice of an higher value is motivated by the will of delaying as much as possible the enhancement of heat dissipation caused by the TFM, that may lead to early kernel quenching. Clearly, this choice could potentially influence the outcome of the spark and further work should be addressed to prove the robustness

of the selected threshold value. Moreover, in the cited works two different grids were used for the two stages (before and after the TFM activation) and the flow field from the first one was interpolated onto the second one with a coarser resolution. This procedure is not retained here for the sake of simplicity and to avoid introducing additional errors with the interpolation procedure. As an additional constraint, if the condition of Eq. 1.61 is not met after certain time, the simulation is set to start the thickening anyway to correctly simulate the flame propagation in the LES framework and to take into account the sub-grid effects on combustion. It is worth pointing out that this was not the case of the simulation presented in the next.

1.9 Conclusions to Chapter 1

In this chapter, the problem of modelling ignition in spray flames was discussed. The governing equations were presented for a multi-species reacting flow. Since the direct solution of these equations is not feasible, the filtering procedure was introduced in the LES framework. After that, the closure of some unclosed terms due to turbulence was shown and later the models used for combustion, spray and energy deposition modelling were discussed.

Chapter 2

Ignition probability computation

In this chapter, the problem of computing the ignition probability is introduced. While the approach presented in Ch. 1 represents a useful tool to achieve a better understanding of the ignition process from a physical point of view, the direct use of reactive LES to compute the ignition probability is not feasible.
Therefore, several *low-order* models were proposed, in the attempt of predicting the ignition probability with numerical tools. At the beginning of this chapter, the concept of ignition probability is discussed, followed by a short literature survey to analyze the different approaches available in literature to compute it. Later, the SPHINTIR model is analysed in greater detail, as it represents the tool employed in this thesis.

2.1 The concept of ignition probability

In Ch. 1 the different phases of ignition were introduced *naively* assuming that it will always be successful. This is not true at all! In fact, ignition in gas turbines is rather a statistical phenomenon than a deterministic one. Therefore, it is now important to describe how the ignition can fail.
Three general modes of failure were identified in scientific literature that are strictly related to the different stages of ignition [8] pointed out in Ch. 1.
The first one is called *first* or *short mode of ignition failure* and is referred to premature extinction of the flame right after the kernel generation. This can normally be traced back to the slowness of the process that allows the kernel to expand. For instance, it may be caused by a too weak

spark or by an excessive local stretch.
The *second* or *long mode of ignition failure* characterizes the second phase of flame growth [8]. In fact, if the flame growth is prematurely stopped, then the ignition of the whole combustor will fail. A first cause of failure, may be the heat losses due to the evaporation of the spray or to the heat transfer to the surrounding cold fluid. Also the aerodynamic quenching and the fuel starvation may concur to hinder the flame. Such mode of failure is more common than the previous one, as usually the spark is powerful enough to always generate the kernel.
The last mode is referred as *third mode of ignition failure* and is related to the third phase of the ignition process [8]. In this case, after the successful growth, a certain part of combustor is filled by the flame when it suddenly blows off. This mode seems specific of recirculating flows and may be related to non-satisfying conditions inside the inner recirculation zone.
Therefore, under similar conditions, releasing the spark in one point does not exclusively results in a successful event neither in a failed one, but there is a probability of success. This is due to some stochasticity sources that are summarized [8] in:

- the variation in the energy released by the spark;
- the inhomogeneity of the spray, in terms of droplet size and spatial distribution, temperature, etc.;
- the fluctuations in the mixture fraction and in strain rate due to turbulence;
- the additional fluctuations induced by the flame propagation within the combustion chamber.

All of these phenomena are relevant to determine the ignition outcome. Therefore, it makes sense to define the ignition probability P_{ign} as the ratio between the number of successful ignition attempts and the overall number of attempts (both successful and failed).

$$P_{ign} = \frac{n_{succ}}{n_{succ} + n_{fail}} \tag{2.1}$$

Several definitions can then be attributed to *successful ignition*: in experiments or actual combustors, it may corresponds to the successful onset of the flame within a defined timeframe or after a certain number of sparks [4]. Similarly, in academic experiments the successful ignition involves the successful onset of the flame after a single spark deposition (multiple events are not considered). Clearly, P_{ign} represents a very useful

information during the initial design stages along with the time required to complete the flame stabilization.
In scientific literature, also the the probability of generating the kernel is normally introduced. However, in the investigated test case such probability is estimated to be always one, which explains why this point is not further discussed at this stage.

2.2 Ignition probability with reactive LES

Before introducing the available models to compute ignition probability in gas turbine combustors, it is worth pointing out why such *reduced* or low-order models are needed. In fact, one could argue that also a full LES approach could be used to compute ignition probability, if a sufficient numbers of attempts are simulated under different initial conditions.
For instance, in [50] and in [51] an approach based on brute force LES is attempted: the results shown are very promising but the computational effort of 1.5 M CPU hours for 20 spark attempts in each of the 3 selected locations (60 sparks in total, 25000 CPU hours each) [51] is still excessive in early design stages, although the proposed approach could be considered for final validation. Recently, an efficient approach based on high-fidelity hot-flow LES and tabulated chemistry was presented in [52]. A look-up table is generated using a homogeneous reactor for the kernel ignition stage, whereas a flamelet progress variable approach is used for the flame propagation stage. The two different look-up tables are then combined linearly and several LES of the ignition process are performed. The ignition probability is computed as a function of the operating conditions and the kernel characteristics using an uncertainty quantification analysis. In [52], to simulate 803 ignition events approximately 1 M CPU hours were used, leading to a CPU cost of roughly 1200 hours for a single spark discharge.

2.3 Review of existing ignition probability models

If a even lower computational effort is desired, ignition models based on a single simulation (either RANS or LES) of the non-reactive flow field before ignition [8] were proposed. The common idea behind these models is to provide a very fast estimation of the ignition probability for a particular spark location by introducing relevant assumptions, at the expense of a lower physical consistency. In the next, some of this model are summarized.

2.3.1 SPHINTIR

The *Stochastic Particle INTegrator for HIgh-altitude Relight* (SPHINTIR) model, firstly presented in [20], was extensively validated and used to investigate the ignition probability in many configurations, including:

- a methane turbulent counterflow flame [20];
- methane bluff-body flames (non-premixed [20] and premixed [53]);
- a methane non-premixed swirling flame [54];
- methane non-premixed multiple-burners (linearly-arranged [55] and annular [56]);
- a n-heptane swirling spray flame [20];
- a liquid fuelled lean-burn industrial combustor under sub-atmospheric conditions [57].

This method is based on the stochastic tracking of Lagrangian particles, called *flame particles*, that mimic the displacement of the flame by being transported through the computational domain. To this purpose, a specific Langevin equation is used. Cells visited by the flame particles are considered ignited and can emit a new flame particle to simulate the propagation of the flame. Moreover, flame quenching is introduced using a criterion based on the Karlovitz number Ka, which can lead to the particle removal from the domain. The ignition probability is finally computed taking into account the size of the domain portion visited by the flame particle.
Since this model is also used in the present thesis, a throughout description is not carried out in this section and will be addressed later.

2.3.2 I-CRIT-LES

In [58] the I-CRIT-LES model is introduced. The main idea, is to build a set of successive deterministic criteria to be evaluated on a single non-reacting flow realization obtained by LES. Therefore, the ignition process is divided into a series of successive phases of finite and unknown duration. Each of these phases represent a specific mechanism and is characterized by an *ad hoc* criterion that must be fullfilled to continue with the ignition process. If not met, the ignition attempt is considered failed.
Instantaneous local flow properties from of a non-reactive LES are used to feed the model. Starting from a certain time step with an associated

flow field, five consecutive conditions are evaluated for each point under investigation.

1. mixture fraction and spray distribution in the chamber: in order to let the ignition even start, a local ignitable mixture must be present at spark location. A simple condition on the total equivalence ratio (gas and liquid) ϕ_0 is introduced:

$$\phi_0^{low} \leq \phi_0 \leq \phi_0^{high} \tag{2.2}$$

where ϕ_0^{low} and ϕ_0^{high} are the low and high flammability limits. Although this limits are influenced by the characteristics of the spray, these were not considered in [58].

2. Energy deposition and generation of the kernel: after that ignition is triggered it leads to complex reaction processes. If the energy is sufficient, the deposition leads to the creation of a small pocket of hot gas with a temperature higher than a certain ignition temperature T_{ign}. The second criterion reads:

$$T\left(t_{cc}\right) \geq T_{ign} \tag{2.3}$$

where $T\left(t_{cc}\right)$ is the temperature at the time when the liquid reaches saturation t_{cc}. This criterion requires the knowledge of the temporal evolution of gas temperature. Some assumptions are made to express such criterion with in a more convenient form, but they are not reported here for the sake of brevity.

3. Growth and convection of the flame: in this phase, if the vaporization time is smaller than the heat diffusion time, the hot gas kernel may turn into a growing flame, whose size increases at a speed dependent by the local curvature of the flame and characteristic scales involved. Conversely, if combustion is not strong enough, the heat release is not sufficient to compensate the cooling of the gas and the kernel quenches. Therefore, the third criterion reads:

$$\tau_{vap} + \tau_{comb} \leq \tau_{diff} \tag{2.4}$$

τ_{vap}, τ_{comb} and τ_{diff} are the timescales related to vaporization, combustion and diffusion. Combustion can be sustained if the droplet can evaporate and burn before the heat is diffused away from the kernel. The full definintion of such timescales can be found in [58].

4. Wall quenching: the interaction of the generated kernel with combustor walls is now considered. A so-called quenching layer is defined, at a certain distance from the wall, where the kernel cannot be sustained. Anyway, depending on local velocity, it is possible that the kernel leaves this region before being completely quenched. Also, a kernel generated anywhere else, may enter in this region and subsequently be quenched. Therefore, three independent scenarios are identified under this criterion. In the first one, the kernel generated within this layer must fulfill a sub-criterion based on the velocity component normal to the wall to survive. If it is not met, the ignition fails. Conversely, the flame might be transported inside this layer: this represent the second sub-criterion and is summarized by a condition based on wall distance and local velocity. Thirdly, if the kernel is sufficiently far from the wall, it will always survive to this stage.

5. Upstream flame propagation: the propagation of the flame towards the nozzle is known to be one of the main mechanism that eventually lead to flame onset. More accurate approaches are presented later, but they are characterized by a larger consumption of resources. In I-CRIT-LES a rather simple criterion is used instead: although not very accurate, it allows to limit the overall computational effort of the model. It is fulfilled if the turbulent flame speed S_T is larger than the mean flow velocity in the injector direction U, thus:

$$U - S_T \leq 0 \tag{2.5}$$

   For the equation used to evaluate S_T, the intersted reader is addressed to [58].

All of this five criteria must be met in order to ensure a successful ignition. Therefore, at each of the LES snapshots considered, the local ignition probability will either be 0 or 1. Finally, the ignition probability map is built by an ensemble average of the one obtained wuth the independent snapshots.
In [58], the I-CRIT-LES model was tested on two academic configurations ([59] and [14]) and on the MERCATO configuration by ONERA [60, 61].

2.3.3 MIST

The *Model for Ignition STatistics* (MIST) was originally presented in [62] and further developed in [18]. Similarly to SPHINTIR, also this model is based on the tracking of the flame growth, although a presence PDF is

used rather than Lagrangian particles. In fact, the starting point of the model consist in the idea that ignition probability is mainly influenced by two factors: the temporal evolution of the kernel and its possible quenching.
The temporal evolution of the kernel is evaluated with the presence PDF $P_{pres}(\boldsymbol{x}, t)$, that represent the probability of finding a kernel in a certain position $\boldsymbol{x}$ at a given time t. $P_{pres}(\boldsymbol{x}, t)$ is build assuming the a gaussian distribution for the velocity close to the kernel position, where the mean value is the mean velocity from LES and the variance is related to the RMS. Therefore, similarly to SPHINTIR, the velocity field of the non-reactive case is used to compute the displacement and the expansion of the kernel.
If only the presence PDF was used, no information about quenching and flammability would be introduced in the model. Therefore, $P_{pres}(\boldsymbol{x}, t)$ is conditioned by the local Karlovitz number and by the flammability factor. A throughout study about the statistical distribution to be used for the flammability factor is carried out in [62], but it is not reported here for the sake of brevity. Finally, the conditioned kernel presence PDF is integrated into space and time to obtain the ignition probability. To this aim, the final radius of the PDF is evaluated to distinguish among failed and successful ignition events.
The model was recently adapted to two-phase flows in [18]. The presence of the spray is considered by introducing the liquid phase into the flammability factor. Moreover, the tracking of the $P_{pres}(\boldsymbol{x}, t)$ was slightly modified compared to [62].
This approach was validated on gaseous swirling premixed/non-premixed flames [62] and on a spray swirling flame [18]. Moreover, in [18] the optimization of the spark plug position for an actual combustor was attempted showing very promising results.

2.3.4 LIMIT

The *Lagrangian Ignition Map using Inverse Time* (LIMIT) model was recently presented in [63]. This model is similar to the SPHINTIR model, except for the time integration which is performed backward in time to obtain the ignition probability. In fact, if in the SPHINTIR model an initial spark location is assumed and the flame evolution is tracked with a Lagrangian approach, here a final ignitable region is defined and Lagrangian entities are tracked backward in time to find the possible initial locations of the spark. As an advantage, all the sparking locations are evaluated in a single run. Moreover, the *a priori* definition of the final (initial from the LIMIT point of view) ignitable region allows to explore

only the successful paths, thus avoiding to track particles to locations that will certainly fail. This last point also represent one of the shortcomings of the model, since it requires the prior knowledge of the ignitable region. Also in this case a non-reactive simulation of the burner is needed to initially feed the model. At first, the ignitable region must be identified: in [63] this is done using the flammability limits, but also the set of methods used in [58] could be employed. Secondly, a certain number of Lagrangian particles are randomly initiated in this volume and the virtual flame is propagated backwards in time. To this aim, a particle momentum equation is used, where the velocity vector is randomized and reversed compared to the one of the cold-flow solution. Also the flame speed is taken into account to determine the velocity of the flame propagation. Similarly to SPHINTIR, each cell is initialized in an unburnt state. If a cell is visited by a particle during the simulation, it switches to a burnt state. At the end of the simulation, the burnt cells would be all the cells connected to the ignitable region that lead to a successful ignition.
A rather complex strategy is also implemented to *clone* or remove particles in order to enhance the model convergence and keep low the computational effort. For further details, the reader is addressed to [63].
The validation of the model was carried out on a lifted methane jet flame and finally employed to investigate the ignition of a supersonic flameholder.

2.3.5 A PSR based method

In [64] and [65] a model based on *Perfectly Stirred Reactors* (PSR) is introduced. Conversely to the other methods presented so far, in this model a lot of effort is put to obtain a detailed description of the chemical phenomena that follows the spark deposition. In fact, the kernel evolution is simulated using a PSR, which allows to simulate in detail the chemical kinetics involved. This model was specifically studied and validated on a sunken fire igniter for gas turbine combustors and at the present day it has not been used to simulate the whole flame propagation. Moreover, some data from related experiments is used as an input for the unknown variables of the model.
At first, a air/plasma reaction mechanism is used to describe the plasma kernel evolution without considering the fuel. This assumption is motivated by the absence of fuel close to the wall where the spark is discharged. The resulting high-temperature ionized gas is employed to initialize the PSR simulation. Even during this stage, no fuel is still added until a certain *transit time* is reached. In this way, the passage of the kernel through the non flammable region close to the wall is mimicked. Finally,

in a third stage a hydrocarbon-air reaction mechanism is considered for the following kernel evolution. Here a flammable mixture is added with a constant mass flow rate, estimated from the experiments. Also the expansion of the kernel is computed from experiments and the associated increase in mass is included by enlarging the PSR to keep the pressure constant. Randomness is introduced by allowing perturbations to the PSR inflow temperature, the transit time and the equivalence ratio.

2.3.6 More models

In the previous sections only the more relevant models were described. It is worth noting that also other models were presented in scientific literature, but a detailed is not undertaken in this manuscript. For the interested reader, an even more detailed review of ignition probability models can be found in [62].

2.3.7 Final comments on ignition probability models

An attempt of classification was introduced in Esclapez Ph. D. thesis [62], where ignition were divided into:

- *pointwise flow characteristics* models: include all the models that attempt to compute the ignition probability relying only on the local flow properties only. They are usually more accurate to evaluate the fate of the kernel right after the discharge of the spark, but they are not effective/designed to describe the flame propagate across the combustion chamber.

- *Trajectory based* models: they are build to recover the flame displacement and growth within the the combustor. In these models, the phenomena related to energy deposition and kernel formation are considered less relevant and larger attention is devoted to the subsequent phases of flame propagation.

According to [62], only I-CRIT-LES completely falls in the pointwise based models but also the PSR based model proposed by Sforzo et al. [64, 65] can be filed in this category. Instead, the remaining ones can be included in the second group: the wider diffusion of trajectory based models, confirmed by the larger amount of published works, suggests that they are probably more effective in describing the relevant mechanisms of ignition in gas turbine combustors.
This is in agreement with the common idea that in practical geometries, the main mechanism to obtain a successful ignition is the convection of the

spark kernel in the IRZ, that eventually leads to flame stabilization [66]. Because of this, all the phenomena that immediately follow the initial deposition (i.e., the kernel generation phase [8]) can be overlooked, while the following displacement of the kernel is assumed to be more relevant. Since the LIMIT model was presented quite recently, it was not evaluated for implementation within this Ph. D. Only the MIST and SPHINTIR models were considered for the present work. One constrain that one should consider, is the platform where the model must be implemented. In order to exploit the commercial CFD solver ANSYS Fluent [23] to investigate ignition process, the SPHINTIR approach was selected because of the easier implementation. In fact, the existing Lagrangian framework was used for the tracking of the flame particles. Moreover, the frozen flow field required by the model, can easily be interpolate if it is obtained with the same solver. In the next sections more details about the SPHINTIR approach are provided.

2.4 Detailed description of the SPHINTIR model

In the present work, the original version of the SPHINTIR model presented by Neophytou et al. [20] was considered and implemented. The reader interested in a complete overview of all the successive developments of the approach is referred to [20, 55, 56, 57].
As anticipated in the introduction, Lagrangian particles called flame particles are employed to track the flame growth. The tracking of the particles is performed using flow data from a non-reactive simulation, referred from now on as *base* solution. To compute the ignition probability, the fraction of the domain visited by the flame particles is considered. The following steps can be identified (Fig. 2.1):

1. interpolation of the flow field: a specific mesh is used to interpolate the data from the base solution and track the flame particles. The set of variables required by the model includes the velocity, the mixture fraction, the *Sauter Mean Diameter* SMD or d_{32} and the evaporation rate. At the beginning, all the cells composing the domain are set to the *unburnt* state and they will eventually be ignited during the simulation (switching to the *burnt* state). It is important to mention that a specific mesh can be used, which can represent only a specific region of the domain, to reduce the computational effort.

2. Initialization of the spark volume: a certain spark volume is defined by the user and used to initialize the kernel propagation. In this

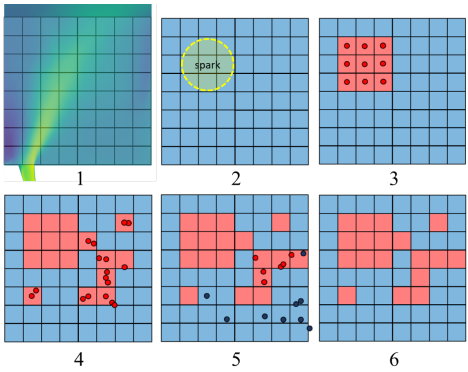

Figure 2.1: Steps of ignition probability computation.

work, an initial spherical shape is chosen, characterized by a radius r_{sp}. Here the mixture is assumed to be already ignited and the preliminary stages of energy deposition and kernel generation are overlooked. It is clear that the amount of energy released by the spark could affect such initial volume, but this relationship is not straightforward as it is probably a complex function of local flow variables. To obtain the local ignition probability, several simulations are performed using the same position of the spark while, to compute the ignition probability map, several spark locations are tested.

3. Flame particles injection: all the cells that overlap the initial spark volume are set to burnt state. They can now release a new flame particle: velocity and mixture fraction are randomly initialized according to a Gaussian distribution for the velocity and a β-distribution for the mixture fraction (using the mean and the RMS of mixture velocity from the base solution).

4. Flame particles tracking: particles are tracked inside the domain using a Langevin equation (Eq. 2.6). The variation of velocity in the i-th direction of the p-th particle is given by:

$$d\boldsymbol{U_p} = -\left(\frac{1}{2}+\frac{3}{4}C_0\right)\omega_p\left(\boldsymbol{U_p}-\widetilde{\boldsymbol{U}}\right)dt + (C_0\epsilon_p dt)^{\frac{1}{2}}\,\boldsymbol{N_p} \tag{2.6}$$

where $\boldsymbol{U_p}$ is the velocity of the tracked particle at the previous

time step dt and $\widetilde{\boldsymbol{U}}$ is the mean velocity from the base solution interpolated onto the new grid. C_0 is a constant assumed equal to 2.0 and $\boldsymbol{N_p}$ is a normally distributed variable (with mean zero and variance unity) [20]. ϵ_p and ω_p represent the turbulent dissipation and the inverse turbulent timescale at particle location respectively. Therefore, particles are convected by the flow and undergo a random walk which allow to include the dispersion due to turbulent fluctuations. Flame particles are also characterized by an overall mixture fraction ξ_p (both liquid and gaseous fuel are considered), whose variation is provided by the following equation:

$$d\xi_p = -\frac{1}{2} C_\xi \omega_p \left(\xi_p - \tilde{\xi}\right) dt + (1 - \xi_p) \frac{\bar{\Gamma}}{\bar{\rho}} dt \tag{2.7}$$

where $\tilde{\xi}$ is the mean overall mixture fraction, $\bar{\Gamma}$ is the evaporation rate and $\bar{\rho}$ is the mean density retrieved from the base solution. C_ξ is a constant set equal to 2.0 [20]. During the tracking of the particles they can visit cells in the unburnt state: in this case, the visited cell is set to the burnt state and emits a new flame particle. Note that cells set to the burnt state can not emit a new flame particle. The amount of emitted particles is a function of the mesh size Δ, which leads to a non-intuitive dependency of this parameter on the ignition probability map, as discussed in Ch. 3.

5. Particle extinction: at the end of each time step, a criterion based on the Karlovitz number of the particle Ka_p is evaluated to assess if particle extinguishes. If $Ka_p > Ka_{crit}$ the flame particle is removed (note that Ka_{crit} is set by the user and represent one the key parameters of the model [20]). Ka_p is defined as:

$$Ka_p = 0.157 \left[\nu \frac{\left(u_p'\right)^3}{L_{turb,p}}\right]^{\frac{1}{2}} \frac{1}{S_{L,p}^2} \tag{2.8}$$

where ν is the laminar kinematic viscosity of the mixture, u_p' the turbulent velocity fluctuation, $L_{turb,p}$ the turbulent length scale and $S_{L,p}$ the laminar flame speed (that should be estimated including the presence of liquid droplets). Compared to [20], here a simpler approach is used to compute laminar flame speed $S_{L,p}$, following the work of [67] and [19]. In fact, the effect of liquid droplets on

flame propagation is included with a rather simple equation:

$$S_{L,p} = D_{th} \left[\frac{\Omega \, d_{32}^2 \, D_{th}}{\Lambda_{eff}} + \frac{D_{th}^2}{S_{L,g}^2} \right]^{-\frac{1}{2}} \tag{2.9}$$

where Ω is the fraction of liquid fuel over the entire fuel mass retrieved from the base simulation. D_{th} and Λ_{eff} stand for the thermal diffusivity of the mixture and the effective evaporation constant. Finally, $S_{L,g}$ represents the laminar flame speed computed using ξ_p and assuming the fuel to be completely evaporated. The reader interested in a comprehensive review about laminar flame propagation in sprays or droplet interaction with the ignition kernel is addressed to [19] and [68] respectively.

6. Final computation of the ignition probability: once that a spark event is completed, the ratio between the *burnt* cells and the overall number of cells is evaluated, defining the ignition progress factor $\pi_{ign} = n_{burnt}/(n_{burnt} + n_{unburnt})$. If $\pi_{ign} > \pi_{ign,crit}$ the ignition event can be considered successful. It is worth pointing out that no general rule is defined to choose $\pi_{ign,crit}$, as it is strongly dependent on the case and the domain under investigation. In the end, the ignition probability P_{ign} is computed as the ratio between the number of successful spark events and the overall number of attempts.

In this way, the model can take into account the effects of mean and fluctuating velocity on flame propagation, the stochastic effect of turbulence and the local extinction due to high turbulent strain rate [20].
Additional details about the implementation of the present model within the ANSYS Fluent framework are provided in Appendix 1.

2.5 Conclusions to Chapter 2

In this section, the definition of ignition probability and the issue of computing it were addressed. At first, the opportunity of directly compute the ignition probability using fully reactive LES was ruled out due to the very large computational effort required. Although it can be useful for final tests, its application is still too expensive during the initial phases of combustor design.
That said, a review of recent ignition probability models was carried out in the attempt of providing to the reader a clear picture of the existing alternatives. In the same section, a comparison among them was reported,

stating the reasons that lead to the choice of SPHINTIR for the present thesis.
Finally, the SPHINTIR approach was described in greater detail in order to fully justify the results reported in the next of this work. The SPHINTIR approach is based on the Lagrangian tracking of the flame front, which is approximated by particles called flame particles. Their displacement accounts for the turbulent transport of the ignition kernel and an extinction criterion is used, based on the mixture fraction.

Chapter 3

KIAI-CORIA lean spray flame

The numerical approaches presented before are now employed to investigate the ignition performances of a laboratory scale combustor. The KIAI-CORIA spray flame was considered in this work and the first section is devoted to describe the rig, the available experimental data and the numerical work already available on it. Then, some details are provided about the strategies employed in the simulations, including numerical methods, different meshes and setup of the models.
The main part of the chapter is composed by the discussion of the results: it starts from a non-reactive LES, continues through the reactive one and ends with the two ignition simulations. The non-reactive simulation is reported to highlight the main flow features and was also used to feed the ignition probability model. In fact, the time-averaged flow field from this simulation was the base simulation for SPHINTIR. Therefore, a detailed validation against experiments was performed to evaluate both the numerical setup and the quality of the results.
After that, the reactive simulation of the stabilized flame is shown, starting from a brief description of the flame structure. Also in this case, an accurate comparison against the experimental data was carried out, pointing out that the overall behaviour of the flame is quite well recovered.
Finally, the two ignition simulations are discussed, starting from the detailed one. The path from spark deposition to full flame establishment was studied and compared against experimental data. Due to the stochasticity of the phenomenon, a rigorous comparison was not possible, but some interesting conclusions about flame development are made anyway. Instead, the results provided by the SPHINTIR model allowed a consistent comparison in terms of ignition probability map: a good agreement is shown, after a careful tuning of the model.

Some of the results presented in this chapter are also part of a master thesis carried out by Matteo Amerighi [69] under the supervision of the author.

3.1 Investigated experimental rig

The experimental rig under investigation is the so-called KIAI-CORIA burner, built in the course of the *Knowledge for Ignition, Acoustics and Instabilities* (KIAI) EC funded project. In this thesis, the single-injector confined test-bench presented in [15, 18, 49, 70] fuelled with liquid *n-heptane* was simulated (Fig. 3.1). It is worth mentioning that other

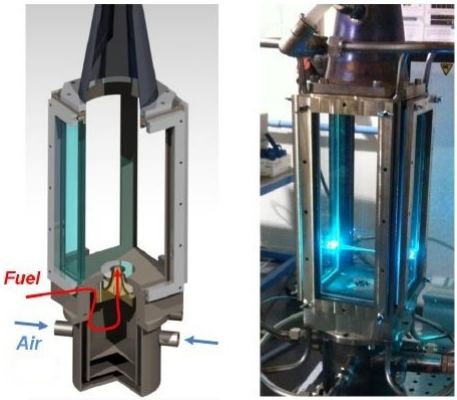

Figure 3.1: Left: render of the KIAI-Spray burner. Right: picture of the burner during the PDA measurements. [5]

configurations were developed and tested so far including:

- methane-fuelled swirled confined single-burner (both premixed and non-premixed) [54, 71]
- methane-fuelled swirled confined multi-burner [48, 72]
- liquid-fuelled non-swirled non-confined single-burner [73, 74, 75, 76, 77]
- liquid-fuelled swirled confined multi-burner [70, 78]

(a) Radial swirler (b) atomizer (c) Sketch of injection system

Figure 3.2: Injection system of KIAI-Spray burner [5].

A throughout review of these works is beyond the scope of this thesis and the interested reader is addressed in the mentioned references.
The combustion chamber 3.1 has a square section of 100 × 100 mm^2, a height of 260 mm and is confined by four quartz windows (78 mm × 228 mm) that provide a full optical access for the non-intrusive measurements. A convergent section is mounted on the top to avoid flow recirculation. The rig was operated at atmospheric pressure.
A plenum feeded with preheated air at 416±3 K the radial swirler (Fig. 3.2(a)), characterized by a swirl number of 0.76 and composed by 18 rectangular channels (6 mm × 8 mm) inclined at 45°. The preheating of air was finely tuned to avoid the formation of a liquid film on the windows. The outlet of the swirler has an inner diameter of 10 mm, while the outer is 20 mm large.
The injection of liquid was performed using a simplex pressure atomizer

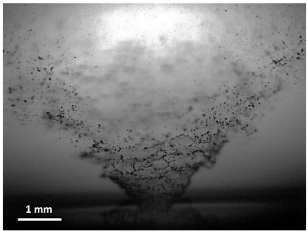

Figure 3.3: Shadowgraphy image in the KIAI-Spray burner showing primary and secondary atomization above the simplex atomizer [5].

(Danfoss, 1.46 kg/h, 80° hollow-cone) represented in Fig. 3.2(b) that discharged the fuel at an estimated temperature of 350 K. Mass flow controllers were used to guarantee a constant global equivalence ratio $\phi_G = 0.61$.
The simplex atomizer is mounted at the centre of the swirler as reported in Fig. 3.2(c). Fig. 3.3 illustrates the liquid issued by the atomizer: at first, the liquid sheet is destabilized and ligaments are generated within the first 2 mm (primary atomization, see Ch. 4). Then, secondary atomization occurs and all the liquid structures are converted into spherical droplets within 4 mm. The operating conditions are summarized in Tab. 3.1. The

Parameter	Value
Operating pressure	1 atm
Air mass flow rate	8.2 g/s
Air temperature	416 ± 3 K
Fuel	n-heptane
Fuel mass flow rate	0.33 g/s
Fuel temperature	≈350 K
atomizer pressure	8 bar
Cone angle	80° hollow cone
Swirl number	0.76
Equivalence ratio	0.61

Table 3.1: Summary of the operating conditions [5].

reader interested in additional details about the experimental configuration is addressed to [5].
In this rig, most of the flow features that can be found in an actual engine combustors are already present. The main limitations from a technical perspective are related to the ambient pressure used for experiments, the absence of cooling features and the single-sector configuration. Anyway, these shortcomings are widely surpassed by the large amount of detailed experimental data, which makes it an ideal candidate for validation purposes, as shown in the next.

3.1.1 Diagnostic and Post-processing

Tab. 3.2 lists all the diagnostics techniques used and the respectively measured quantities.
Phase Doppler Anemometry (PDA) [79] was used under non-reacting and reacting conditions with the aim of measuring the droplet velocity and size distribution. The procedure is based on the scattering of a

Measured quantity	Technique	Flow conditions
Fuel droplet size	PDA	NR & R
Fuel droplet velocity	PDA	NR & R
Air velocity	PDA	NR & R
Air velocity	HS-PIV	NR
Mixture fraction	Toluene-PLIF	NR
Flame structure	OH-PLIF	R
Kernel evolution	HS-Visualization	I
Ignition probability	Probability map	I
Chamber pressure	Pressure sensor	I

Table 3.2: Classification of the experimental techniques used, indicating the measured quantity and the flow conditions. Flow conditions are: NR (non-reactive), R (reactive) and I (ignition).

light interference pattern by the object to measure (droplets in this case). Such measurements were not carried out within the first 10 mm from the injector, due to the presence of very dense spray. It is worth mentioning that PDA was used to measure the velocity of the carrier phase as well, seeding the inflow with very small olive oil droplets.
Also *High-Speed Particle Image Velocimetry* (HS-PIV) [80] was used to measure the velocity of the carrier phase under non-reacting conditions. It is based on the paired imaging of a seeded flow, illuminated by two laser pulses at two instants of known time interval. The displacement of the particles from one image to one other were used to compute the velocity vector on the measurement plane.
Planar Laser Induced Fluorescence on Toluene (Toluene-PLIF) [81] was used to measure the local vapour mixture formation under non-reacting conditions. The objective of this technique is to estimate locally the amount of fuel vapor in the chamber. Later, this can be translated into local equivalence ratio or mixture fraction. N-heptane is not a fluorescent molecule, therefore the fuel was mixed with a certain amount of toluene (2%) characterized by a similar evaporation rates. As soon as it is injected in the chamber, the liquid mixture started evaporating. Then, the concentration of toluene was detected with laser induced fluorescence. Finally, n-heptane concentration was calculated under the hypothesis of conservation of the toluene-to-heptane molar fraction ratio between liquid and vapour.
Planar Laser Induced Fluorescence on OH (OH-PLIF) [82] was used to characterize the stabilised flame structure and stabilisation points. In fact, the OH molecule was used as a tracer for the combustion process.

Similarly, *High-Speed* (HS) Visualisations of the spontaneous flame emission were recorded with an high speed camera to characterize the ignition process.
Finally, the ignition probability was measured to understand how the sparking position and the local flow properties influence the ignition process. The mixture was ignited using a laser-induced spark, with the benefit of the lack of electrodes and the ability of trigger the spark anywhere in the domain. The ignition probability was measured in several points of a 3D mesh performing 30 ignition trials each. The mixture has ignited by focusing a 532 nm laser beam, generated at 10 Hz by a Nd:YAG laser, in the selected location. The amount of energy deposited by the laser was estimated to be around 405 mJ. After a successful ignition event, the wall temperature was monitored and a successive ignition test was allowed only when decreased below 387 K. The reader interested in additional details about the experimental configuration and the diagnostics techniques is addressed to [5].
The first outcome of this set of measurements is the possibility of finely characterize the non-reactive flow prior to ignition. In [5] a detailed description of this field is carried out, starting from the identification of the main flow structures thanks to PDA and HS-PIV results. Moreover, the data from PDA are analyzed, showing the spray evolution within the chamber and allowing a deeper understanding of the equivalence ratio map obtained with Toluene-PLIF.
The ignition probability map and the measurements about the cold-flow provide a nice overview of the flow parameters that facilitate or hinder ignition. Transitory kernel generation and flame growth observation are also made in [5], using the images acquired with HS-Visualization. For instance, kernel images are compared for several position slightly after the spark discharge, to better understand the initial shape and its interaction with the turbulent flow field.
Moreover, it is shown that the very first stage of kernel generation is always accomplished with such setup and the ignition may fail only during the second stage and the third stage. That said, a classification of the main mechanism of ignition success or failure is attempted in [15] More details will be provided in the next, while comparing the experimental data against the ignition results.
Finally, OH-PLIF alongside PDA acquisitions of the stabilized flame allow a better comprehension of the reactive flow that follows the ignition process.

3.1.2 Previous numerical works about the KIAI-CORIA burner

To the best of the author knowledge, the specific configuration here studied was previously object of one numerical campaign only, namely the one of the Ph.D. thesis of Collin-Bastiani [18]. The AVBP LES solver developed at CERFACS and IFPEN was used to simulate the KIAI-CORIA rig. Turbulent sub-grid stresses were modeled using the SIGMA model [83] and a Lagrangian approach was chosen for the spray description: sub-models for drag and evaporation were used, whereas the injection was modelled with FIM-UR approach to mimic a simplex pressure atomizer, following the setup already employed in [73].
The n-heptane fuel oxidation was described using an *Analytically Reduced Chemistry* (ARC) derived from a skeletal mechanism [84] comprising 25 transported species, 27 species in Quasi-Steady State Approximation and 210 irreversible reactions [15, 49]. The use the ARC reaction mechanism, instead of the less complex two-step mechanism employed in this thesis, allowed a more effective description of the ignition process, although the computational effort was strongly increased since the reaction rates could not be solved explicitly anymore. No turbulent combustion closure was employed and the reaction rates in Eq. 1.14 were considered as non-filtered. This was made possible thanks to the very refined meshes employed to simulate the stabilized flame and the ignition process. Finally, the ED model was used to initiate the flame kernel.
A good agreement in the prediction of the gaseous velocity and of spray distribution, as well as of the overall flame shape, was shown. Moreover, reactive LES was used as a complimentary tool to analyze the ignition failure and success mechanism. As an example, one of the successful ignition events in [18] is reported in Fig. 3.4 The reader interested in

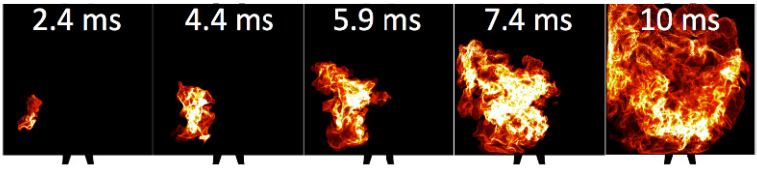

Figure 3.4: Numerical integrated heat release during ignition sequence (adapted from [18]).

more details about this numerical work is addressed in the mentioned references. It is worth pointing out that such simulation setup represents

the current state of the art in the scientific context, but many numerical choices would not be sustainable in an industrial one, because of the huge computational cost associated. Although the simulations presented in this thesis also required a significant amount of computational resources, they are nowadays affordable by an engine manufacturer thanks to the evolution of High Performance Computing infrastructures.

3.2 Setup of the simulations

The simulations were carried out with the methodologies presented in Ch. 1 and 2. From now on, they will be referred as follows:

- *NR-LES*: LES of the non-reactive flow field (with spray injection);
- *R-LES*: reactive LES;
- *I-LES*: detailed LES of the ignition process;
- *I-PROB*: set of simulations to compute the ignition probability map using the SPHINTIR model.

All the simulations performed within this chapter were carried out with the commercial solver ANSYS Fluent.

3.2.1 NR-LES, R-LES, I-LES

A sketch of the numerical domain and prescribed boundary conditions is given in Fig. 3.5. There the spatial coordinates used in the post processing are also defined: *z-coordinate* is employed to indicate the axial distance from the swirler, whereas the radial distance is marked with *r-coordinate*. For convenience, the origin of the reference frame is set in the centre of the domain where the liquid injector is mounted and particle are initiated. The numerical domain included all the components of the experimental rig from the air plenum up to the convergent discharge section. All the other parts were not considered in the simulations.
A constant mass flow rate of air equal to 0.0082 kg/s was specified at the inlet marked in red. The temperature of the incoming flow was set to 416 K according to the experimental setup. No artificial turbulence generator was used as most of the instabilities are believed to be generated through the swirler. A constant pressure was prescribed at the outlet which was also treated as non-reflecting for acoustic waves (blue in Fig. 3.5). All the remaining surfaces are representative of solid walls, so the non-slip condition was imposed. The walls far from the flame were considered as

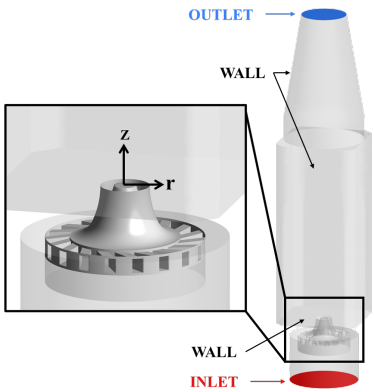

Figure 3.5: Numerical domain and grid for LES.

adiabatic, whereas a specified temperature was set for the ones which mostly interact with the flame. Therefore, the swirler was set to 416 K, assuming that it reached the temperature of the incoming airflow (the swirler was not cooled in experiments). Conversely, the temperature of the walls of the combustion chamber was selected based on the flow conditions. In the NR-LES and the I-LES simulations, it was set according to the temperature reached by experimental sensor after each ignition test, namely 387 K. Instead, it was set to 1000 K in the R-LES according to [15, 49].

To track liquid dispersion inside the combustion chamber, a coupled Eulerian-Lagrangian formulation was adopted to represent the spray dynamics and gas-liquid interactions (Ch. 1). All the phenomena related to the primary breakup of the spray are overlooked in this approach and the particles are directly injected at at $z, r = 0.0$ mm following a Rosin-Rammler distribution [85]:

$$1 - Q = exp - (D/X)^q \tag{3.1}$$

$$\frac{SMD}{X} = \left[\Gamma\left(1 - \frac{1}{q}\right)\right]^{-1} \tag{3.2}$$

A *Sauter Mean Diameter* (SMD) of 30 μm was imposed with a dispersion parameter $q = 2.5$ following the work of Shum-Kivan [86]. The injection velocity of 27 m/s was instead derived from correlations [85]. The initial

temperature of the fuel is set at 350 K according to the experimental estimations.
It is important to note that such injection setup was chosen in [86] thanks to the detailed experimental results that allowed a fair guess of the SMD and of the cone angle of the spray. As it will be shown later, it provides quite a good agreement with the experimental data, that again were used to validate it. This short remark would like to emphasize the help provided by the experimental spray measurements in liquid injection setup. When not available (Ch. 4), the situation changes dramatically!
Three fully unstructured meshes were generated for the simulations. Fig. 3.6 shows a slice of the mesh for all cases with a magnification in the flame stabilization zone. The NR-LES mesh is the coarsest one as only the

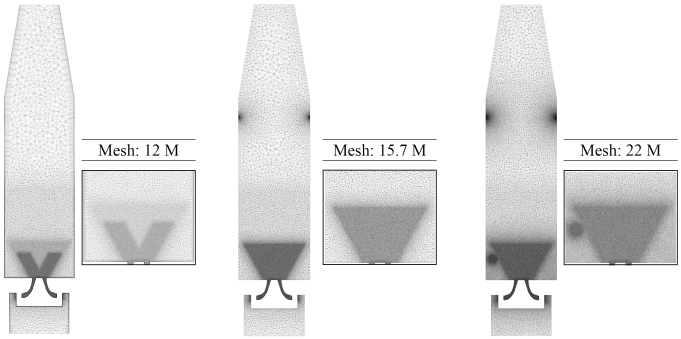

(a) NR-LES (b) R-LES (c) I-LES

Figure 3.6: Meshes used for NR-LES (a), R-LES (b) and I-LES (c).

turbulent mixing process takes place in this simulation and the minimum cell size is around 0.4 mm inside the swirler and in the jet region. A larger size was adopted out of it, because no relevant phenomena takes place elsewhere. A layer of 12 prisms adjacent to solid walls was created in the initial attempt of well-resolving the turbulent eddies close to the wall.
In the reactive simulations (R-LES and I-LES) an additional refinement inside the swirler and in flame region was applied to better resolve the flame structure and to place more points within the thickened flame front. Moreover, in the I-LES a refinement in the spark position was introduced, which is necessary to capture the kernel evolution. At the same time, a finer mesh was used in the ORZ where kernel development may take place

as highlighted in [15]. In these two simulations, only 3 layers of prisms were created at wall: this was possible by the generally smaller size of the mesh that already resulted in a better discretization of the eddies close to the wall. This was also done to reduce the computational effort, assuming that the heat transfer is not so relevant in this case.
In all the presented meshes, the cells gradually increase in size up to the discharge zone, since here there is no need to resolve in detail the flow structures. Moreover, bigger cells result in a numerical damping of pressure fluctuations reflected on the outlet patch.
Clearly, not all the models presented in Ch. 1 were used in all the simulations: Tab. 3.3 summarizes the models employed in each case.

Simulation	Turbulence	Spray	Combustion	Spark
NR-LES	•	•	○	○
R-LES	•	•	•	○
I-LES	•	•	•	•

Table 3.3: Summary of the models employed for each simulation.

As already stated in Ch. 1, LES was chosen for its superior performance in representing swirling flows compared to RANS and because of the need of carrying out unsteady simulations. However, RANS solutions were still used to initialize the NR-LES and the R-LES cases, whereas the I-LES was directly started mapping the flow field from NR-LES. In LES, the WALE [24] sub-grid scale model was used to model the unclosed terms of the Reynolds stress tensor.
Lagrangian sub-models were adopted for the spray particles displacement, heating and evaporation. No secondary breakup was introduced as it is believed to have a minor impact on the solution due to the relatively low Weber number of the injector. The non-deformable drag law by Morsi [39] was applied to introduce the mutual effect of momentum exchange between the continuous and the dispersed phase. Under the assumption of uniform temperature inside the droplet [41], evaporation was modelled as explained in Ch. 1 using data from [87] for the thermo-physical properties of n-heptane.
The turbulent sub-grid combustion model were used in reactive simulations only. The TFM was adopted as specified in Ch. 1. Regarding the efficiency function, the formulation by Colin et al. [27] was used as it is already implemented in ANSYS Fluent [23]. The laminar flame speed and thickness necessary to feed the model were computed with CANTERA [38] employing the 2-step reaction mechanism used in the simulations.

In the I-LES simulation, the ED model implemented with UDF and shown in Ch. 1 was used. The control parameters are summarized in Tab. 3.4. The spark position was selected in the ORZ based on the experimental

ED parameter	Value
Energy E_i	25 mJ
Duration Δ_t	100 μs
Sphere diameter Δ_s	8 mm
Spark position	x = 40 mm and z = 30 mm

Table 3.4: ED setup.

ignition probability map due to the high ignition probability (over 80 %). A pressure-based solver was used and the SIMPLEC algorithm was employed for pressure-velocity coupling. Spatial discretisation was treated with Green-Gauss node-based method method for the gradients, Second Order for the pressure, Bounded Central Differencing for the momentum and Second-Order Upwind for all the other equations. A Bounded Second-Order Implicit formulation was used for time. A constant time step of 8×10^{-6} s was chosen for the NR-LES whereas 1×10^{-06} s was used in R-LES and I-LES. The computational cost of the I-LES was about 100k CPU hours on 400 cores (Intel® Xeon® Core™ Bronze 3204).

3.2.2 I-PROB

The specific domain employed for the computation of ignition probability is illustrated in Fig. 3.7. It consists only of a small part of the domain used for the LES simulations, including only the regions of flame propagation and stabilization. A large part of the combustion chamber and the whole swirler were not modelled. This choice allowed a further reduction of the computational effort required.
A uniform hexahedral mesh was used to track the flame particles, using a constant physical time step of 0.2 ms for a maximum simulated time of 60 ms for a single ignition event. $S_{L,g}$ was computed as a function of ξ_p with the POLIMI reaction mechanism [37] using Cantera [38] at the experimental temperature and pressure. A uniform value of $L_{turb,p} = 1.0$ mm was assumed in this case.
To obtain a single ignition probability map shown in the next section, 6000 simulations were carried out: 120 evenly spaced spark locations (marked in Fig. 3.7 with red dots) were tested for 50 times each one. About 1000 CPU hours were requested to compute a single ignition probability map on a desktop PC equipped with Intel® Core™ i7-7800X.

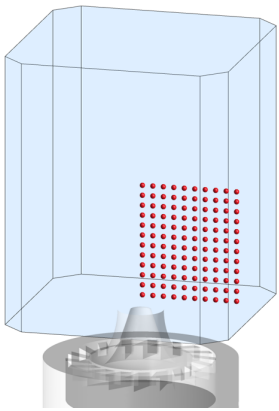

Figure 3.7: Numerical domain used to compute ignition probability and investigated spark positions.

3.3 NR-LES results

A throughout validation of the NR-LES is quite useful, not only to validate the employed setup, but also because the results were directly used to feed the SPHINTIR model and to initialize the I-LES before the spark was released (although the mesh was changed). The simulation was initialized with a preliminary RANS, but such results are not reported here for the sake of brevity. After that, a certain time interval was simulated in LES to flush the initialization, before starting to collect the statistics shown in the next paragraphs.

3.3.1 Gaseous flow dynamics

The time-averaged and the instantaneous flow field of the axial velocity are reported in Fig. 3.8. Three main zones can be identified: the *Inner Recirculation Zone* (IRZ), the *Swirled Jet Zone* (SJZ) and the *Outer Recirculation Zone* (ORZ). The iso-line $u_{axial} = 0$ in Fig. 3.8 drawn in white separates each zone. The presence of the IRZ is justified by the swirl number larger than 0.6 but, compared to actual combustors, the IRZ is less pronounced and quite smaller than the ORZ [5]. Thanks to the presence of the convergent section at the outlet, the IRZ is confined to the vicinity of the nozzle (not shown in Fig. 3.8). The reverse flow

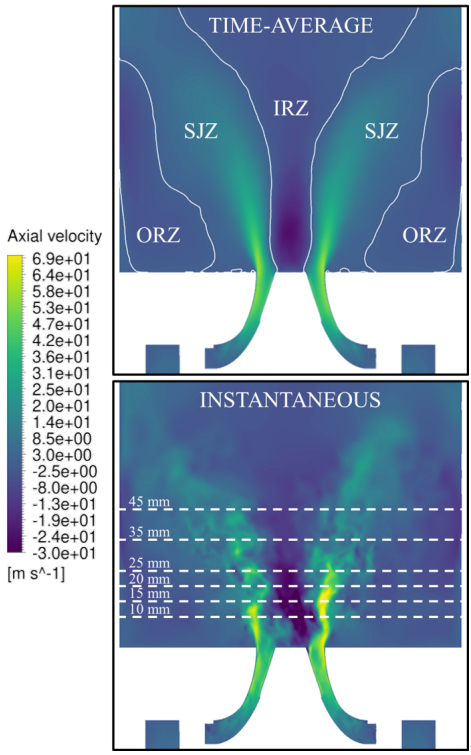

Figure 3.8: Contour of the NR-LES axial velocity flow field. Top: time-averaged field with $u_{axial} = 0$ iso-line. Bottom: instantaneous field with the dotted lines that represent the six experimental stages considered.

in the IRZ has a typical bottle-neck shape caused by the radial velocity, with very thin cross-section at the low axial positions, whereas it gets wider downstream.
To validate the flow field against experiments, time-averaged velocity profiles for different z-coordinates are reported and compared with data from PDA (Fig. 3.9). The six axial stages used to draw the lines are highlighted in Fig. 3.8 for the sake of clarity. Also in this case, the

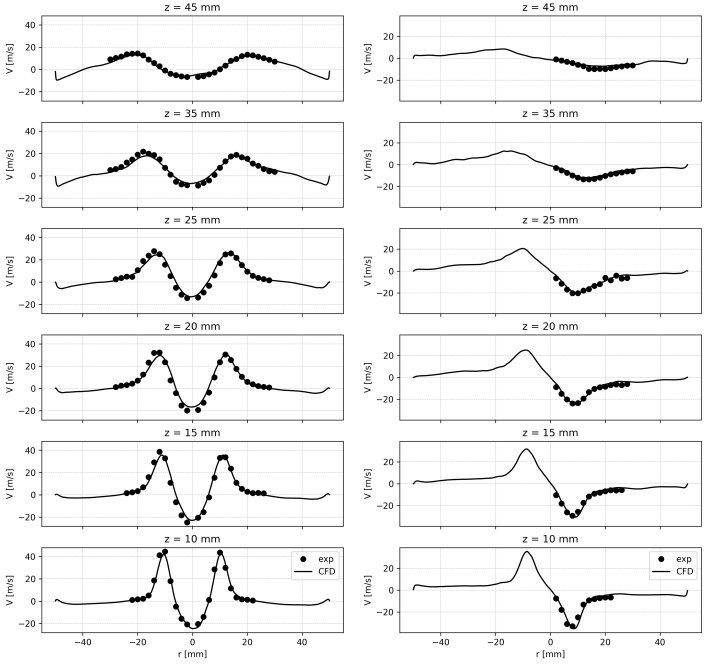

(a) Mean axial velocity (b) Mean tangential velocity

Figure 3.9: Comparison between numerical and experimental data at different heights for mean axial (a) and tangential (b) velocity.

presence of the IRZ and the ORZ, characterized by a negative axial velocity, can be easily pointed out. A very high axial velocity in the SJZ can be observed at $z = 10$ mm, which gradually fades for higher z-coordinates. A good agreement with the experimental data can be pointed out: a proper evaluation of the velocity flow field is fundamental

to correctly describe the trajectory of the flame during the third phase, both in the I-LES and in the I-PROB simulations.
Instead, a key parameter for the flame growth is the local turbulence intensity. Therefore, gaseous velocity fluctuations are presented in Fig. 3.10 in terms of RMS. An overall good agreement can be pointed out, thanks to the use of LES which allows to resolve a large part of the turbulent kinetic energy spectrum (i.e., the grid is fine enough to capture the larger turbulent fluctuations). The fluctuations are larger in the jet region, whereas they decrease in the IRZ and almost vanish in the ORZ. At $z = 45$ mm the mesh is coarser so the comparison with the experiment is not as good as in the upstream stages. The velocity fluctuations are

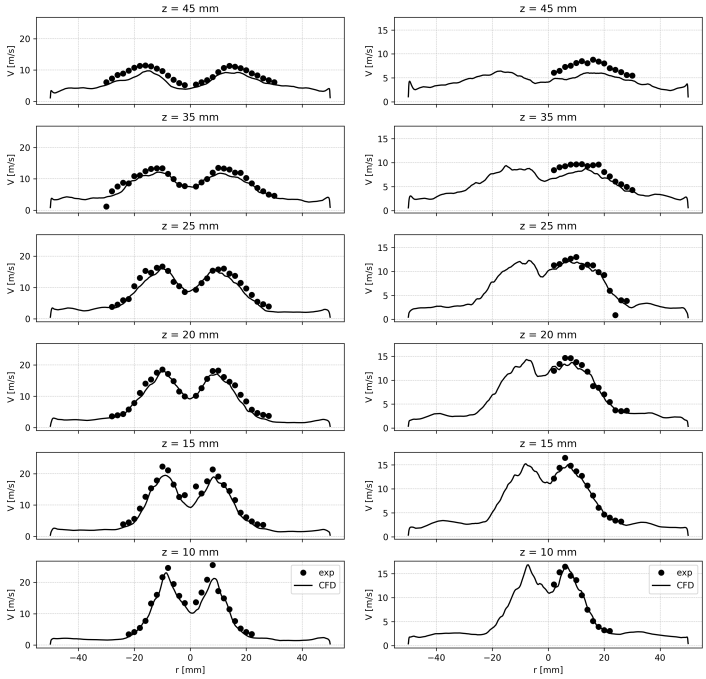

(a) RMS axial velocity (b) RMS tangential velocity

Figure 3.10: Comparison between numerical and experimental data at different heights for RMS axial (a) and tangential (b) velocity.

very important in the ignition process, as they can provide fresh gases to sustain the flame kernel, but also promote the diffusion of heat away from it. A proper prediction is therefore fundamental for the I-LES. Moreover, in the SPHINTIR model they are used to account for the random motions of the kernel and therefore they must be well estimated. Finally, such comparison also implies that the mesh size is fine enough to capture most of the turbulent eddies registered experimentally. Therefore, no mesh sensitivity was carried out at this stage, also considering the relevant amount of computational resources needed for this kind of simulations.

3.3.2 Liquid fuel dynamics

The presence of liquid droplets is of paramount importance in determining the outcome of an ignition attempt [8]. In fact, the generated kernel must be sufficiently strong to survive despite the latent heat absorbed by droplet vaporization. However, the vaporization of fuel is also necessary to sustain and stabilize the flame. Therefore, a proper prediction of spray distribution is extremely important for the outcome of ignition simulations.
The comparison between experimental and numerical data in terms of SMD is shown in Fig. 3.11 (points are plotted only if the SMD computation is based on more than 1500 droplets). For a consistent comparison againts experimental data, spray statistics were also collected circumferentially as well as averaged in time. It is important to note that the same procedure was not applied to gaseous phase velocity data, that are just averaged in time and collected over a line. A proper prediction of the SMD is recovered in the ORZ (large r-coordinate), while a slight under-prediction can be noticed close to the axis ($r = 0.0$ mm). On the one hand, it can be concluded that spray SMD was correctly initialized, as suggested by the overall good agreement in the ORZ and in the SJZ. The poly-dispersion in these two regions is shown in Fig. 3.12(a) and 3.12(b) where the droplet size distribution is reported for two of the three points shown in Fig. 3.15. On the other hand, the under-estimation of the SMD in the IRZ (Fig. 3.12(c)) might be due to a poor representation of fuel droplet convection caused by the recirculation zone. Based on these observations, the description of the SMD distribution by NR-LES is globally acceptable at all the considered stages.
The experimental data are further exploited considering the liquid phase velocity to validate the liquid injection setup. Such input is not considered in SPHINTIR, although it might be relevant for R-LES and I-LES simulations. It is worth pointing out that the spray is mostly composed by small droplets with a low Stokes number. Therefore they rapidly achieve

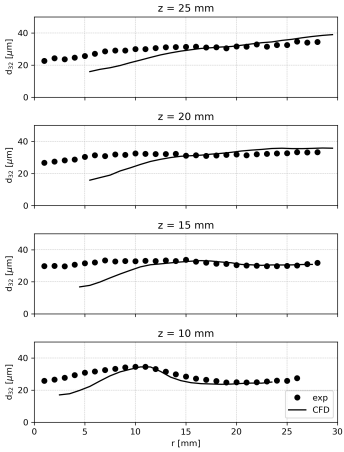

Figure 3.11: Comparison between numerical prediction and experimental data in term of SMD at different heights.

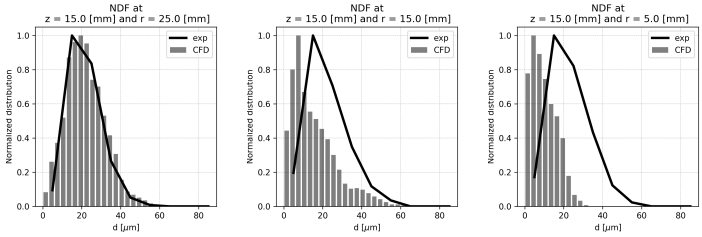

(a) ORZ (b) SJZ (c) IRZ

Figure 3.12: Comparison between experimental and LES normalized distribution of droplet diameter at three points highlighted in Fig. 3.15. (a) P_{ORZ} : $r = 15$ mm,$z = 25$ mm , (b) P_{SJZ} : $r = 15$ mm,$z = 15$ mm , (c) P_{IRZ} : $r = 15$ mm,$z = 5$ mm

the velocity of the gas phase that, if well predicted, will provide a good agreement also in terms of liquid phase velocity. Four mean profiles are reported in Fig. 3.13 for two classes of droplet diameter: $d_p \in [0; 10]$ μm and $d_p \in [40; 50]$ μ. Only a small under-estimation can be pointed for the

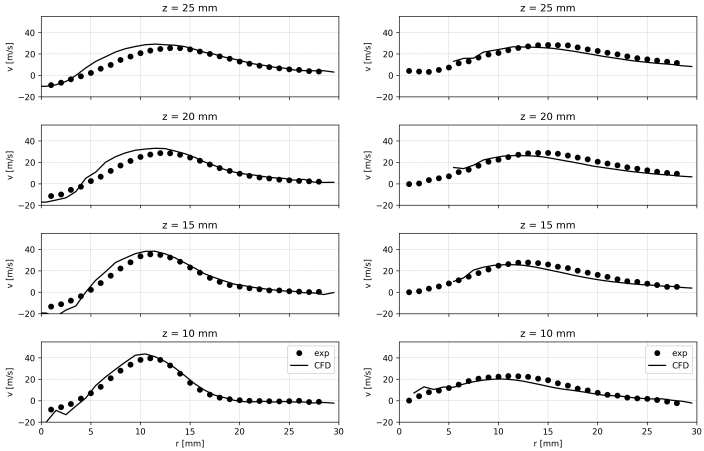

(a) $d_p \in [0; 10]$ μm (b) $d_p \in [40; 50]$ μm

Figure 3.13: Comparison between numerical and experimental data at different heights for mean axial droplet velocity. (a) $d_p \in [0; 10]$ μm. (b) $d_p \in [40; 50]$ μm.

bigger droplets at all the considered heights.

3.3.3 Equivalence ratio

Obviously, the local amount of fuel (i.e., mixture fraction, equivalence ratio) is critical in ignition, as it determines the possibility to translate the energy deposited by the spark into actual flame propagation.
In Fig. 3.14 the mean equivalence ratio is shown both with and without the liquid contribution. The shaded area on the experimental side is not quantitatively reliable, due to the large presence of droplets that does not guarantee a proper measurement with the Toluene-PLIF technique (see [5] for further discussion on this controversial point). Thanks to the decent agreement shown for velocity and droplet distribution, also the prediction of the equivalence ratio is quite good. In particular, as

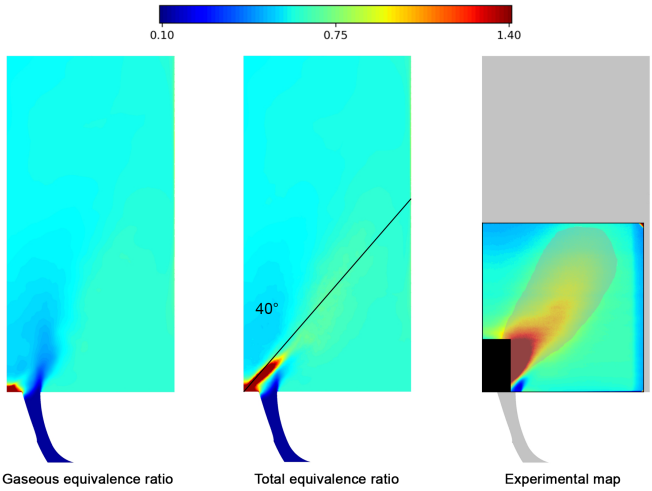

Figure 3.14: Contour of the NR mean equivalence ratio (excluding and including spray) and experimental map adapted from [5].

verified experimentally, in the ORZ the ϕ_g is slightly larger than the global equivalence ratio of the chamber ($\phi_{global} = 0.61$) due to the higher presence of liquid droplets and fuel vapor recirculation. Conversely in the IRZ and SJZ it is leaner because of the lower residence time of droplets that does not allow their complete evaporation. Therefore, in these two zones a less favorable condition for the ignition of the mixture must be accounted.
By including the fuel droplets, it is possible to identify the cone angle of the spray (80°, as per nominal value of the nozzle) and the global equivalence ratio. The high value of ϕ_{tot} near the injector is caused by a high presence of fuel droplets, as reported in Fig. 3.15. In fact, in these zones, the liquid volume fraction is over 10^{-4} and only downstream reaches the value of 10^{-6}.

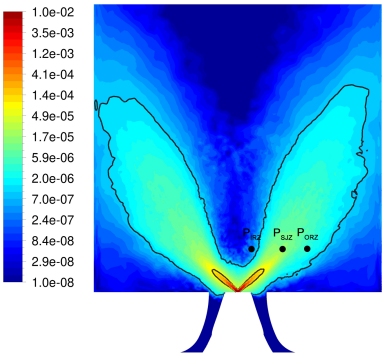

Figure 3.15: Contour of the NR-LES mean liquid volume fraction. The two iso-lines (10^{-4} and 10^{-6}) and the three points (P_{IRZ},P_{SJZ},P_{ORZ}) used in Fig. 3.12 are reported.

3.4 R-LES results

The R-LES simulation was used to investigate the capability of the chosen reaction mechanism and combustion model to reproduce the structure of the stabilized lifted M-shape spray flame. Also in this case, an extensive validation against the available experimental data was carried out, in order to validate the setup for the I-LES simulation. In the next, the focus is firstly devoted to the description of the velocity field and of the liquid distribution. After that, the flame structure is analysed showing a proper prediction of the features observed experimentally.

3.4.1 Flow dynamics and liquid fuel distribution

Fig. 3.16 shows the instantaneous temperature field: the fresh air that is injected from the swirler, rapidly undergoes to a strong heating due to the combustion taking place. The presence of large eddies, with strong temperature gradients, again corroborate the use of LES for turbulent combustion. In fact, the temperature field has a huge role in droplet evaporation and it must be properly recovered. For instance, a certain entrainment of hot gases can be seen in the IRZ, which supposedly has a strong interaction with the spray. It is worth pointing out that the presence of very hot gases in the IRZ as in Fig. 3.16 was observed only

occasionally.
Four z-coordinates are also plotted which correspond to the ones used in Fig. 3.17 to compare the mean velocity field with the experimental data. The main characteristics of a swirling flow remain clearly visible

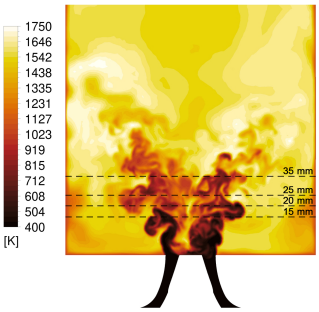

Figure 3.16: Contour of the R-LES instantaneous temperature field with the four dotted lines for the experimental comparison.

also the reactive simulation. In fact, the presence of the IRZ, the ORZ and the SJZ can be still pointed out (Fig. 3.17). The combustion process induces some modifications in the flow field: due to the reduction of the density, the maximum value of the mean axial velocity is greater than under non-reactive conditions (for instance, a peak above 45 m/s can be pointed out at low z-coordinates). Here, the minimum velocity in the IRZ is slightly underestimated by the CFD as well as the maximum peak of velocity in the SJZ. As it will be shown later, it may be due to an underprediction of the flame lift, which may cause an excessive blockage of the air flowing out of the swirler. Conversely, a quite good agreement is obtained for the tangential velocity.
The presence of the flame also induce an higher unsteadiness of the flow field with respect to the NR-LES. In fact, the velocity RMS for the same four coordinates are characterized by an higher intensity, as reported in Fig. 3.18. Despite the general underestimation of the mean axial velocity, the LES well predicts the magnitude of the velocity fluctuations thanks to the mesh refinement operated in the flame region.
In Fig. 3.19 the SMD is compared with the experimental data for the four z-coordinates shown in Fig. 3.11. As already done under non-reactive conditions, data are plotted only if the SMD calculation is based on more

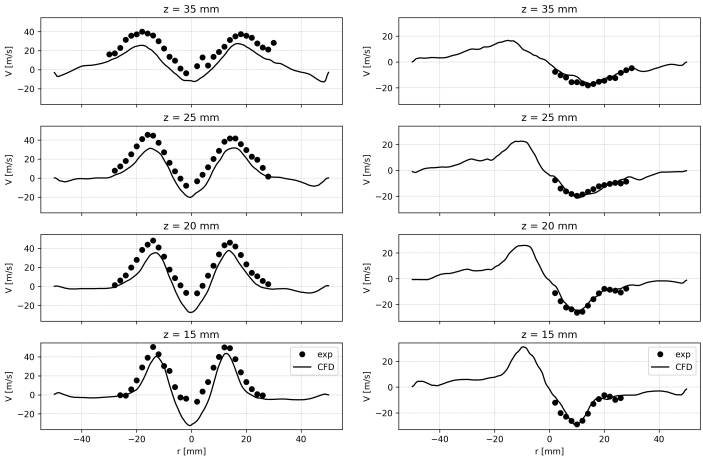

(a) Mean axial velocity (b) Mean tangential velocity

Figure 3.17: Comparison between numerical and experimental data at different heights for mean axial (a) and tangential (b) velocity.

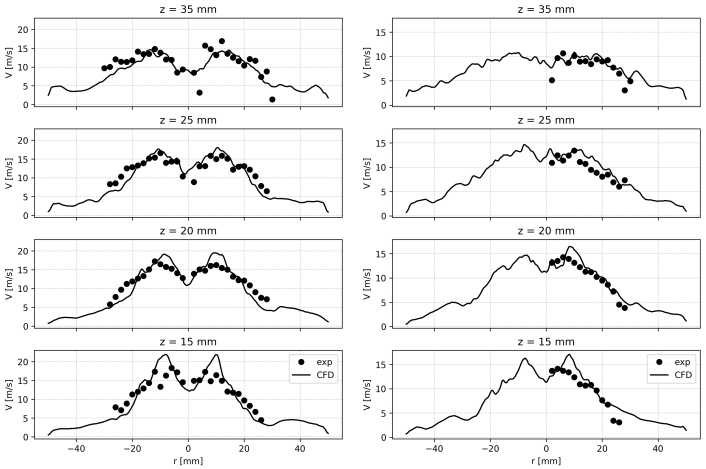

(a) RMS axial velocity (b) RMS radial velocity

Figure 3.18: Comparison between numerical and experimental data at different heights for RMS axial (a) and tangential (b) velocity.

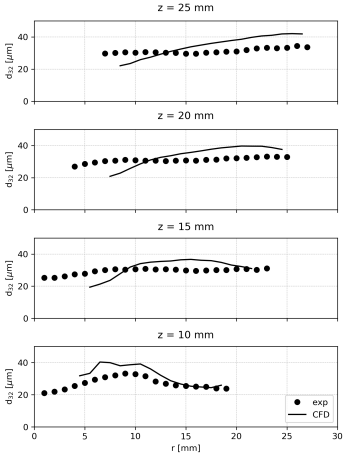

Figure 3.19: Comparison between numerical prediction and experimental data in term of SMD at different heights.

than 1500 droplets. A decent agreement can be pointed out also in this simulation. While the global SMD is mostly correct, the simulation also succeed in catching the evolution of the curve, which progressively becomes more and more flat. This is probably due to the faster evaporation of the smaller droplets that do not survive up to the higher stages. Also in this case, a certain underestimation in the IRZ can be pointed out. The instantaneous distribution of the DPM coloured by their mass is

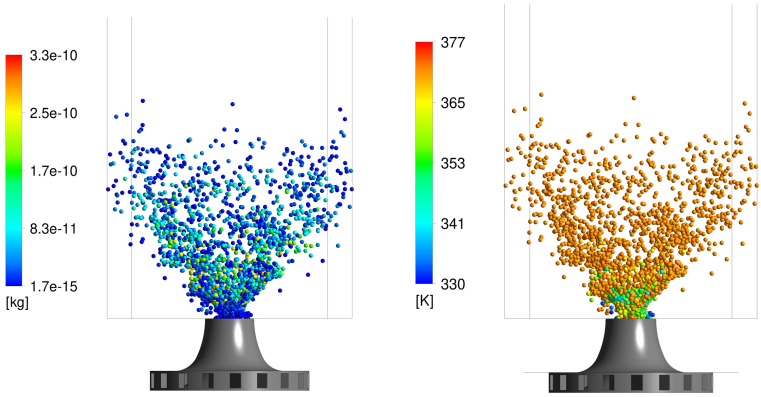

(a) DPM mass (b) DPM temperature

Figure 3.20: Instantaneous of DPM mass (a) and temperature (b).

reported in Fig. 3.20(a). It is important to highlight how some particles successfully cross the flame region and eventually reach the combustor wall. No film accumulation was observed in the experiments and in fact their mass is very low. As illustrated in Fig. 3.20(b), downstream the injector the droplets fastly reach the boiling temperature which involves a significant increase in the evaporation rate with respect to the NR-LES simulation.

To this aim, a comparison in terms of evaporation rate is shown in Fig. 3.21. This highlights how the presence of the flame shifts the evaporation zone upstream, closer to the injector.

For further validation, the mean velocity for the liquid phase is reported in Fig. 3.22 for the $d_p \in [0; 10]$ μm and the $d_p \in [40; 50]$ μm classes size: the agreement is quite good for both classes. Smaller droplets already reach a high velocity at the first stage: because of the lower Stokes number they

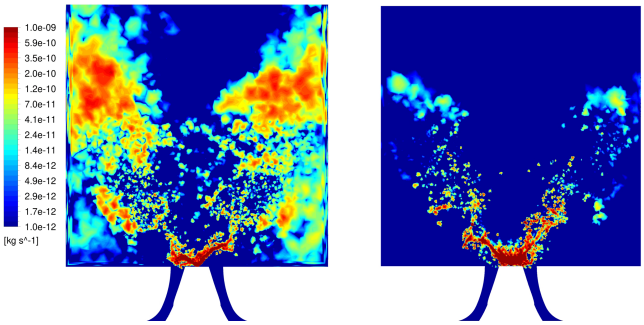

(a) Non Reactive (b) Reactive

Figure 3.21: Contour of the instantaneous evaporation rate for the (a) NR-LES and the (b) R-LES simulations.

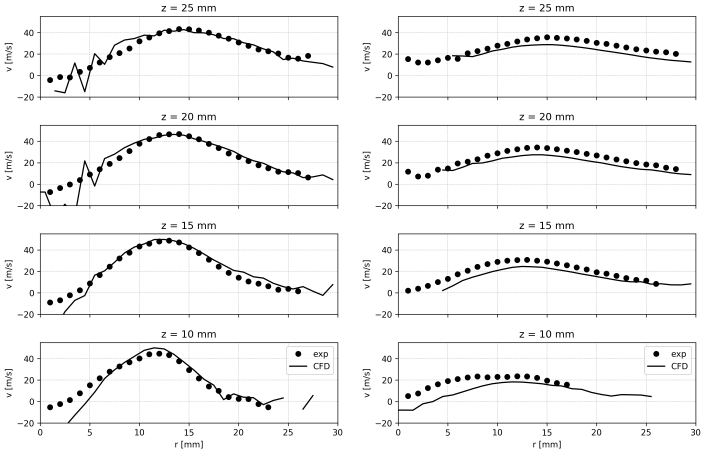

(a) $d_p \in [0; 10]$ μm (b) $d_p \in [40; 50]$ μm

Figure 3.22: Comparison between numerical and experimental data at different heights for the mean axial velocity. (a) $d_p \in [0; 10]$ μm. (b) $d_p \in [40; 50]$ μm.

promptly achieve the gaseous phase velocity. Conversely, the larger class needs more time to adapt to the carrier phase velocity as it continues to increase downstream.

3.4.2 Flame structure

In the KIAI-spray burner a typical lifted M-shape spray flame was observed. In the experiments, the OH-PLIF technique allowed to visualize a section of the flame as shown in Fig. 3.23(a). Even if the shape of the flame can be identified quite well with this image, a quantitative measure of the OH mass fraction cannot be constructed. From a numerical perspective, the analysis of the flame structure was carried out by directly showing the mass fraction of the OH radical. As reported in Ch. 1, Y_{OH} is not transported and it is not included in the reaction mechanism. Therefore, the strategy shown in Sec. 1.6.3 based on the partial equilibrium assumption was employed. For instance, one instaneuous distribution of OH is reported in Fig. 3.23(b). Here, five main zones were highlighted: a

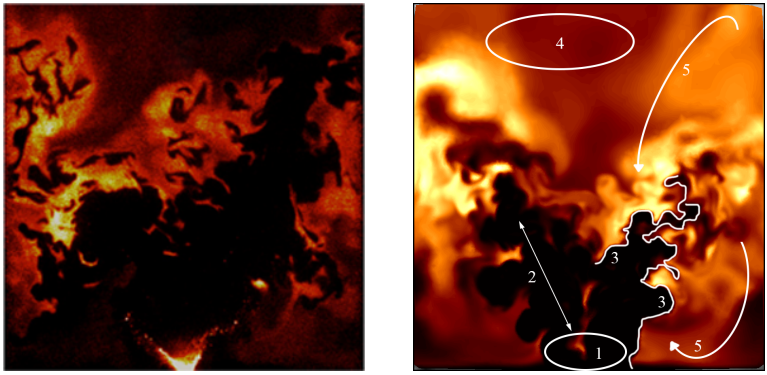

(a) Experimental (b) R-LES

Figure 3.23: Comparison between experimental OH-PLIF image (a) adapted from [5] and instantaneous OH field from LES (b)

first zone immediately downstream the atomizer, where some pockets of OH can recirculate due to the IRZ. The intermittent presence of OH in this area was documented also in the experiments and can be associated with random reductions in the flame length. In the experimental picture, also the spray is visible due to the measurement technique employed. A

second zone is indicated, which follows the trajectory of the droplets and of the swirling jet. Here, the fresh mixture (dark regions) separates the IRZ from the ORZ. The third zone outlines flame front, where a strong gradient of OH indicates the area where reactions take place. Ideally, two flame fronts may be identified, an inner and an outer one, depending on the recirculation zone they are in contact with. A lower mass fraction of OH is found in the fourth zone, where it is progressively oxidized. In this zone the temperature is quite high, because the combustion process is mostly finished and the cooling of the windows is not relevant. The IRZ and the ORZ (fifth zone) allow the flame to be sustained be providing hot burnt gases to the flame front.
A more reliable representation of the flame front is displayed in Fig. 3.24 where the heat release is plotted (both instantaneous and time-averaged). Such data is not directly available from experiments: therefore only the comparison in terms of OH was possible to validate the numerical flame shape. In Fig. 3.24(a) a snapshot of heat release distribution is shown,

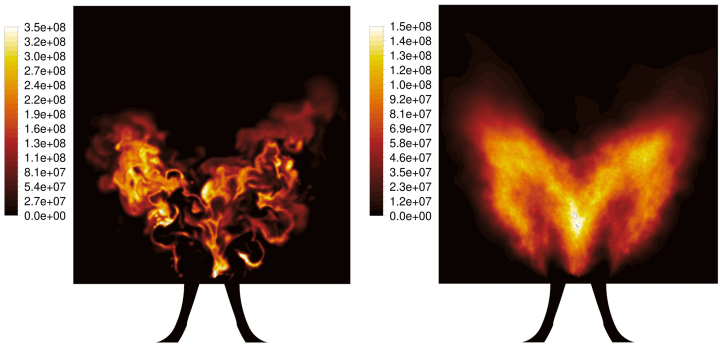

(a) Instantaneous (b) Mean

Figure 3.24: Contour of the heat of reaction per unit of volume: (a) instantaneous field and (b) mean field.

that allows to identify the actual position of the flame front. A very strong unsteadiness can be pointed out: the large eddies issued by the swirling flow strongly interact with the combustion process, further justifying the need of using LES for a proper prediction.
The lifted M-shape of the flame is even more evident in Fig. 3.24(b),

where the time-averaged heat release is shown. The large fluctuations seen in the previous picture, are identified by the large thickness of the time average reaction zone.
Finally, in Fig. 3.25 the mean OH fields are reported for experiments and CFD. Again, no quantitive scaling is attempted because such information is not available from experiments, therefore normalized contours were plotted. A decent agreement can be pointed out, although a general

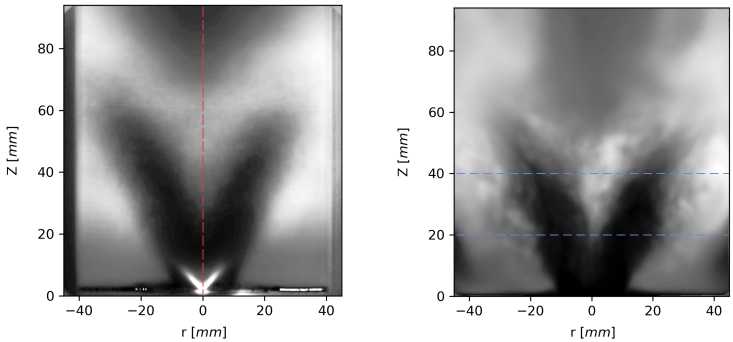

(a) Experimental (b) LES

Figure 3.25: Comparison between mean experimental OH-PLIF image (a) and mean OH field from LES (b). The blue and red dotted lines show the experimental sections used in Fig. 3.26 and Fig. 3.27 respectively.

underestimation of the flame height is recovered. In particular, a deeper entrainment of the OH radical inside the IRZ is obtained with the simulation. In Fig. 3.26 the difference between experimental and numerical prediction is plotted over the red dotted line of Fig. 3.25. It can be noticed that the OH concentration is shifted downstream in the CFD simulation. This is consistent with the non optimal estimation of the size of the IRZ highlighted before. At the present day it is not clear what generates such discrepancies, even if the setup of the combustion model and the employed reaction mechanism must be held accountable, considering the very good prediction of the flow field obtained in the NR-LES.
The height of the flame seems to be slightly overestimated in the whole domain: in fact, a steeper production of OH is also recovered in the

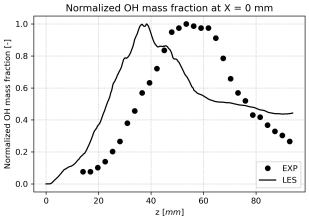

Figure 3.26: Normalized vertical profile (red line in Fig. 3.25(a)) of mean OH mass fraction from experiments and R-LES.

the upper part of the M-shape. This may be due to the very simplified approach used to model chemistry. A more detailed mechanism was employed in [49], obtaining a more precise description of the flame shape. In

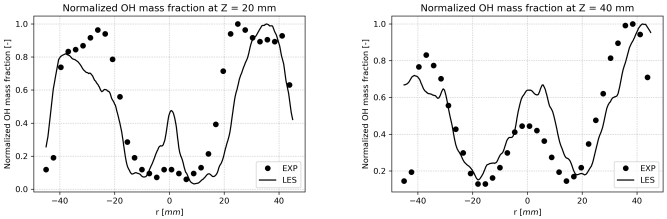

(a) (b)

Figure 3.27: Normalized horizontal profiles (blue lines in Fig. 3.25(b)) of mean OH mass fraction from experiments and LES results. (a) Profile at $z = 20$ mm. (b) Profile at $z = 40$ mm.

the end, two normalized horizontal profiles are reported in Fig. 3.27 from the blue dotted lines seen in Fig. 3.25(b). Two stages were drawn, in the attempt of quantitatively assess the differences in the flame shape. Again, the underestimation of the height in the IRZ is quite evident although a the flame width is better estimated by the computation. This probably relates with a better prediction of velocity obtained in the ORZ and in the SJZ.

It can be argued that the comparison against the experimental OH distribution could also be undertaken using the heat release data. In fact, this leads to a quite satisfactory comparison when instantaneous images

are considered since the experimental OH concentration mostly coincides with the peak regions of the numerical heat release (see Fig. 1.6 and 1.7). However, if time-averaged quantities are considered, then the situation is quite different: by comparing the mean heat release from CFD (Fig. 3.24(b)) and mean OH from experiments (Fig. 3.25(a)) the agreement is all but good, since the heat release fails to identify the amount of OH that is not oxidized after the flame front and that recirculates with the other hot gases in the IRZ and the ORZ. Conversely, the use OH mass fraction, predicted by the equilibrium assumption (Sec. 1.6.3), leads to a more decent comparison in terms of time-averaged quantities, even if it may fail to correctly identify the peaks in the instantaneous images. As an alternative, the two approaches could be coupled to further improve the physical consistency of such comparison, but this was not attempted in this thesis.

3.5 I-LES results

Due to the large computational effort required, only one simulation was carried out in this work. To select the spark location, the experimental ignition probability map (Fig. 3.28) was exploited as in [49].
The swirling flow and the equivalence ratio distribution are the two main parameters that influence the ignition probability map. As already observed in Sec. 3.3.3, the ignition is really hard in the IRZ due to the very low equivalence ratio. Similarly, ignition is rarely accomplished starting from the SJZ, since the kernel is transported far from the flame region and rapidly quenched. Instead, the ignition probability increases moving towards the combustors walls and the ORZ. In this work, the point located at $r = 40$ mm and $z = 30$ mm was chosen, since it presents a very large ignition probability ($P_{ign} \sim 80\%$). Therefore, the most probable outcome of the ignition simulation is the successful establishment of the flame, rather than a failed spark attempt. Moreover, the good agreement shown in the non-reactive flow field (NR-LES) should guarantee that the ignition process will follow the same path observed in the experiments, provided that the combustion is modelled properly.

3.5.1 Overview of the ignition sequence

In Fig. 3.29 and Fig. 3.30 the simulated ignition process is displayed from the initial energy deposition ($t = 0.0$ ms) up to the final stabilization of the flame ($t = 28.5$ ms). To this aim, instantaneous iso-surfaces of heat release are reported colored by local temperature.

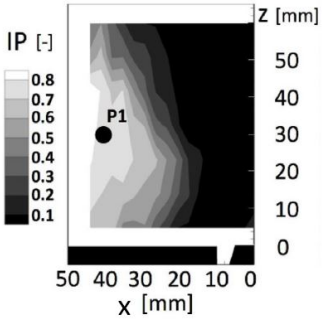

Figure 3.28: Experimental ignition probability map [49].

At the beginning, the kernel has a spherical shape around the spark position. It should be reminded that the source term added in the energy equation has a Gaussian shape in space and time, but it is not visible here because a single iso-surface is drawn. Although simulated, the actual spark discharge and combustion initiation is not described in detail at this stage. In fact, the reaction mechanism employed is not suitable to mimic the complex plasma generation process that takes place after an actual spark discharge.
Within the first 4.0 ms, the kernel/flame grows and starts to be wrinkled by turbulence, losing the initial spherical shape. These initial stages are crucial for ignition success since the heat dissipation may undermine its expansion.
After 6.0 ms the flame is sufficiently large to survive closer to the SJZ, where a large presence of droplets may hinders its development. In fact, while the ORZ presents favorable conditions for flame development, the successful ignition requires the combustion to take place also in the proximity of the SJZ where the flame actually stabilizes.
From $t = 8.0$ ms to $t = 14.0$ ms, the flame propagation follows the same trend discussed above: it continues to expand close to the wall in a clockwise direction (see top view in Fig. 3.30) following the tangential velocity imposed by the swirling flow. Moreover, the inner surface of the flame attaches to the SJZ, promoting the vaporization of droplets, which in turn further helps the flame propagation.
At $t = 16.0$ ms, the flame front touches the bottom of the combustion chamber, whereas at $t = 20$ ms it reaches the opposite wall. At this point,

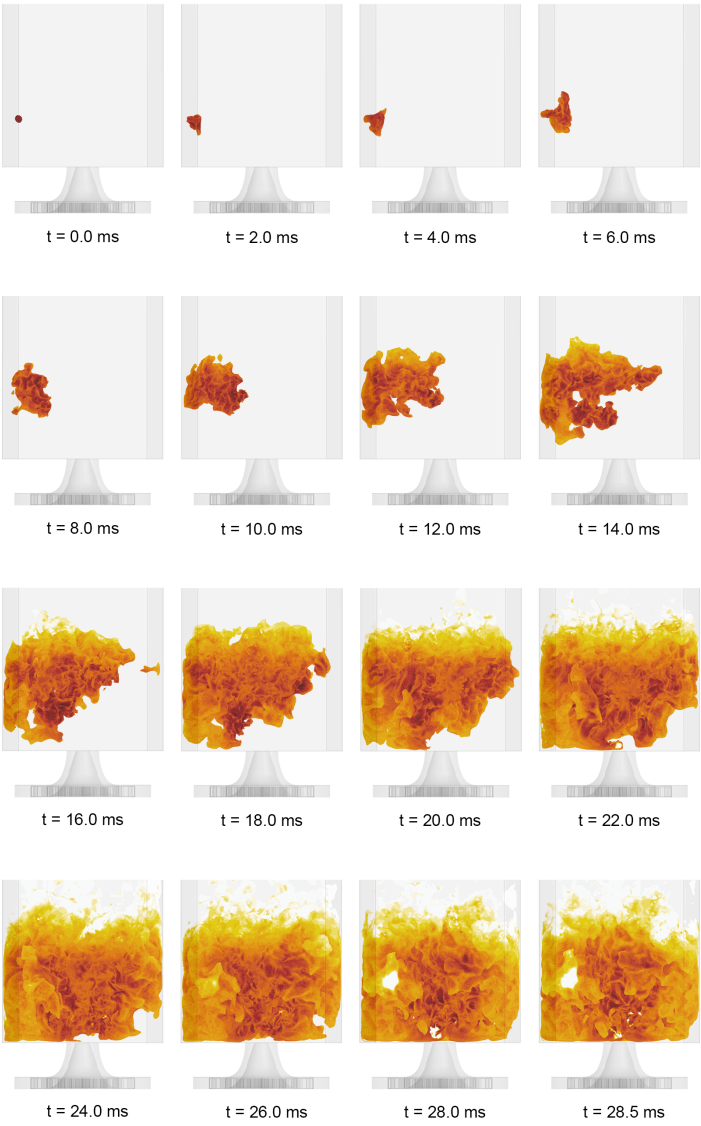

Figure 3.29: Ignition sequence: the flame front is visualized using an iso-surface of heat release at 1.0^8 *J/(m*^{3}*s) colored by temperature (lateral view).*

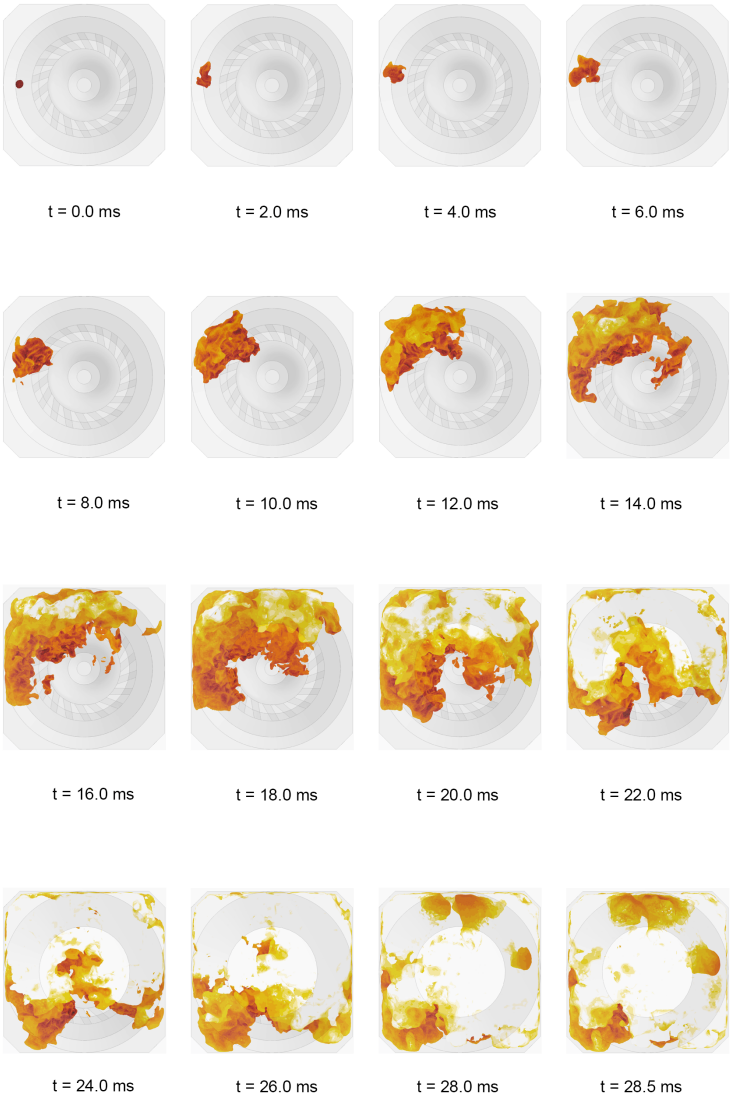

Figure 3.30: Ignition sequence: the flame front is visualized using an iso-surface of heat release at 10^8 $J/(m^3 s)$ *colored by temperature (top view).*

flame extinction is very unlikely because a very large part of the combustor is already ignited. Moreover, the flame is successfully penetrated inside the IRZ which ensures an even faster evaporation of the spray.
Later in the sequence up to 28.5 ms, the chamber is fully ignited. All the walls are reached mostly following the swirling motion in a clockwise direction, but also moving upstream in anti-clockwise direction thanks to the higher temperature and equivalence ratio (due to larger evaporation) which enhance flame speed propagation.

3.5.2 Comparison with experimental ignition sequence

Now that the predicted ignition sequence was described, a qualitative comparison against experimental data can be attempted. Fig. 3.31 (top) shows the experimental high-speed images of the flame kernel development extracted from [18] whereas the at the bottom the numerical sequence is illustrated. Clearly, the same ignition location was used in both cases.

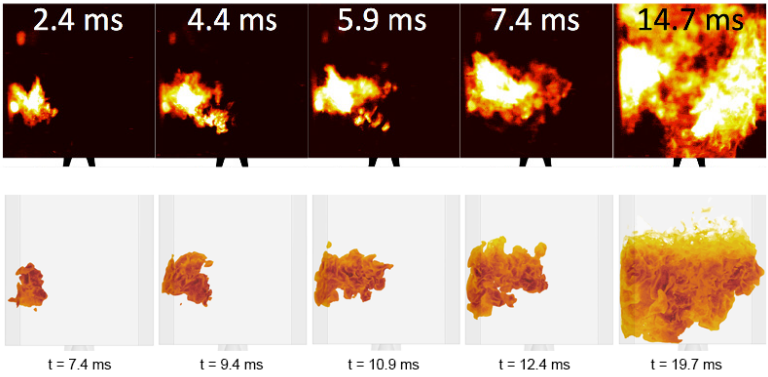

Figure 3.31: (Top): Experimental spontaneous flame emission sequence extracted from [18]. (Bottom): iso-surface of heat release at 10^8 *J/(m*^{3}*s) colored by temperature during ignition sequence. Dimension of visualization boxes are 98 mm* $\times$ *98 mm.*

A delay of 5 ms was added to the numerical data, to allow a better comparison by trying to match the initial shape and dimension of the flame in the first image available from experiments. The kernel incubation strongly depends on the local turbulence, which may slow down the flame growth due to the thermal dissipation. In fact, the local turbulent timescale

is likely in the order of ms (for instance, considering the outer swirler diameter of 20 mm and the maximum RMS of axial velocity of 20 m/s, one gets 1.0 ms). However, also the local equivalence ratio and the amount of spray close to the ignition point are quite relevant in this stage. These two quantities are related to even longer timescales such as the one of the recirculation inside the ORZ and of the swirling flow instabilities. A statistical analysis would be required to shed some light on this point, as it is likely that a numerical spark slightly delayed or anticipated, could have reduced or increased such initial discrepancy.
Once that such delay is added, all the successive steps seem to be well reproduced by the LES, at least in the lateral view here displayed. In fact, the time interval between kernel growth and distortions are correctly catch by the simulation, especially if a certain random variation is accounted due to the turbulent flow.
In [5, 15] a classification of the main mechanism of ignition failure/success is attempted, based on many experimental observations (Fig. 3.32). The upper row displays the five ignition scenarios, whereas the bottom on one is dedicated to the failure modes. Both successful and failure paths are specific of the considered rig.
Plain blue arrows indicate the initial kernel displacement until a considerable volume is ignited. In the successful cases, dashed green arrows describe how developed kernel approaches the injector to complete the ignition of the single-injector.

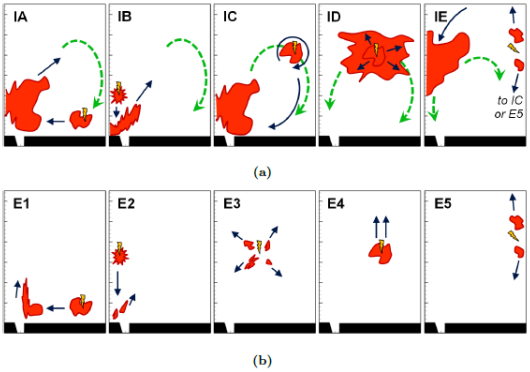

Figure 3.32: Sketch of different observed (a) ignition and (b) extinction scenarios (adapted from [15]).

It is out of the scope of this review to mention all the ignition and ex-

tinction mechanisms shown in [5, 15], even if it is worth discussing briefly the ignition mechanism labelled as *IC* in Fig. 3.32. In [5] this ignition mechanism is referred as *long-ORZ-growth ignition mode* and it is very common since it takes place in the majority of the burner (blue circles on RHS of Fig. 3.33. Usually the smooth and slightly deformed kernel starts

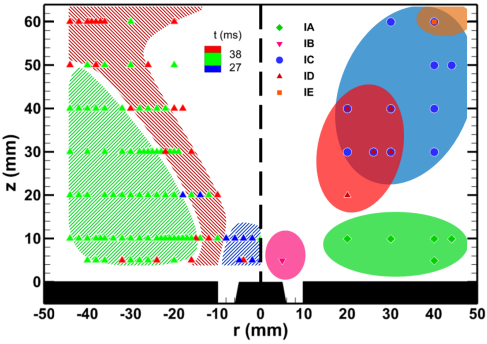

Figure 3.33: Left: mean ignition delay time. Right: Regions of the chamber attributed to the different ignition mechanisms (adapted from [5]).

rotating and it is captured by the flow motion inside the ORZ. Then, the flame evolves quiescently traversing the entire ORZ close to the wall and encountering the spray from the bottom. Finally, the flame is then lifted by the air jet to complete the injector ignition (green dashed arrows). This main characteristics of this path are quite similar to the ones described in the previous section (Fig. 3.29 and Fig. 3.30), further validating the predicted ignition process.

3.5.3 Flame kernel growth and convection

In the previous sections the mechanisms that lead to flame stabilization were highlighted. In this section, the focus is devoted to describe more accurately two instantaneous snapshots, particularly relevant in the flame development. The maximum temperature in the domain, after reaching a peak above 3000 K due to the external energy supplied by the spark, starts decreasing because of the lean conditions where the spark is deposited. After a few ms (oscillations are probably due to turbulent interactions), the maximum temperature starts to increase again and stabilizes around a constant value of 2500 K. In fact, at 6 ms the flame reaches the SJZ.

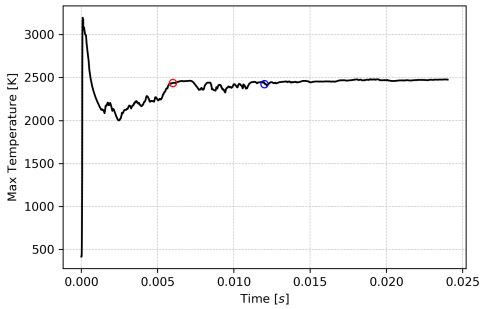

(a)

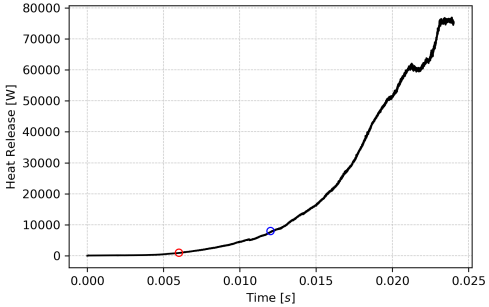

(b)

Figure 3.34: Temporal evolution of the maximum temperature inside the domain (a) and the integral of the heat release (b). The red and blue circles identify the time step at 6 ms and 12 ms respectively.

Although the presence of liquid spray may locally quench it, in other parts it is likely to meet an equivalence ratio close to stoichiometric, which provides such local high temperature. Moreover, at the same time step the integral of the heat of reaction starts to grow faster, probably implying that the flame has reached a critical size that allows it to further expand in the chamber. The same time step is considered in Fig. 3.35(a),

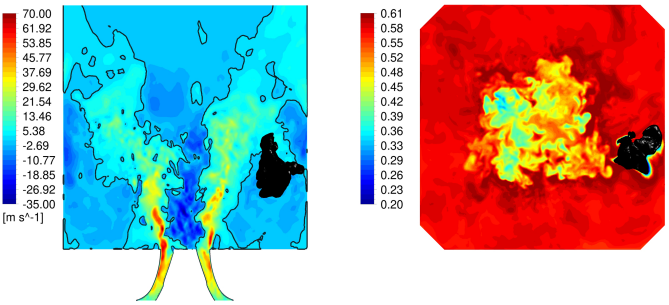

(a) (b)

Figure 3.35: (a) Contour of the instantaneous axial velocity on a longitudinal section with an iso-line $u_{axial} = 0$ m/s and an iso-surface of the heat release (10^8 J/(m^3s)) colored by black at $t = 6$ ms. (b) Instantaneous total equivalence ratio on a cross section with the same iso-surface of heat release (10^8 J/(m^3s)) colored by black $t = 6$ ms.

where the instantaneous axial velocity field is reported with the flame kernel drawn in black. The figure shows the kernel reaching the SJZ, after the initial development inside the ORZ. The left part of the kernel (Fig. 3.35(a)) is likely the one with higher temperature due to the larger equivalence ratio. Fig. 3.35(b) reports the local equivalence ratio field view from top: again the IRZ is leaner than the ORZ. Moreover, there are several spots between these two regions with an equivalence ratio larger than the nominal one $\phi_{global} = 0.61$.
In Fig. 3.34 another important step of the kernel development is pointed out with a blue circle. At 12 ms the flame front covers roughly a quarter of the ORZ and touches the spray from below. Moreover, it can be observed that part of it reaches the IRZ and starts to be convected downstream. Fig. 3.36 reports the same iso-surface of heat release colored with the

tangential and axial velocity. The tangential velocity shows how the kernel evolution follows the swirling flow and it mostly propagates in the clockwise direction. As can be observed in Fig. 3.34, at $t = 12$ ms (blue dot) the maximum temperature in the domain is now constant, whereas the integral of heat of reaction further increase due to growth of the flame which reaches more and more locations in the domain.

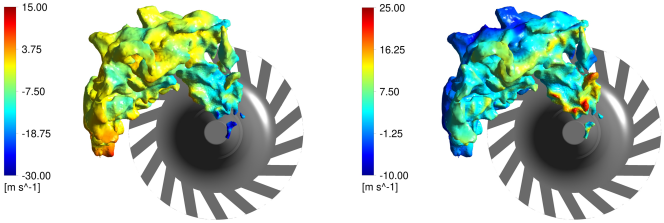

(a) Tangential velocity (b) Axial velocity

Figure 3.36: Top view of flame kernel visualization (heat release iso-surface at 10^8 $J/(m^3 s)$) at $t = 12$ ms colored by: (a) tangential velocity and (b) axial velocity.

3.6 I-PROB results

In this section, the SPHINTIR model developed in [20] and implemented in ANSYS Fluent is employed to compute the ignition probability of the KIAI-CORIA burner. The validation of the non-reactive flow field (*base* simulation hereafter) was carried out in Sec. 3.3 showing that a very good agreement with the experimental data. Therefore, here only the performances of the model mentioned above are evaluated, due to the high quality data used to feed it. At first the ignition probability map is discussed and compared to the experimental data. Then, a sensitivity analysis is carried out to highlight the effect of the several tuning parameters, which constitute the main drawback of the model. Finally, a comparison in terms of flame propagation is attempted using the I-LES data.

3.6.1 Ignition probability map

In Fig. 3.37 a comparison between the ignition probability map measured experimentally and computed numerically is shown. The agreement can be considered quite satisfactory since similar trends can be identified in both the experimental and the numerical map. In fact, a larger ignition probability is recovered in the ORZ, where ignition is favoured by the slightly richer conditions and low velocity. Conversely, ignition is almost impossible in the IRZ and in a large part of the SJZ. Here, compared to

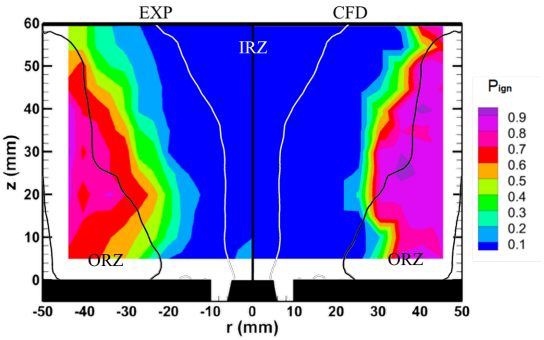

Figure 3.37: Ignition probability map comparison between experiments (left) and CFD (right) using baseline setup.

the esperiments the ignition model strongly underestimates P_{ign}. This is probably due to the time averaging of the base flow field. The large u'_p in this region in conjunction with a low equivalence ratio results in a Ka that exceeds the particle extinction threshold Ka_{crit}. In reality pockets of rich mixture intermittently occur which would lead to some successful ignition events. Fig. 3.38 shows some typical snapshots from the NR-LES where such a rich pockets are seen. There is also a small region with $P_{ign} \neq 0$ right above the injector in the experimental measurements that is not recovered by the model. This is probably due to a poor prediction of the local equivalence ratio in the *base* simulation, where the distribution and evaporation of the really dense spray are not properly simulated by the Lagrangian approach. Finally, higher P_{ign} is predicted in the ORZ: despite the absolute value of ignition probability being slightly overestimated by the numerical model, the global shape of the zone is correctly identified, representing sufficient information to

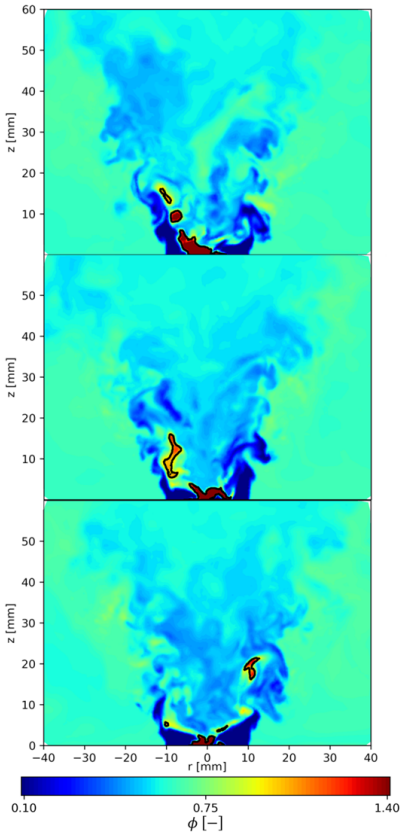

Figure 3.38: Instantaneous independent snapshots of equivalence ratio with black iso-line at $\phi = 1$.

potentially improve the design of the combustion chamber. Based on the author experience, the results shown in Fig. 3.37 already make a useful contribution in the design process.
In this computation, a critical Karlovitz number $Ka_{crit} = 1.5$ was assumed, with an initial spark radius $r_{sp} = 2.0$ mm and a critical ignition progress factor $\pi_{ign,crit} = 0.4$. The employed mesh is composed by hexahedral elements characterized by a size $dx = 2.0$ mm. The choice of these parameters is the result of a sensitivity which is discussed next.

3.6.2 Sensitivity to main tuning parameters

In order to obtain the numerical ignition probability map shown in Fig. 3.37, a sensitivity to the main tuning parameters was performed. For the sake of clarity, the *baseline* configuration is the one presented above ($\pi_{ign,crit} = 0.4$, $Ka_{crit} = 1.5$, $r_{sp} = 2.0$ mm, $dx = 2.0$ mm) and the sensitivity was carried out modifying one parameter at the time, as reported in Tab. 3.5.

Param.	Investigated values	Other parameters
Ka_{crit}	0.5, 1.0, **1.5**, 2.0	$\pi_{ign,crit} = 0.25$, $r_{sp} = 2.0$ mm, $dx = 2.0$ mm
$\pi_{ign,crit}$	0.25, **0.40**, 0.55, 0.70	$Ka_{crit} = 1.5$, $r_{sp} = 2.0$ mm, $dx = 2.0$ mm
r_{sp}	**2.0**, 4.0	$\pi_{ign,crit} = 0.4$, $Ka_{crit} = 1.5$, $dx = 2.0$ mm
dx	1.35, **2.0**	$\pi_{ign,crit} = 0.4$, $Ka_{crit} = 1.5$, $r_{sp} = 2$ mm

Table 3.5: Investigated parameters (in bold the one chosen as baseline).

3.6.2.1 Critical Karlovitz number

Following Neophytou et al. [20] $Ka_{crit} = 1.5$ must be chosen for perfectly premixed flames, whereas an exact value cannot be identified for partially premixed flames. Still in [20] and [55], $Ka_{crit} = 1.5$ is also used successfully for non-premixed flames fueled with n-heptane and methane, whereas in [57] and [54] higher values (i.e., 3.0 and 7.0) are used. In this study a strong influence of the value chosen for Ka_{crit} can be seen from Fig. 3.39.

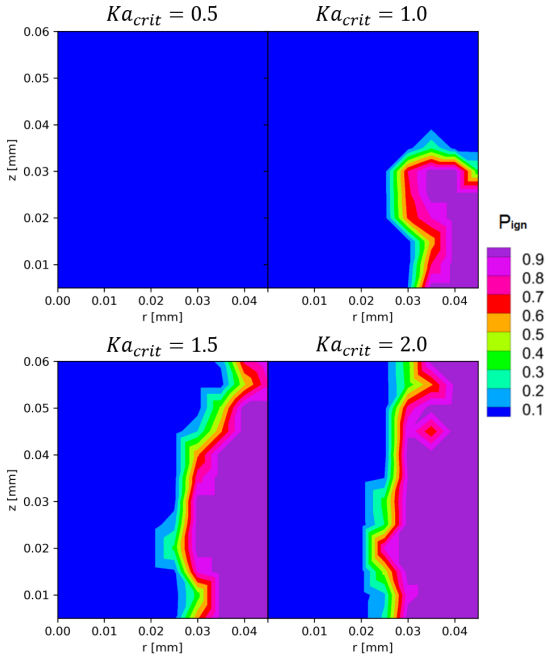

Figure 3.39: Sensitivity to Ka_{crit}.

In the sensitivity illustrated in Fig. 3.39, an initial value of 1.5 was tested, verifying that it can properly represent the area with higher ignition probability (note that $\pi_{ign,crit} = 0.25$ was used to draw these figures). The use of $Ka_{crit} = 2.0$ does not particularly affect the final result, but the previous value is preferred as the global shape of the area with high ignition probability seems better predicted. Lower values of Ka_{crit} do not allow flame particle propagation: the region with non-negligible ignition probability is reduced to a small portion of the ORZ with $Ka_{crit} = 1.0$, while no successful ignition events are registered using $Ka_{crit} = 0.5$.

3.6.2.2 Critical ignition progress factor

$\pi_{ign,crit}$ is strongly case dependent and aims at representing the experimental evidence that once a significant part of the combustor is ignited, the ignition event will be successful [20]. Therefore, it is dependent on the volume of the established flame as well as the domain included in the simulation.
From Fig. 3.40 a certain effect of the chosen value of $\pi_{ign,crit}$ can be pointed out. In Fig. 3.41 the predicted temporal evolution of π_{ign} for $r = 35.0$ mm and $z = 15.0$ mm is shown: while some sparks fail immediately after the deposition, leading to $\pi_{ign} \sim 0.0$, in some of the remaining events a lower propagation speed can be pointed out, that eventually leads to a lower final π_{ign} (below 0.40, marked in red). Such value of π_{ign} is not believed to be enough to completely ignite the combustion chamber, therefore $\pi_{ign,crit} = 0.25$ should not be considered in this case. On the contrary, it can be pointed out that $\pi_{ign,crit} = 0.40$ successfully selects ignition events that could eventually lead to ignite the most of the domain (marked in yellow and green in Fig. 3.41). The same conclusion can also be drawn for $\pi_{ign,crit} = 0.55$, which provides similar results to $\pi_{ign,crit} = 0.40$ (see Fig. 3.40). Instead, if $\pi_{ign,crit} = 0.70$ is considered, a globally lower ignition probability is predicted: from Fig. 3.41 it can be seen that the simulation time of 60 ms affects this prediction, considering successful only the ignition events marked in green and potentially excluding some successful ignition events with a lower propagation speed (marked in yellow). In this case, the output of the simulation is dependent on the simulated time, which potentially constitutes another tuning parameter. Therefore, $\pi_{ign,crit} = 0.40$ was chosen for the baseline setup which should produce the same ignition probability map even if a longer simulation time was considered.

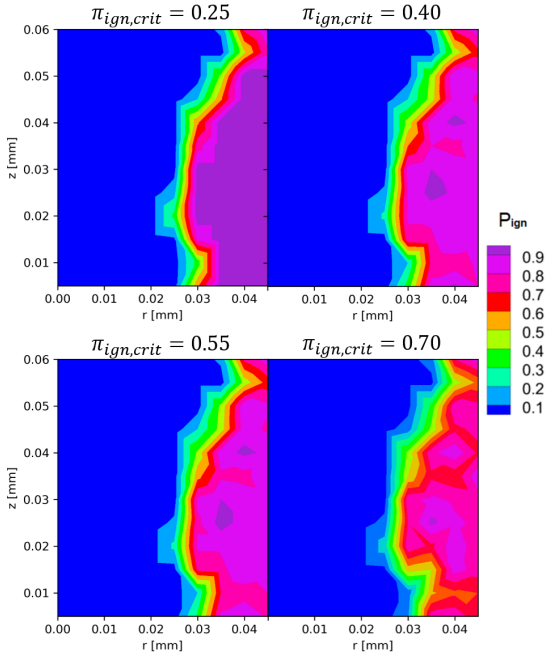

Figure 3.40: Sensitivity to $\pi_{ign,crit}$.

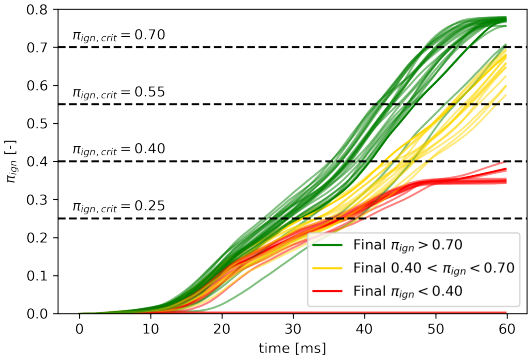

Figure 3.41: Temporal evolution of π_{ign} for $r = 35.0$ mm and $z = 15.0$ mm, analysis of different $\pi_{ign,crit}$.

3.6.2.3 Mesh size

The role of the grid spacing in the SPHINTIR grid was extensively discussed in [20], where also some requirements on Δ and dt were introduced. The aim of this section is only to demonstrate the another drawback of the present model: while in CFD a finer grid is usually associated with a more accurate result, this is not the case with the approach under investigation. In Fig. 3.42 a comparison is shown between two different mesh size, showing that better results can be obtained with a coarser mesh. This should not be considered a mistake, but a consequence of the random initialization and tracking of the flame particles. As discussed in [20], by adopting the same initial spark size (r_{sp}) a larger number of *flame particles* is injected, creating more flame particles per unit of volume, i.e., a larger *flame particles density*. Therefore, the higher the number of particles in the combustor, the higher the number of particles capable of successfully propagate the flame. As shown in Fig. 3.43, a reduced mesh size leads to many similar ignition events, each one characterized by a similar development in time. On the contrary, a larger grid spacing provides a more random development of the initial kernel.

3.6.2.4 Spark radius

Experimentally, a nominal spark size of approximately $1.0 - 2.0$ mm is reported by [49]. However, since in the present model the aspects related

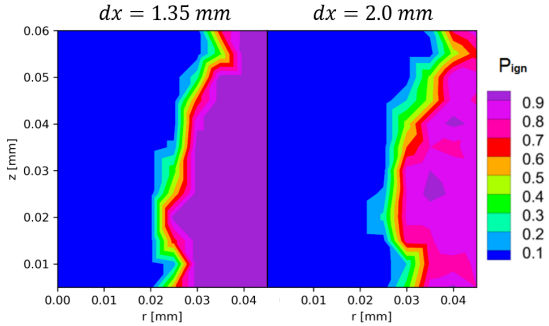

Figure 3.42: Sensitivity to dx.

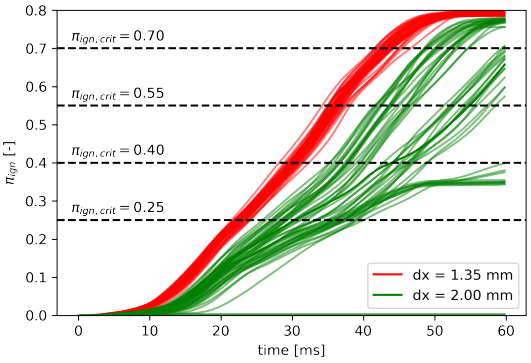

Figure 3.43: Temporal evolution of π_{ign} for $r = 35.0$ mm and $z = 15.0$ mm, analysis of different dx.

to initial kernel development are overlooked, the size and the shape of the spark represent two parameters that have to be set by the user. Considering that a laser-induced spark was employed in the experiments [70], only a spherical shape was considered in the course of this work. In Fig. 3.44 two sizes are compared. Only small differences can be seen in

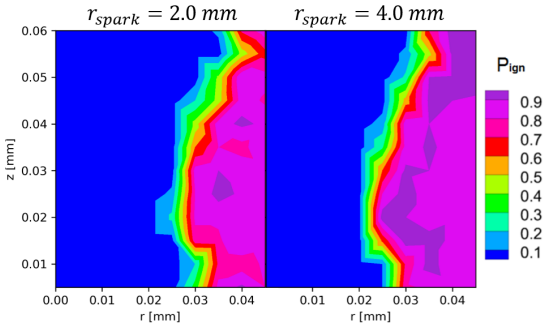

Figure 3.44: Sensitivity to r_{sp}.

the contours, but a globally higher ignition probability can be noticed for the case with a larger spark radius. This is clearly due to a larger number of particles initialized for each location, creating a better chance to survive and finally ignite all the combustion chamber.
To overcome this issue as well as the one related to grid size, an energy criterion could be proposed, in order to distribute the same amount of energy deposited by the spark over a larger number of flame particles. To the best of the author knowledge, this approach was not attempted so far.

3.7 Comparison between I-LES and I-PROB results

In Fig. 3.45 the evolution of the flame front predicted by the I-LES and I-PROB approaches is reported. The baseline setup is considered for the SPHINTIR model and the spark position selected is the one used for the I-LES simulation. It should be pointed out that several realization were available from the ignition probability model and only one was selected here to compare the outcome of the two simulations. As already done in the paragraphs above, for I-LES an iso-surface of heat-release is used, coloured by temperature (left). The heat release is not available in SPHINTIR and the ignited region is displayed with a volume render of

the cells marked as burnt (the colour is not relevant in this case).
A similar flame behaviour is predicted by the two approaches, in particular regarding the propagation in clockwise direction following the swirling motion. In all the considered time steps, the volume occupied by the flame is similar as well as the area newly ignited from the previous instant. Clearly, some effects are lost in the SPHINTIR approach, like the wall-quenching at 10.0 and 15.0 ms. Similarly, the anti-clockwise propagation of the flame (visible since 15.0 ms), due to the mass and heat diffusion rather than kernel convection, is not captured.
Anyway, this final comparison suggests that the SPHINTIR approach can be used to estimate the also the flame trajectory with sufficient accuracy. Moreover, it allows to estimate the time required to complete the ignition and reach certain parts of the combustor. Finally, such comparison further proves the importance of the transport of the kernel due to the underlying velocity flow field, rather than flame propagation itself.

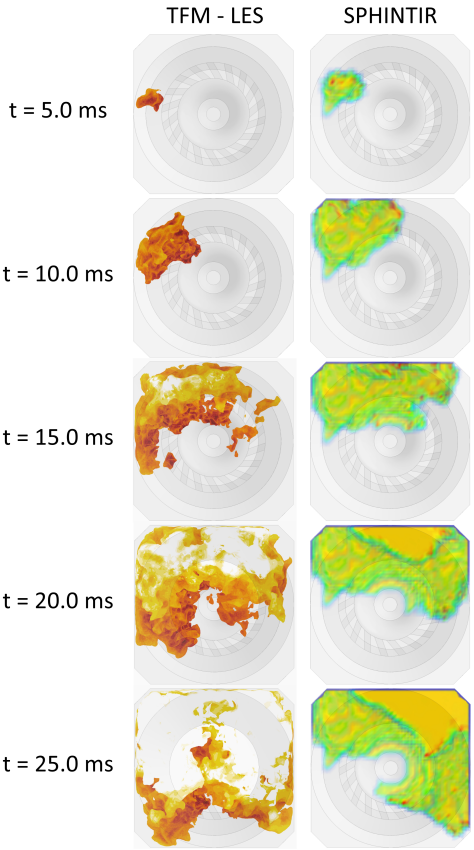

Figure 3.45: Comparison of flame propagation between I-LES (left) and I-PROB (right) simulations.

3.8 Conclusions to Chapter 3

In this chapter the KIAI-CORIA rig was simulated using the modelling approaches presented in Ch. 1 and 2. At first, the investigated test rig was described with a particular focus on the experimental techniques used and the data available to validate the CFD simulations. Later, the only numerical work available on such test case was briefly revised.
A section is then dedicated to present the numerical setup employed for the simulations, concerning both the set of LES and the low-order model SPHINTIR. Finally, the obtained results were described in detail, providing an extensive validation of each simulation that was carried out.
After this chapter, it can be concluded that the techniques employed to characterize the ignition process performed sufficiently well on the considered test case, providing a quite accurate results in terms of flame propagation, ignition sequence and ignition probability. All of these input might be useful in an industrial design process, to improve the ignition performances of the burner.
The main simplifications of the considered rig must also be considered. With respect to a potential study of an actual combustor, favourable conditions were considered in terms of temperature and pressure. Moreover, the BCs for the spray tracking were quite easily deduced from previous works that followed the experimental data. In the next chapter, a rather different test case is considered, from which the need of an accurate model to predict the spray size distribution after primary breakup is justified.

Chapter 4

The importance of spray under altitude relight conditions

The aim of this chapter is to help the reader understand the shift of focus towards the primary breakup that will be carried out in the last chapter of this manuscript. The set of approaches described in Ch. 1 and Ch. 2 are valuable tools to simulate the ignition process under atmospheric conditions, which may strongly differ from the ones of technical relevance. In fact, as already pointed out in the introduction, the main reason of understanding ignition is related to the improvement of the altitude relight performances. It means that far lower pressure and temperature should be considered, slightly changing the relevance of the several factors affecting the ignition process.
The amount of numerical and experimental studies on this topic is small: to the best of the author knowledge, the experimental studies of altitude relight are limited to [6, 88, 89], whereas it as been faced numerically only in [90] using reactive LES and in in [57] with SPHINTIR. As correctly pointed out in [90], almost no evaporation takes place and droplets are free to travel everywhere in the combustion chamber. Therefore, most of the liquid reaches the confinement of the burner and may form a liquid film over the spark plug, strongly influencing the outcome of the energy deposition process. The trajectory of droplets can still be studied effectively with the Lagrangian approach presented in Ch. 1, although some issues may rise from their initialization. A practical example is provided at this point: a test case experimentally studied at KIT, capable of reproducing altitude relight conditions is introduced. Compared to the previous chapter, such test case is more interesting from a technical perspective, although the limited optical accessibility and the lower amount of measurements

available led towards the use of the KIAI-CORIA rig for the previous assessments. In this case, two *Stress-Blended Eddy Simulations* (SBES) were carried out, but a throughout validation was not possible as in Ch. 3. Despite that, some results in terms of spray distribution are shown, highlighting the disruptive effect of the spray initial conditions under altitude relight conditions. In this case, a numerical misprediction of the trajectory of the droplets may fundamentally alter the predicted ignition performances. To avoid this kind of issues, a deeper knowledge of how dispersed spray is formed under altitude relight conditions is required, as well as a numerical approach to estimate the initial conditions of the spray.
Motivated by that, the primary breakup process is briefly described in the next of this chapter. The main aim is to provide the reader with the necessary understanding of the physics of the primary breakup to fully comprehend its relevance under altitude relight conditions.
Finally, to further support the present analysis, a recent and extremely relevant experimental publication is reviewed, aiming at illustrating the difficulties of spray breakup when altitude relight conditions are considered.

4.1 The initialization of spray in altitude relight simulations

In this section, a very brief description of one of the activities carried out within the *Soot Processes and Radiation in Aeronautical innovative combustors* (SOPRANO) project is provided, aiming at showing the importance of the liquid injection under altitude relight conditions. In fact, two different strategies for liquid injection were compared, underlying a very different distribution of liquid close to the spark location.
Several details about the experimental apparatus and the setup of the simulation were omitted for the sake of brevity. Moreover, the operating conditions and the simulations results were normalized, since some parts of the hardware were provided by *Avio Aero - A GE aviation business*, that requires the maximum confidentiality in sharing the data. For the same reason, many geometrical features were blanked.
Despite these limitations, the purpose of the discussion still holds: under altitude relight conditions, the low evaporation rate requires a very accurate estimation of the initial conditions of the spray, if a correct distribution of liquid fuel must be retrieved.
Although many ignition measurements were already available during the writing of this thesis, it was decided not to attempt the simulation of

this rig with the approaches presented in the first part of the thesis. As it will be shown later, this was due to strong uncertainties in liquid fuel injection that were cleared only recently.

4.1.1 ISCAR rig description

A detailed description of the *Ignition in Sub atmospheric Conditions-Altitude Relight* (ISCAR) rig configuration and available measurements can be found in [91, 92, 93, 94, 95]. It is worth specifying that such rig was built during a previous project, but it was updated and reused during SOPRANO for a new set of measurements. Hereby, only the main features of the rig are discussed for the sake of clarity. A sketch of the rig is reported in Fig. 4.1.

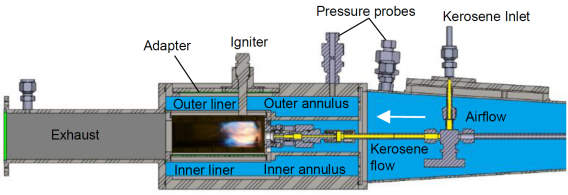

Figure 4.1: Sketch of the ISCAR rig (adapted from [95]).

The rig is capable of reproducing altitude relight conditions, both in terms of pressure (up to 0.4 bar) and temperature (about -20°C). In the studied configuration, it is equipped with an air swirler, a fuel injector and a spark plug provided by *Avio Aero - A GE aviation business*, in order to increase the technical relevance within the aforementioned European project. Except from these parts, the rig consists of a box-shaped combustion chamber with dilution holes to mimic a RQL combustor.
The optical access is granted by a quartz window placed on one side. The fuel employed is kerosene and the injection temperature is estimated to be slightly below the one of the room due to the fuel pipes being exposed to the cold air during the experimental trial. In this way, it is possible to replicate the ignition process under more relevant operating conditions if compared to the KIAI-CORIA test case shown in Ch. 3. In this work, the considered pressure is 0.43 bar, whereas the temperature of the injected air is well below -10°C (the exact value can not be disclosed for confidentiality issues).
Additional details about the experimental techniques and the measure-

ments are not reported here for the sake of brevity. Moreover, the experimental data cited will be the subject of a future publication by KIT and will be part of the Ph. D. thesis of Martinos A. D.

4.1.2 Numerical setup and domain

The simulations shown in the next were performed within the framework of the SOPRANO project, along with other activities not presented in this thesis. As already explained in Ch. 3, RANS is not precise when a swirling flows in a combustion chamber is considered. In this case, a wall resolved LES would be unfeasible due to the very large number of elements required to properly reproduce the boundary layer, considering the extension of the rig. Therefore, a hybrid RANS-LES approach named SBES was employed. Such approach was proposed by Frank and Menter [96] as further development of the *Detached Eddy Simulation* model. As other hybrid models, it is based on a dynamic blend between RANS and LES closures for the eddy viscosity:

$$v_t^{SBES} = f_s \cdot v_t^{RANS} + (1 - f_s) \cdot v_t^{LES} \tag{4.1}$$

The shielding function f_s is adopted to prevent the use of LES sub-grid model in the unresolved boundary layers, whereas a RANS approach is preferred. Thus, a lower mesh resolution was needed, allowing to consistently reduce the required computational effort. Concerning the RANS part, a *k-ω Shear Stress Transport* (SST) model was adopted, whereas a WALE sub-grid scale model was employed in the LES portion. No reactive simulations were carried out: therefore, compared to the set of equations shown in Ch. 1, no energy equations were solved here for the gaseous and liquid phase, considering that a very low temperature variation takes place (both the air and the spray are cold). Moreover, the evaporation of liquid particles was not considered: this seems to be in contrast with the scope of the work, considering that the local equivalence ratio is listed as one of the most influencing factor for gas turbine ignition [85]. Even though, some considerations on the operating conditions under investigation should be carried out first. In fact, considering the operating conditions, it is possible to calculate the maximum gaseous equivalence ratio that can be achieved locally. Such maximum equivalence ratio, corresponds to the value under saturation conditions which depends on:

- gas phase temperature,
- pressure,
- liquid fuel composition.

First of all, fuel saturation pressure can be computed for a given temperature: in this case the n-decane Antoine Law from NIST repository [87] was considered. The saturation pressure of the fuel represents the maximum partial pressure of vapor that can be found in the combustor. Therefore, the associated equivalence ratio can be computed as a function of temperature (Fig. 4.2). In this case, a maximum equivalence ratio of

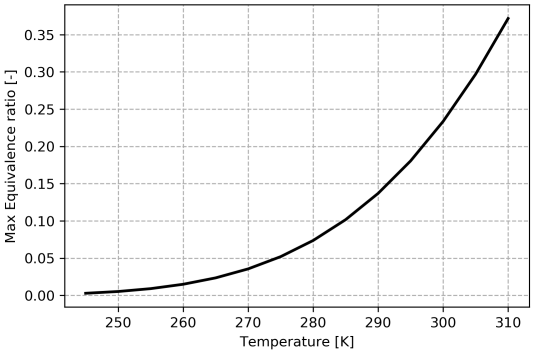

Figure 4.2: Maximum equivalence ratio as a function of temperature under the pressure investigated experimentally. N-decane is considered.

approximately 0.01 is found for a temperature below 260 K, which does not have any effect on the kernel generation.
Thus, the concentration of vapor fuel prior to spark discharge is negligible in the considered case, whereas far more important is the liquid spray distribution close the spark plug [68]. Moreover, from an experimental point of view, several spark attempts are normally required to observe a successful ignition event. These may promote liquid fuel evaporation and recirculation within the IRZ, increasing the ignition probability. Sadly, the simulation of a pair of consecutive spark attempts is not feasible, due to the long interval between the two (from a numerical perspective). Therefore, liquid evaporation was overlooked, which also provides the following advantages in terms of computational effort:

- it is not necessary to solve a separate transport equation for vapor fuel;
- the energy equations for gas phase and particles are not solved (due to the limited temperature range, large variations in thermophysical properties are not expected).

Because of the excessive computational effort, also the liquid film formation was not considered in the simulations. Therefore, the particles were simply removed from the domain once they hit a wall.
Under these assumptions, only continuity and momentum equations were solved along with the equations dedicated to turbulence modelling for the carrier phase. Similarly, only the momentum equation was considered for the dispersed one. This strongly reduces the computational effort, allowing a finer mesh to be used for a better resolution of the turbulent eddies.
That said, a sketch of the numerical domain is reported in Fig. 4.3(a). Prescribed mass flow was specified at all the domain inlets, according to the mass flow split measured experimentally. No velocity perturbations were imposed, as most of the turbulence is generated through the swirler and the dilution holes. Moreover, no velocity fluctuations were used at the inlet for spark coolant. Static pressure was imposed at the outlet while all the walls are set as no-slip (including the liner spark marked in green in Fig. 4.3(a)).

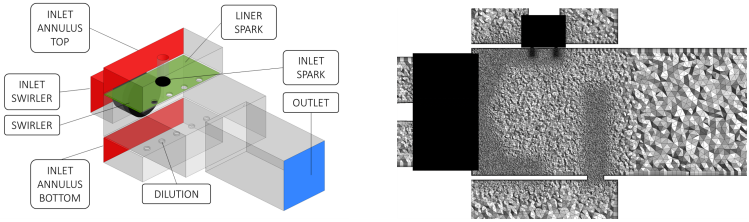

(a) Numerical domain (b) Mesh

Figure 4.3: Numerical domain and mesh used for computation on ISCAR rig.

In this work, the mesh size was determined scaling down the one used in [97]. In fact, the present rig consists in a larger and scaled version of the apparatus experimentally and numerically investigated by the *University of Florence* UNIFI. In [97], thanks to the detailed unsteady PIV measurements carried out on the non-reactive flow field, it was possible to determine that the employed mesh was sufficiently fine to resolve most of the turbulent structures observed experimentally. In fact, a correct match in terms of mean and RMS profile of velocity in the jet was obtained. Therefore, no additional discussion on the flow field resolution and sizing was carried out here. The resulting mesh is reported

in Fig. 4.3(b).

4.1.3 Brief description of the numerical findings

As already mentioned before, two strategies for liquid injection were compared:

- *inj-1*: the droplets were injected following a Rosin-Rammler distribution (as in Ch. 3) with an SMD derived from an experimental correlation [98] and a certain spread parameter based upon internal experience. This approach does not require experimental data and it was used several times in similar works [45];

- *inj-2*: a Rosin-Rammler distribution was retained, but the SMD and the spread parameter q were selected based on precise experimental data, available from KIT (and not yet published). This approach, although not always possible, leads to a more accurate injection of the spray.

The resulting spray size distributions are compared in Fig. 4.4. It can

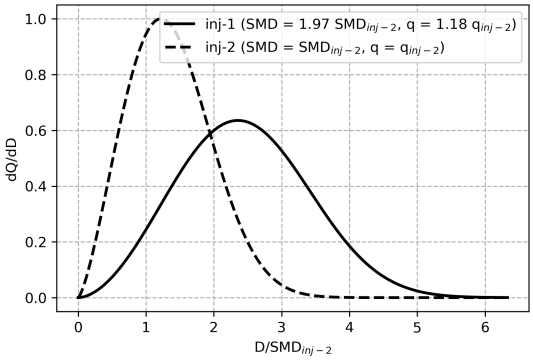

Figure 4.4: Comparison between the two first injection employed and the revised one thanks to experimental data: probability density function.

be observed that a larger amount of small droplets are injected in *inj-2*, whereas the distribution of *inj-1* is wider and shifted towards larger diameters. Therefore, the particles injected through *inj-2* are more likely to follow the gaseous flow field.
In Fig. 4.5 the mass flow rate of the droplets reaching the liner equipped

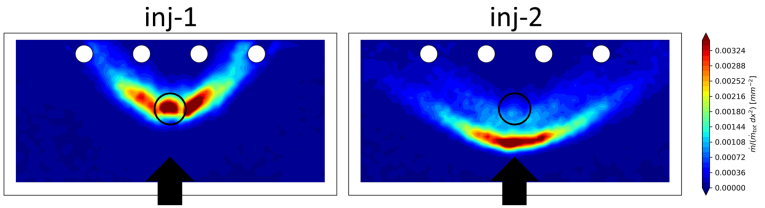

Figure 4.5: Comparison between the two first injection employed and the revised one thanks to experimental data: mass distribution.

with the spark (marked in green in Fig. 4.3(a)) is reported. The black arrow indicates the position of the swirler, whereas the small circle the one of the spark. A very different distribution can be pointed out between the two injection strategies: in *inj-1*, most of the liquid hits the wall very close to the spark, whereas in *inj-2* it follows more closely the trajectory of the swirling jet. From an ignition perspective, this difference may strongly alter the thickness of the liquid film which is formed over the considered liner, with a huge impact on the spark discharge. However, it is worth pointing out again that film formation was not strictly investigated here and the mass distribution is only referred to the droplets that reached the wall before being removed.
In Fig. 4.6 the same comparison is carried out in terms of SMD, showing the large difference between the two cases considered. In fact, the larger droplets of *inj-1* may have a very different behaviour in terms of rebounding or sticking to the surface.

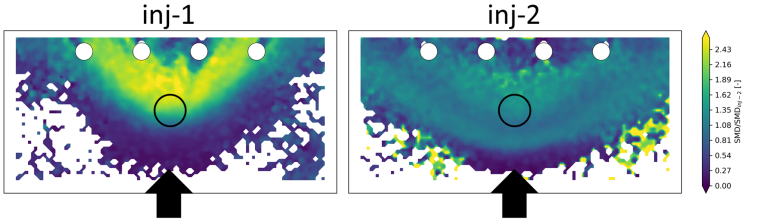

Figure 4.6: Comparison between the two first injection employed and the revised one thanks to experimental data: SMD distribution.

The outcome of this introduction is now clear: if no experimental data

were available, *inj-1* would have been used, probably leading to a very poor representation of the liquid distribution in the chamber and close to the wall.
That said, the approaches presented in Ch. 1 and Ch. 2 were not tested on this rig. Instead, the focus is now shifted on a tentative approach to prevent the use of experimental correlations and best practices to set up the initial conditions of the spray. Prior to that, a brief description of primary breakup is provided in the next section.

4.2 Characteristics of sprays and atomization

The atomization is the fundamental process that leads to the production of a spray (a population of droplets) starting from a coherent structure of liquid. Lefebvre [85] defined the atomization as "*the process in which a liquid jet or sheet is disintegrated by the kinetic energy of the liquid itself or by the interaction with the high velocity gas stream*". Before focusing on the description of the atomization process, it is worth introducing the characteristic numbers employed for the description of the sprays.
One of the most relevant quantity within this context is the liquid volume fraction α_l:

$$\alpha_l = \frac{\sum_{k=1}^{N} V_{d,k}}{V} = \frac{V_l}{V} \tag{4.2}$$

where $V_{d,k}$ stands for the volume of the k-th droplet, N for the number of droplets considered and V_l for the generic volume of the liquid. All of these quantities are referred to the control volume V. The so-called Stokes number St_p is defined as:

$$St_p = \frac{\tau_p}{\tau_g} \tag{4.3}$$

where τ_p refers to a characteristic time for the dynamics of a generic particle (in this scenario represented by a droplet of liquid) and τ_g to a characteristic time for the carrier phase in which the particle is transported. For instance if $St_p << 1$ the time-scale of the dispersed phase is much smaller than the one of the carrier phase, and the droplets are practically transported by the gaseous phase.
It is now possible to introduce a first classification between the regimes which guide the phase to phase interaction, as shown in Fig. 4.7. Here, the following regimes may be identified:

- $\alpha_l < 10^{-6}$: the droplets are transported by the continous phase without affecting it (one way coupling).

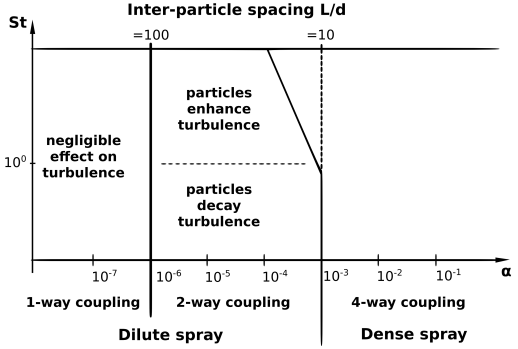

Figure 4.7: Classification of the regimes between the dispersed phase and the carrier one, adapted from [99].

- $10^{-6} < \alpha_l < 10^{-3}$: the mutual effects are now relevant (two way coupling) but α_l is still low and the spray can still be considered as diluted. Therefore the sub-models developed for an isolated droplet (see Ch. 1) can still be used.
- $\alpha_l > 10^{-3}$: the spray is dense and a four way coupling must be considered.

From a modelling point of view, a two-way coupling is normally used when a Lagrangian tracking is adopted as in Ch. 3.
While α_l and St_p are useful numbers to characterize the spray, the breakup process requires the definition of non-dimensional number to distinguish different breakup regimes. The breakup process takes place because the magnitude of the disruptive forces exceeds the one of the consolidating. For instance, the aerodynamic drag promotes a distortion of the droplet, whereas the surface tension tries to stabilize it in a spherical shape. This ratio of disruptive and consolidating forces is described by the dimensionless Weber number We:

$$We = \frac{\rho_g U_{rel}^2 L}{\sigma} \tag{4.4}$$

where L is a characteristic length (e.g., the droplet diameter, the diameter of the liquid jet or the thickness of the prefilmer), U_{rel} is the relative velocity between phases and σ the surface tension.
Another relevant characteristic number is the Reynolds number Re, representing the ratio between the inertial and the viscous forces acting on

the atomizing liquid:

$$Re = \frac{\rho_g |U_{rel}| L}{\mu_g} \tag{4.5}$$

μ_g and ρ_g are the dynamic viscosity and the density of the gas phase. Finally the Ohnesorge number Oh represents the ratio between the viscosity contribution inside the liquid phase and the aerodynamic and surface tension forces:

$$Oh = \frac{\sqrt{We}}{Re} \tag{4.6}$$

The atomization process can be considered as if composed by two consecutive steps: the first one is the *primary breakup*, which indicates the initial disruption of liquid close to the injection point and its fragmentation into smaller entities that will eventually reshape into spherical droplets. The second one is the *secondary breakup*, which involves a further separation of the droplets into smaller ones. A brief description of the first stage is

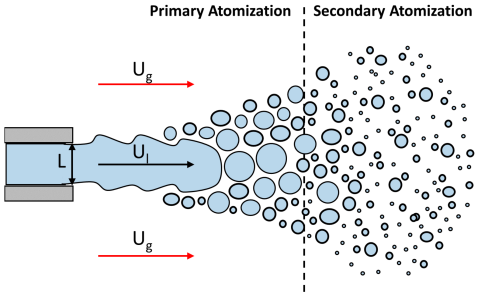

Figure 4.8: Sketch of the two steps of breakup. Adapted from [100].

reported next.

4.2.1 Primary breakup

The primary breakup occurs close to the injector exit and consists in the initial fragmentation of the coherent structures of liquid into smaller entities of any shape. The geometry of the injection system is therefore extremely relevant as it will be observed later. From a general point of view, the primary breakup starts with the unstable growth of deformations on the liquid interface that disrupt the initial shape of the liquid flowing out from the injector. Subsequently, the formations of smaller liquid

fragments takes place, characterized by a variable size, dependent on the initial energy of the liquid flow. However, a general theory is not available to describe the primary breakup and each class of atomizers must be characterized individually. In the following, a brief description of the primary breakup mechanisms for liquid jets and liquid sheets is provided. Anyway, a comprehensive discussion of this topic is beyond the purpose of this section and the interested reader is addressed to the specific literature [85, 101].

4.2.1.1 Liquid jets

Several studies were performed regarding the atomization of round jets. Here, only the classification suggested by Reitz [102] is considered, where different breakup regimes were distinguished. In Fig. 4.9, the liquid core length L_{BU} is reported against the injection velocity U_L. Five breakup mechanisms are identified [101]:

- dripping regime (A): droplets are directly emitted from the nozzle exit and a liquid column is not formed. In this case, the injection velocity is negligible.
- Rayleigh regime (B): the liquid flows out of the injector as a coherent column. A single axisymmetric perturbation appears, with a wavelength similar to the jet diameter. Droplets are detached from the jet when the amplitude of the perturbation becomes equal to the jet radius and their diameter is roughly 1.89 times the one of the jet.
- First wind-induced regime (C): stronger perturbations evolve on the jet interface. Here, the droplets production is not well organized as in the previous case, but it is still axisymmetric and their diameter is still close to the one of the jet.
- Second wind-induced regime (D): the perturbations now grow faster, immediately after the ejection fo the liquid from the orifice. The shape of the column is now chaotic and two primary breakup mechanisms can be observed all along the jet: near the nozzle small droplets are peeled off the interface whereas downstream the remaining liquid flow breaks up into large liquid fragments.
- Prompt atomization regime (E): it is the most relevant in technical applications. It is characterized by a complete liquid disruption that occurs immediately at the nozzle exit. It produces droplets with an average diameter much smaller than the jet one.

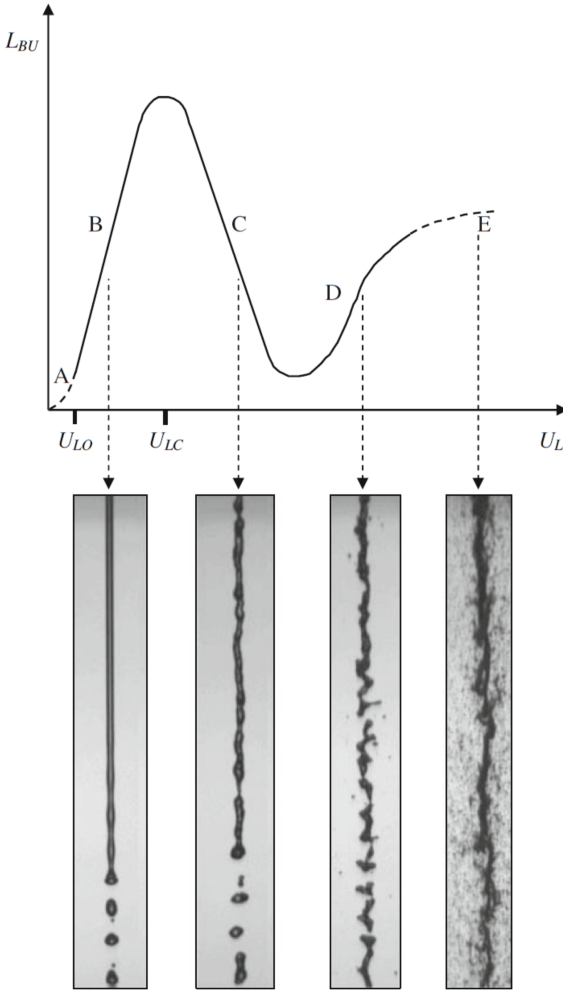

Figure 4.9: Cylindrical jet length as function of injection velocity (top) and examples of visualizations (bottom). Adapted from [102].

This kind of configuration is typical for the injection of fuel in the automotive sector. In the modern aero engine combustors a prefilmer configuration is normally preferred, that presents similarities with the liquid sheet atomization described in the nex section.

4.2.1.2 Liquid sheets

A wide range of injection systems exploit the discharge of liquid in the form of a liquid sheet. This can have a flat shape, a conical one or even annular, depending on the injector geometry. The sheet fragmentation depends on the relative velocity between the phases. As long as there is not an air stream (i.e., $U_g = 0$), the liquid sheet converges down to a point, where it coalesces. If the velocity of the liquid increases, some effects related to the turbulence appear and some perforations in the liquid sheet are generated. However, these phenomena are not accompanied by any drop formation and cannot be labeled as breakup.
By adding an high-speed gas stream, a significant shear stress is generated with the liquid sheet leading to the formation of longitudinal and transverse waves, that quickly grow and end in sheet disintegration. The different regimes that may occur in this configuration can be summarized as:

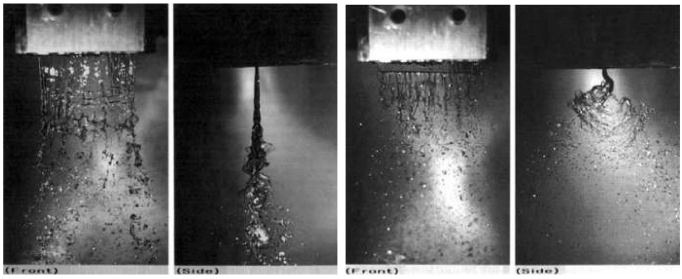

Figure 4.10: Air-assisted flat breakup of a liquid sheet: left, cellular breakup and right, stretched streamwise ligament regime. Adapted from [101].

- cellular breakup regimes (Fig 4.10, left): a low velocity ratio U_g/U_l is present between the two phases and the sheet oscillation results in a mix of sinusoidal and dilational waves with low amplitude. Both spanwise and streamwise ligaments generate liquid cellular structures which finally disintegrate into droplets.

- Stretched streamwise ligament regimes (Fig 4.10, right): now streamwise ligaments predominate over the spanwise ones. The liquid is subject to strong lateral oscillations, which are the cause of a higher spray angle. A shorter breakup length is also recovered.

- Prompt atomization: if the ratio U_g/U_l is high enough, the breakup takes place close to the nozzle tip and the liquid sheet is not even formed.

A more detailed discussion on this topic can be found in [101].
To conclude, the main quantities that play a primary role in primary atomization are:

- the relative velocity between phases;

- the injector geometry;

- the properties of the liquid phase;

- the properties of the gas phase.

As reported in Fig 4.8, primary breakup is usually followed by a second stage of atomization, referred as secondary breakup. This topic is not covered in the present manuscript and the reader interested in a further reading is addressed to specific literature [85, 103].
In the next section, the role of the primary breakup in altitude relight conditions is stressed out by describing the effect of ambient pressure on the atomization process of a prefilmer airblast atomizer.

4.3 The primary breakup under altitude relight conditions

The relevance of the primary breakup in the simulation of turbulent spray flames was already discussed extensively in a recent thesis of our research group [100]. For the sake of brevity, the discussion is here limited to the altitude relight conditions. The work recently published by Chaussonnet et al. [104] sheds a light on the effect of pressure on the atomization process. The experimental test case is a planar prefilming airblast atomizer already experimentally studied at the *Institut für Thermische Strömungsmaschines* (ITS) of the *Karlsruhe Institute of Technology* (KIT) [98, 105, 106, 107].
A sketch of the test section is reported in Fig. 4.11. The geometry consists of a planar wing-shaped prefilmer where the liquid is supplied through a cavity on one side of the prefilmer body. The injection is performed

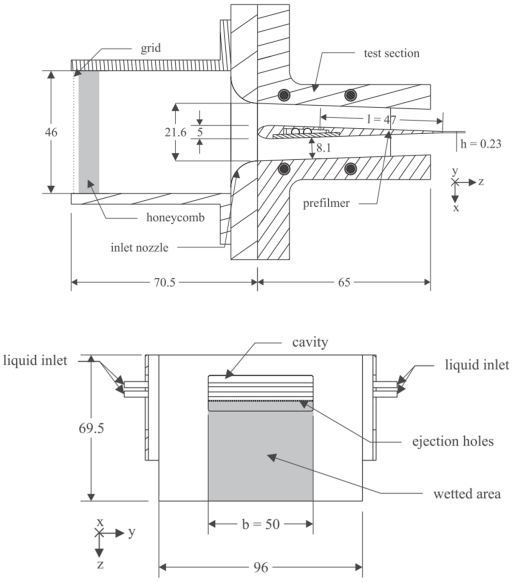

Figure 4.11: Experimental setup of the prefilmer for the KIT atomizer: side view (top) and top view (bottom). Adapted from [107].

using 50 equidistant distributed holes, forming a thin film of liquid that homogeneously wets the surface up to the atomizing edge. Here, the liquid accumulates and creates a reservoir that feeds the atomization process, whereas the air flows around the wing-shaped geometry on both sides. Available measurements include particle and ligament tracking as well as Laser Doppler Anemometry. But, above all, the shadowgraphy technique was used to acquire information about the amount of liquid accumulation at the prefilming edge and collect statistics about the generated droplets and ligaments. A *Depth of Field* (DoF) correction was employed to properly estimate the object sizes.
Such work represent a unique experimental data-set on prefilmer systems with detailed information about the evolution of the atomization process in the near injection region and about the droplet population generated in the downstream zone.
After many works under atmospheric conditions [98, 105, 106, 107], in [104] the prefilmer was installed on a pressurized rig and measurements were carried out up to 7 bar. Clearly, the higher pressure also produces an increase in air density, which in turn increases the We and Re numbers introduced in the previous section. Because of that, a faster atomization is observed (Fig. 4.12). On the left, the operating pressure was set to 3 bar,

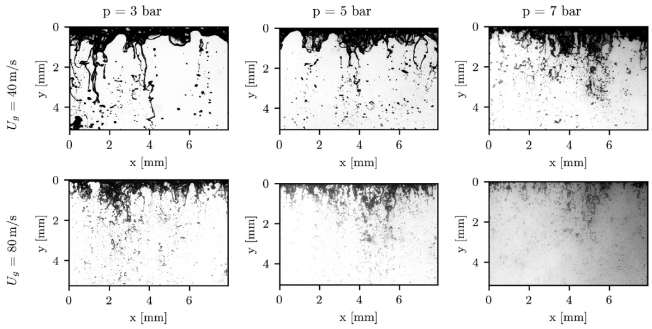

Figure 4.12: Effect of pressure and velocity variation on primary atomization. Adapted from [104].

whereas it was increased to 5 bar in the central column and finally raised up to 7 bar. In the two rows two gas phase velocities were considered (40 and 80 m/s) which are also relevant for the present discussion.
During the normal in-flight operation of an aircraft, an absolute pressure of 7 bar is easily overcame inside the combustion chamber (e.g., 13.5 bar

in [108] under cruise conditions) and the spray behaviour will be more similar to the one illustrated in the pictures on the right. It is easy to imagine that such tiny droplets mostly follow the gaseous phase, due to the very low inertia. Moreover, they will quickly evaporate because of the high temperature of the gas phase due to the heating inside the compressor and the presence of the flame. In a simulation the spray will soon be converted into vapour, playing only a marginal role in the final result (although this influence might be relevant for some specific quantities [100]).
A lower and lower pressure strongly affects the quality of the atomization: at 3 bar, larger droplets can be observed and the primary atomization lasts longer. As a consequence of that, larger droplets will be created, with their own inertia and a minor tendency to follow the gasesous phase. Therefore, they will likely conserve the initial momentum acquired during the breakup process. Moreover, several different breakup mechanisms will take place, probably widening the spray size distribution from very large droplets, generated by the direct breakup of ligaments, and very small ones, for istance from bag breakup (see Ch. 5 for this distinction). This condition is clearly more difficult to be simulated and requires a major care in the setup of the initial conditions of the lagrangian spray.
The effect of velocity is clearly similar, because of the increase in the We and Re number. This is also relevant in the present discussion, considering that flame blow off also progressively reduces the rotation speed of the turbine which in turn decreases the amount of air provided by the compressor. Therefore, moving from standard cruise conditions to altitude relight, also the speed of the air inside the combustor is expected to decrease.
In Fig. 4.13, the variation of SMD with respect to pressure and velocity of the gas phase is reported. In the plot, also the fuel load was varied because of some limitations in the experimental setup. Clearly, a strong effect of both quantities can be pointed out. With the blue rhombus, the best condition (in terms of atomization quality) is underlined: a SMD around 55 μm was observed in this case. Based on the operating conditions reported in [108], an even higher pressure can be expected during cruise, with an even lower average size of the droplets. Conversely, with the red circle the worst atmospheric case is highlighted, characterized by a lower velocity of the gaseous phase and 1 bar of operating pressure. The SMD rises up to 160 μm, providing a totally different SMD if compared to the blue rhombus.
In [107], this last point was considered as representative of altitude relight conditions, but in reality a further pressure decrease up to 0.4 bar can

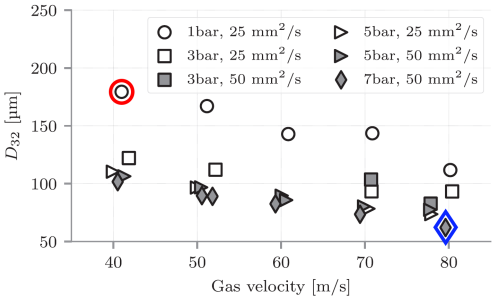

Figure 4.13: Effect of pressure and velocity variation on primary atomization. Blue rhombus: operating point similar to cruise conditions. Red circle: low pressure and velocity as in altitude relight. Adapted [104].

be achieved [109]. Therefore, very large droplets must be expected and evaporation will be negligible because of the very low temperature. As highlighted in the initial section of this chapter, the correct initialization of liquid particles will be of fundamental importance to track their trajectory and understand their interaction with the spark plug.

4.4 Conclusions to Chapter 4

In this chapter, the importance of spray during altitude relight was highlighted starting with a test case recently studied within the SOPRANO project. Many details were omitted for the sake of brevity, but the main outcome of the presented simulation should be quite clear: under altitude relight conditions, the poor atomization quality and the negligible evaporation process underline the need of proper initial conditions for spray injection. Such initial conditions are the result of the primary breakup process that was briefly described in the following section of this chapter. In the end, recent experimental data from a prefilming airblast atomizer were used to assess the large influence of the operating pressure on the atomization quality. Also in this case, the need of a reliable tool to estimate the droplet size distribution of the spray after the primary atomization was highlighted, leading to the numerical procedure illustrated in the next chapter.

Chapter 5

A novel technique to post-process primary breakup simulations

In the present chapter, a novel technique to determine the spray size distribution after primary breakup is presented. This activity is motivated by the need of retrieving accurate initial conditions for the spray to be used in altitude relight simulations, as depicted in Ch. 4. To this aim, the *Eulerian-Lagrangian Spray Atomization* (ELSA) model is used and some commenents on its improvement are provided in the chapter.
Some of the variables available in the solver were used to estimate the characteristics of the spray. Such variable are the liquid volume fraction, the density of liquid/gas interface and the interface curvature. At first, the ratio between the transported liquid volume fraction and density of interface is used to compute the SMD over some planes, in the attempt of monitoring the progress of the atomization process. Secondly, the interface distribution per classes of curvature is introduced: such distribution is used to provide a further analysis of the breakup process. Finally, this two information are combined in the attempt of extracting the *Number Density Function* (NDF) of the spray at a specific distance from the injection, with the aim of using it in simulations like the one reported in Ch. 4.
The novel approach was validated exploiting the experimental data from the test case presented in Sec. 4.3. The prefilmer airblast atomizer was simulated using the ELSA model and post-processed at runtime. As an outcome, the SMD and other spray statistics are correctly predicted with the proposed methodology.

5.1 The ELSA model

In this work, the recent implementation of the ELSA model proposed by Anez et al. [110] was employed with minor modifications. Therefore, in this section only a brief description is provided and the reader interested in a deeper overview of the ELSA approach is addressed to the aforementioned reference [110].
The employed solver (`icmElsaFoam`) is a LES-based approach where the standard *Volume of Fluid* (VoF) solver of OpenFOAM® (`interFoam`) is coupled with the ELSA approach. It is worth noting that the ELSA acronym is kept in this dissertation even if no Lagrangian approach is considered here. Future developments of the model will be addressed to integrate the current `icmElsaFoam` solver with an advanced Lagrangian approach. The continuity and the momentum equations retain the same formulation of a standard incompressible VoF model and are not discussed here for the sake of brevity. Instead, compared to `interFoam`, the standard transport equation for the liquid volume fraction α_l is recast as:

$$\frac{\partial \bar{\alpha}_l}{\partial t} + \boldsymbol{\nabla} \cdot \left(\overline{\boldsymbol{U}} \bar{\alpha}_l\right) + \underbrace{\boldsymbol{\nabla} \cdot C_\alpha \boldsymbol{U}_r \bar{\alpha}_l \left(1 - \bar{\alpha}_l\right)}_{ICM} = \underbrace{\left(1 - C_\alpha\right) \boldsymbol{\nabla} \cdot \left(\boldsymbol{R}_{\alpha_l}\right)}_{ELSA} \quad (5.1)$$

$\overline{\boldsymbol{U}}$ is the Reynolds averaged mixture velocity, $\boldsymbol{U}_r = |\overline{\boldsymbol{U}}| \frac{\boldsymbol{\nabla} \bar{\alpha}_l}{|\boldsymbol{\nabla} \bar{\alpha}_l|}$ is the relative velocity between phases and $\boldsymbol{R}_{\alpha_l} = \frac{\nu_t}{Sc_t} \boldsymbol{\nabla} \bar{\alpha}_l$ is the sub-grid diffusion of $\bar{\alpha}_l$ typical of the ELSA model. C_α acts as a blending function between the two methods: if $C_\alpha = 1$ the interface between liquid and gas is well resolved and the *Interface Capturing Method* (ICM) is applied. Instead, in the ELSA part $C_\alpha = 0$ and the interface is considered diffused.
To switch between the two approaches, two *Interface Resolved Quality* (IRQ) sensors are introduced [110], which were used in this work to assess if the employed grid size was sufficiently fine to resolve most of the turbulent fluctuations taking place at the interface between liquid and gas. If not, local results were discarded as pointed out in the next paragraphs of the work.
Before introducing the IRQs, it is worth spending a few words about the transport equation of the density of interface Σ, which represents the main variable in the ELSA framework. As a result of the derivation of the equations in the LES formalism, in [110] the overall density of interface Σ is split into two components, namely $\Sigma = \Sigma_{min} + \Sigma^{'}$. In this expression, Σ_{min} represents the density of interface related to the presence of any fraction of liquid within the control volume, while $\Sigma^{'}$ is the amount of additional surface introduced by turbulent fluctuations. $\Sigma^{'}$ is transported

across the computational domain using Eq. 5.2:

$$\frac{\partial \Sigma'}{\partial t} + \boldsymbol{\nabla} \cdot \left(\overline{\boldsymbol{U}} \Sigma'\right) = \boldsymbol{\nabla} \cdot \left[\frac{\nu_t}{Sc_t} \boldsymbol{\nabla} \Sigma'\right] + C_\Sigma \frac{\Sigma}{\tau_\Sigma} \left(1 - \frac{\Sigma}{\Sigma^*}\right) \tag{5.2}$$

where ν_t and Sc_t are the turbulent SGS viscosity and the Schmidt number respectively. The source term on the RHS is designed so that the overall density of interface Σ tends to an equilibrium value Σ^* over a certain time scale τ_Σ. The unknown terms closure used by Anez et al. [110] is here retained. The reader interested in further details on this topic is addressed to the provided reference. It is worth mentioning that Eq. 5.2 is also coupled with Eq. 5.1 since it contributes to the evaluation of C_α, as it will be shown in the next. However, in the past it was also used to enrich the description of the momentum transfer between the two phases [111] and to evaluate the evaporation rate of an evaporating spray [112]. A different definition of Σ_{min} was preferred here (Eq. 5.3):

$$\Sigma_{min} = |\boldsymbol{\nabla} \overline{\alpha}_l| \tag{5.3}$$

This equation comes from a similar reasoning to the one presented in [113] regarding the computation of the flame surface density in combustion modelling. As in [113], it exploits the possibility of calculating the density of interface of a variable that is smeared over a few elements in the computational domain and does not variate sharply over a single cell. For the sake of clarity, the equation used in [110] reads:

$$\Sigma_{\text{min}} = \frac{2.4\sqrt{\overline{\alpha}_l \left(1 - \overline{\alpha}_l\right)}}{a} \tag{5.4}$$

Which is based on the idea if either $\overline{\alpha}_l = 1$ or $\overline{\alpha}_l = 0$ the interface is zero. The coefficients are then designed to recover the minimum amount of surface (corresponding to a flat surface) inside in a spherical volume which contains the amount of liquid determined by $\overline{\alpha}_l$. Although the reasoning behind that is not wrong, it does not consider the interface smearing and rapidly produce an artificial increase in the predicted amount of surface. In fact, in `interFoam`, despite the use of an interfacial compression flux term to mitigate the effects of numerical smearing [114], the interface is spread over a few cells, even if a sufficiently small grid size is used. For instance in Fig. 5.1, a globally good representation of the spherical shape is obtained, but the interface is poorly represented locally [114]. The previous formulation of Σ_{min} (Eq. 5.4 [110]), which just takes into account the amount of $\overline{\alpha}_l$ in a cell soon produces a certain overestimation of the amount of interface. For a better prediction, the surrounding

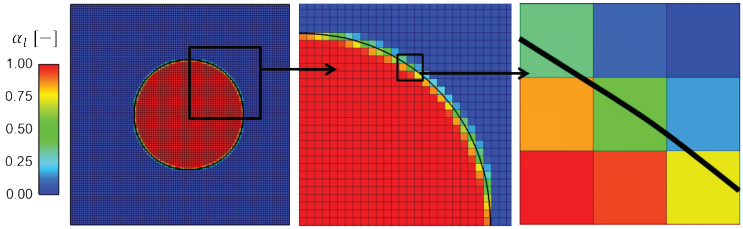

Figure 5.1: Numerical smearing of the interface of a 2D droplet. Adapted from [114].

computational cells must be taken into account as well: Eq. 5.3 allows to consider the local smearing of the interface. It must be said that in highly turbulent test cases like the one studied by Anez et al. [110], a sudden production of Σ' soon covers the over-prediction of Σ_{min} (since $\Sigma' \gg \Sigma_{min}$) and no main errors are introduced as $\Sigma \approx \Sigma'$. Here, due to relatively low turbulence intensity of the studied test case, a different equation was necessary to better describe the amount of interface under lower turbulence intensities.

To provide a preliminary validation of the novel formulation, a 3D sphere of liquid was initialized into a control volume with a uniform mesh size (Fig. 5.2). The `icmElsaFoam` solver was run for a sufficient time, in order to let the artificial interface compression algorithm stabilize the surface of the liquid, providing the typical interface smearing already seen before. No turbulence or bulk velocity is here considered, so that the only responsible for liquid movement is the artificial compression algorithm. For the same reason, no Σ' is generated. The amount of surface is computed as the integral per unit of volume of $\Sigma = \Sigma_{min}$, which provides S_Σ in the plot. S_{theory} is the theoretical surface of the spherical droplet considered. It can be pointed out that a very good estimation is provided from Eq. 5.3 when the mesh size falls over a certain level. In fact, the prediction gets more and more reliable when the interface of the droplet is well-resolved. It must be pointed out that in practical cases using more than 100 cells to discretize the smaller entity of liquid is not feasible. Anyway, as it can be observed from Fig. 5.2, the prediction of the theoretical amount of surface is still reliable up up to 5 cells in the diameter which can be easily achieved with a relatively low computational effort.

On the other hand, Eq. 5.3 seems to fail when very diluted spray is considered and only a few cells can be used to describe liquid structures (left side of 5.2): from the authors perspective, this issue should be

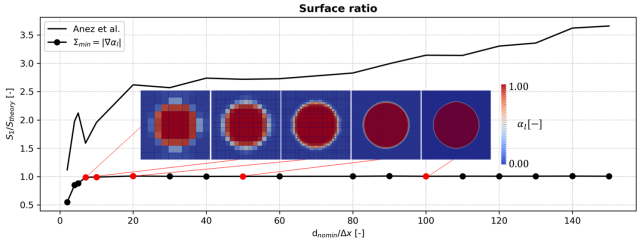

Figure 5.2: Comparison between different equations for Σ_{min} in terms of theoretical to computed surface.

compensated by very high values of Σ', when practical cases are considered under turbulent conditions. Indeed, further work is needed on this point but at the present day no additional considerations are made. This is also justified by the focus of the work on the primary breakup region, where a quite small mesh size is usually adopted. For the sake of comparison, also Eq. 5.4 is reported in Fig. 5.2 to highlight the overestimation derived from such formulation, as already discussed above.
Finally, the two IRQ sensors can be introduced:

$$IRQ_\Sigma = \frac{\Sigma_{\min}}{\Sigma} \quad , \quad IRQ_k = \frac{1}{\Delta k} \tag{5.5}$$

IRQ_Σ is defined as the ratio between the resolved and the overall density of interface. Clearly, if $IRQ_\Sigma \to 0$ the ELSA approach will be more appropriate than the VoF, as most of the interface is modelled. Instead, IRQ_k is based on curvature and mesh size: if the curvature is too high compared to the local grid, then the ICM approach is not able to capture the interface anymore and ELSA must be preferred. The switch between the two methods is not smooth for stability issues and threshold must be imposed so that:

$$C_\alpha = \begin{cases} 1, & \text{if } IRQ_\Sigma > 0.5 \text{ or } IRQ_k > 1.0 \\ 0, & \text{otherwise} \end{cases} \tag{5.6}$$

It is worth pointing out that if the ICM method is considered, also the surface tension is taken into account as currently done in `interFoam`.
As it will be clarified later, only the resolved (ICM) part is considered in this work to exploit the curvature of the interface. The reader might argue that there was no need to adopt the coupled `icmElsaFoam` solver

rather than the only `interFoam`. The main advantage of using ELSA lies in the availability of the IRQ sensors, which allows to understand when the liquid phase is sufficiently well resolved to trust the output of the ICM technique, or when a purely diffused interface approach must be considered. For a reliable calculation of the curvature, which is used in the post-process, the interface must be well-resolved. To this aim, a very fine mesh is normally required, which would be in contrast with the engineering purpose of the present work, which focuses on a cost-effective and affordable method to extract spray BC from CFD, rather than rely on experimental correlations or experiments. To this aim, a relatively coarse mesh was used in the the whole domain whereas a strong local refinement was only adopted in the atomization region. Yet there is no way to determine whether liquid structures are well-resolved or not, also considering that the mesh requirements may vary in time due to the large velocity fluctuations. Here the `icmElsaFoam` approach comes in help with the previously mentioned IRQs, that provide a rough idea of the reliability of the ICM method. It was observed that the IRQs were always respected in the refined region, while they are not outside, and thus no data are collected over there.

5.2 Description of the post-processing procedure

Recently in Braun et al. [115], the *Smoothed Particle Hydrodynamics* (SPH) method was used to simulate in detail the liquid structures originated by the primary breakup. Thanks to a very low mean inter-particle distance, even very small liquid structures are captured and the primary atomization process is represented very accurately. Regarding the post-processing technique, in the work of Braun et Al. [115] the use of SPH allows a straightforward handling of phase interfaces. To post-process the simulation, gaseous particles were firstly removed to reduce the memory requirements and an enclosing surface mesh was extracted based on the remaining liquid particles. Then, tessellation was performed using the α-shape algorithm and the resulting triangulated surface is fed into a cluster detection algorithm based on the Connected Component Labeling (CCL). In this way, each cluster can be analysed individually: the clusters having an almost spherical shape are considered to compute spray statistics.
Similarly in [107], to quantitatively post-process a VoF simulation, a sampling plane at the domain outlet was defined and a CCL algorithm was again used to detect connected liquid structures based on a certain minimum volume fraction in each cell. This way, the number of formed droplets was determined. Moreover, once a connected structure was de-

tected, the surface area of each one was quantified by the sum of all cells containing liquid with the corresponding volume fraction and the grid size. Finally, the droplet diameter was derived by assuming a circular section. It is worth pointing out that, in this case, the final result was also influenced by the minimum liquid volume fraction value (or threshold) chosen to carry out the detection.
The common idea behind the reported examples is to carry out droplet identification by a clustering algorithm, which introduces the need to store a large amount of data [115] and to assume a certain threshold of liquid volume fraction [107]. The novel post-processing technique is composed of two stages. First, the density of interface Σ is used to compute the SMD then, the mean curvature k is employed to obtain the NDF. It is worth pointing out again that, to apply the proposed procedure, it is not necessary to store several instantaneous snapshots of liquid distributions. Moreover, compared to other approaches based on a VoF method, the technique is not dependent on the assumed threshold of liquid volume fraction used to carry out the identification of the droplets.

5.2.1 SMD calculation

The SMD (or d_{32}) of a spray is defined as the ratio between the amount of liquid volume and its surface [85]. Based on that, two definitions can introduced depending on the strategy used to track the liquid phase. On the one hand, if information about single droplets is available, it is convenient to calculate the SMD as (Eq. 5.7):

$$d_{32}^{L} = \frac{\sum_i d_{p,i}^3}{\sum_i d_{p,i}^2} = 6\frac{V_l}{A_l} \tag{5.7}$$

where $d_{p,i}$ is the diameter of the i-th droplet, whereas V_l and A_l are respectively the volume and the area of the considered the portion of spray.
On the other hand, using the variables introduced so far by the ELSA approach, if a control volume V is considered, then the d_{32} can be computed integrating (Eq. 5.8):

$$d_{32}^{E}(V) = 6\frac{V_l}{A_l} = 6\frac{\iiint_V \overline{\alpha}_l dv}{\iiint_V \Sigma dv} \tag{5.8}$$

where dv stands for the volume element of the integration. In Fig. 5.3 the difference between d_{32}^{L} and d_{32}^{E} is graphically explained. d_{32}^{L} is used in experimental measurements, Eulerian-Lagrangian simulations (e.g.,

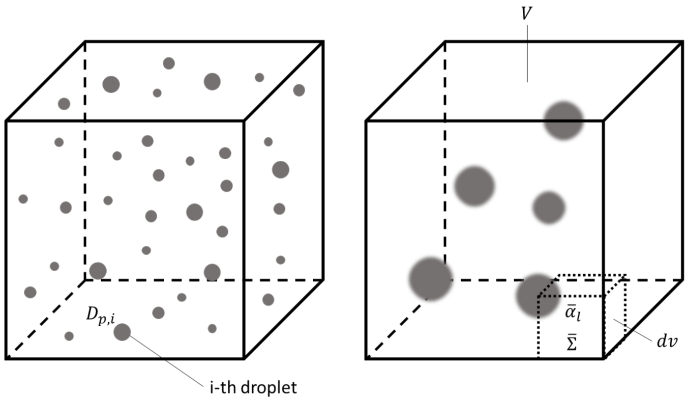

Figure 5.3: Conceptual difference between SMD definitions. Left: based on discrete droplet diameters (d_{32}^L - Eq. 5.7), right: based on phase indicator α_l and interface density (d_{32}^E - Eq. 5.8).

Ch. 3) or ICM computations through interface recognition, but it can not be directly adopted in VoF simulations. On the other hand, d_{32}^E can be directly adopted in the considered framework, without requiring additional considerations on droplet identification. From a theoretical point of view, if $\overline{\alpha}_l$ and Σ are well defined, the two definitions should lead to the same result, $d_{32}^L = d_{32}^E$.
From a simulation point of view, it is usually more convenient to compute the SMD of the droplets flowing trough a given plane S. Therefore, starting from Eq. 5.8, Eq. 5.9 can be written:

$$d_{32}^E(S) = 6\frac{\int_T \iint_S (\overline{\alpha}_l \boldsymbol{U} \cdot \vec{n} ds)dt}{\int_T \iint_S (\Sigma \boldsymbol{U} \cdot \vec{n} ds)dt} \tag{5.9}$$

where S stands for the surface over which a time average SMD is computed within the timeframe T. $\vec{n}$ is the normal to the surface S and $\boldsymbol{U} \cdot \vec{n}$ is the component of the mixture velocity normal to S. This also corresponds to the output which is usually available from experiments, where only particles crossing a certain plane are considered. A sketch of this concept is provided in Fig. 5.4 (left).
While this already represents an interesting way to compute the SMD for a given plane, SMD distributions in space could be of use rather than a uniform value (e.g., for non-uniform injection of Lagrangian droplets in

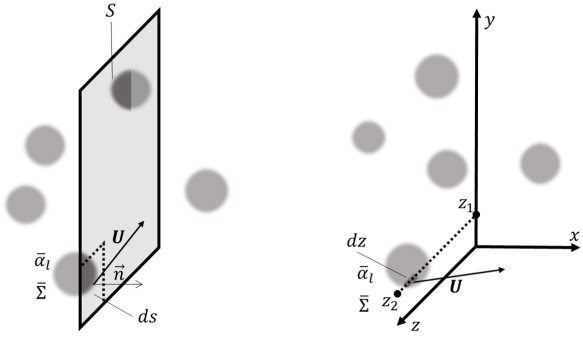

Figure 5.4: Graphical representation of the post-processing technique applied to compute the SMD: left, over discrete planes (Eq. 5.9) and right, over discrete lines (Eq. 5.10).

space or just to compare against experiments).
In this work, the SMD distribution was computed also over discrete lines. Given a certain reference frame (x, y, z), the SMD variation along y can be computed for a constant value of x_0 by integrating over z as follows:

$$d_{32}^{E}(x_0, y) = 6\frac{\int_T \int_{z_1}^{z_2} (\overline{\alpha}_l(x_0, y, z)\boldsymbol{U}(x_0, y, z) \cdot \vec{x}dz)dt}{\int_T \int_{z_1}^{z_2} (\Sigma(x_0, y, z)\boldsymbol{U}(x_0, y, z) \cdot \vec{x}dz)dt} \tag{5.10}$$

Eq. 5.10 is illustrated in Fig. 5.4 (right). The output of the presented equation will be clarified in the next sections, but it is now worth mentioning its potential. For instance, if a simplex atomizer is considered, with an axisymmetric design, the radial SMD variation could be computed at a given axial distance from the injector, providing also an idea of the angular dispersion of the spray.

5.2.2 Spray Size Distribution estimation through curvature

While in the previous section a way to estimate the SMD was proposed, no information is yet available on the size distribution of the generated spray. Nevertheless, very different distributions can still provide the same SMD but largely affect the ignition process due to the different evaporation

and combustion time-scales associated with each class of diameter. In this work, we also propose an approach to extract spray distribution by analyzing the liquid/gas interface mean curvature k.
The reader interested in an exhaustive discussion about curvature in sprays is addressed to specific literature (see [116] and references therein). Hereby, the idea introduced by [116] on a *Homogeneous Isotropic Turbulence* (HIT) box to extract the NDF is exploited on a more complex test case. In [116] the Gauss $G = k_1 * k_2$ and the mean $H = \frac{k_1+k_2}{2}$ curvatures were computed from the two principal curvatures of the surface k_1 and k_2, following the method presented in [117]. This two principal curvatures were computed with two alternative post-processing techniques: one based on the level-set function available in the employed solver ARCHER [118] and the the second one based on gas-liquid interface discretization with a 2D triangulated mesh [119].
While, in [116] several detailed analysis on liquid curvature evolution were carried out, here only the idea of looking at interface curvature to analyze the primary-breakup process and compute the NDF is exploited, with a less demanding computational approach, on a configuration of technical interest.
Therefore, the mean curvature already implemented in OpenFOAM ® for the estimation of the surface tension forces was used:

$$k = -\boldsymbol{\nabla} \cdot \left(\frac{\boldsymbol{\nabla} \overline{\alpha}_l}{|\boldsymbol{\nabla} \overline{\alpha}_l|} \right) \tag{5.11}$$

The reader interested in a detailed review of curvature computation in OpenFOAM is addressed to specific literature [114, 120].
Similarly to [116], several classes of k were created and used to store the associated total amount of interface $\Sigma\, dv$. It is worth specifying that the overall amount of interface is considered since $\Sigma\, dv = (\Sigma_{min} + \Sigma^{'})\, dv$. However, it was verified that the contribution of $\Sigma^{'}$ is not relevant in the considered case since statistics were collected only where the IRQ sensors indicated that the interface was well resolved and thus $\Sigma_{min} \gg \Sigma^{'}$. In this framework, k is not used to estimate the amount of interface, but only to understand to which class of curvature it must be attributed. Therefore, despite k being defined everywhere, the PDF is actually populated only when $\Sigma\, dv \neq 0.0$ and therefore some amount of interface can be found. Such procedure was coded in OpenFOAM by directly storing at runtime the amount of surface associated with predefined classes of curvature in a predefined control volume.
Some additional steps were still necessary to *translate* the curvature

distribution into a NDF: first of all, negative curvature values were discarded. As it will be clear in the next sections, such values can be associated with the presence of non-spherical liquid entities with concave parts, that are not considered at this stage. Now, different classes of diameter can be defined as $d_k = 4/k$ and the number of drops for each of these classes can be computed as as $N(d_k) = \Sigma\, dv/\pi d_k^2$.
In the studied test case, the resulting NDF still presents a very long tail towards large diameters. Such diameters are not relevant in terms of numbers of droplet, but they still strongly affect the final SMD. Keeping that in mind, we propose to cut out the tail of the NDF in order to match the local value of SMD computed thanks to Σ and $\overline{\alpha}_l$.
In this way, larger structures with concave (negative curvature) and almost flat (large diameters) parts are not considered in the NDF computation.

5.3 Investigated test case

In this section, a few additional details about the experimental test case presented in Ch. 4 are provided. Then, the some preliminary single phase simulations are discussed and in the end, the numerical setup of the ELSA simulation is introduced.

5.3.1 Experimental setup

The numerical approach presented in the previous sections was applied to investigate the planar prefilming airblast atomizer already introduced in Ch. 4 [98, 104, 105, 106, 107]. Its description is not repeated here, although it is worth mentioning that a single operating point at atmospheric pressure was selected for this simulation, with a nominal gas phase velocity of 40.0 m/s. Several liquids were investigated experimentally, but in this case *Shellsol D70* was chosen. The reported thickness of the prefilmer trailing edge is 230.0 μm. A summary of the operating conditions is reported in Tab. 5.1.

5.3.2 Preliminary single phase simulations

The great influence of the gaseous flow field on the atomization process leads to the requirement of accurate, time-dependent boundary conditions. In [107, 121], the concept of embedded *Direct Numerical Simulation* (DNS) [122, 123] is exploited to obtain high-fidelity time-dependent BCs for the gaseous phase, in order to take into account the turbulent fluctuations generated inside the prefilmer channel. A similar strategy was adopted here (Fig. 5.5): at first, a single-phase LES of the whole prefilmer

Parameter	Value
Gas phase pressure	1 atm
Gas phase velocity	40 m/s
Gas phase density	1.225 kg/m^3
Gas phase kinematic viscosity	1.48 e^{-05} m^2/s
Liquid phase velocity	0.5 m/s
Liquid phase density	770 kg/m^3
Liquid phase kinematic viscosity	2.026 e^{-06} m^2/s
Liquid phase surface tension	0.0275 kg/s^2
Prefilmer edge thickness	230 μm

Table 5.1: Operating conditions and liquid fuel properties considered in the numerical simulation.

apparatus was performed. The grid is composed by hexaedral elements with a base size equal to 0.5 mm, while a mesh grading was applied on the prefilmer lip to further refine the mesh in this area. The total number of elements amounts to 4.7 M. The simulation employs second order schemes for the momentum and a dynamic Smagorinsky model to account for the sub-grid scales of turbulence. A mean velocity of 40.0 m/s was applied to the inlet boundary and a turbulence intensity of approximately 10 % was superimposed to generate velocity fluctuations. As a validation, the velocity profiles at 0.3 mm downstream the atomizing edge are compared to the experiments in Fig. 5.6. A good agreement is achieved both in terms of mean velocity and RMS.
Then, the instantaneous velocity vectors were recorded on a plane and used as BCs for a second single phase simulation, similar to the *turbulent channel* used in [107]. This intermediate step was necessary to increase the definition of turbulent eddies close to the wall and the boundary layer. Moreover, in [107] the direct use of the turbulent channel to derive the BCs lead to the lack of the temporal history of the flow field related to the prefilmer itself. In fact, the resulting profiles would be more affected by the modelling assumption at the inlet of the turbulent channel (i.e., the turbulence intensity at the inlet and the chosen sub-grid model) than the effective geometry of the test case. Instead, the strategy adopted here does not apply directly a turbulence generator to the channel inlet, but a flow field obtained from a simulation representative of the whole rig.
This second domain has a rectangular section where the cell size ranges from 200 μm in the freestream up to 50 μm near the wall. To this aim, two refinement steps were performed, each of which halves the previous sizing, leading to a final amount of 5.35 M elements. The simulation

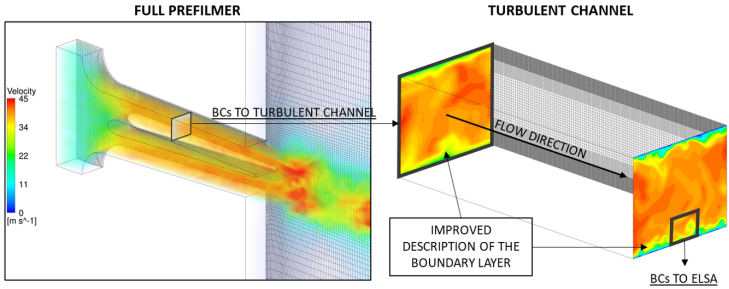

Figure 5.5: Schematic representation of the two mapping procedures carried out to obtain time varying velocity BCs for the ELSA simulation.

employs the same modelling choices of Step 1.
Moving from the inlet to the outlet, the flow field becomes more turbulent close to the wall and the resolution of wall eddies is increased. This clearly leads to a more realistic prediction of the atomization process due to the absence of strong assumption on the boundary layer.
The achieved velocity profiles are finally sampled at the outlet, providing a suitable temporal window for the subsequent multiphase simulation.

5.3.3 Numerical setup of the ELSA computation

Following the work of Warncke et Al. [107], the multiphase simulation was performed on a reduced domain representative of the last section of the prefilming edge (Fig. 5.7). Two inlets are present for the gas phase, where the air velocity was prescribed following time-varying profiles mapped from the single phase simulation. The liquid is injected through a dedicated inlet (0.10 mm thick) with imposed mass flow rate and a uniform velocity profile. Therefore, the liquid flows over the prefilmer which is treated as a no-slip wall. The discretized section of the prefilmer is 1.00 mm long and 0.230 mm thick. The chosen length, allows to consider the formation of small waves (observed also in [107]) which may influence the atomization process whereas the thickness was measured experimentally [115]. Lateral boundaries are modeled as symmetrical, while the remaining ones (top, bottom and outlet) are considered as freestream BCs.
The primary breakup requires a very fine mesh on the prefilmer surface and in the region near the lip. If the mesh resolution is high enough, the

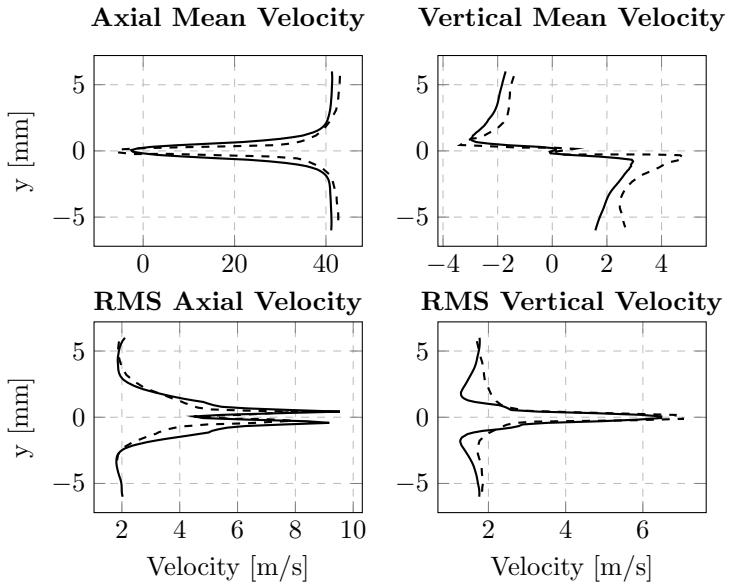

Figure 5.6: Comparison between the single-phase numerical simulation (——) and the experimental data (- - -) 0.3 mm downstream the atomizing edge.

atomization process is well described, but it is not convenient in terms of computational effort. Consequently, in this study our focus is limited to a small region close to the prefilmer lip, where a fine hexahedra mesh was used. Outside this zone, the size of the elements is doubled and it only serves to avoid the influence of boundary conditions on the relevant test-section. The final size for the cells near the prefilmer surface is 10.0 μm and the total number of cells is about 5.5 M.

A second order backward time scheme was used for all quantities except for $\overline{\alpha}_l$, where a special procedure called MULES was used to preserve boundedness of this quantity [110]. The time step was set to $1.5 \cdot 10^{-07}$ s. The WALE model was employed to account for the effects of sub-grid turbulent viscosity.

In Fig. 5.8 the locations used to post-process the simulation are shown. On the left, discrete planes for SMD computation are represented: the first one is located at the end of the prefilmer lip, while the last one is placed

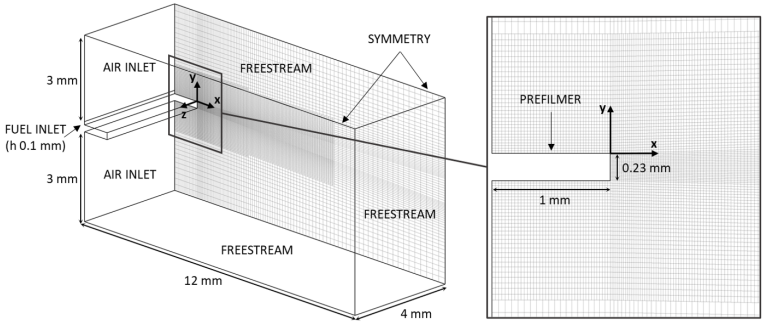

Figure 5.7: Numerical domain, reference frame, boundary conditions and employed mesh.

6.00 mm downstream. The distance between each of them is 0.50 mm and, as already said, they only extend in the refined mesh region. On the right, the boxes for curvature storage are shown. In OpenFOAM, a piece of code was directly introduced in order to store liquid/gas interface curvature at each time step in the given location. For the sake of clarity, it would have also been possible to implement such storage on some planes, as already done for the SMD. However, this would have strongly complicated the implementation of the algorithm, since interpolation would have been required. Since this thesis represents the first attempt to exploit this approach, a simpler strategy was preferred.

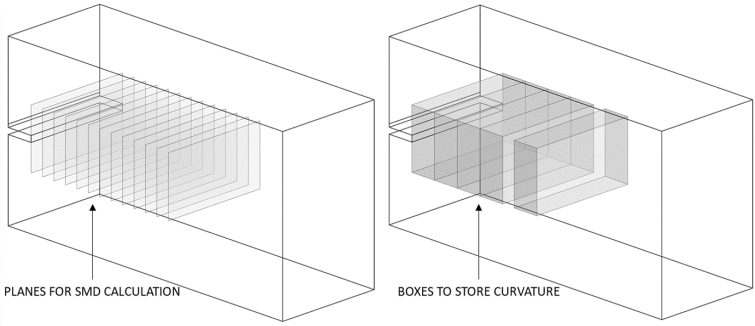

Figure 5.8: Post-processing locations: planes used to compute SMD (left) and boxes to store surface distribution in classes of curvature (right).

5.4 Results

In this section, the results obtained with the presented approach on the investigated test case are shown. At first, a qualitative description of the structures generated by the atomization process is provided, employing the data from the simulation only. Later, the prediction of the SMD using Σ is discussed and used to describe the progress of the atomization process. Finally, the interface curvature k is employed to provide a continuous description of the atomization, from the injector lip up to spherical droplets.

5.4.1 Qualitative description

A qualitative outlook of the investigated phenomenon is provided in Fig. 5.9, where two instantaneous isosurfaces at $\alpha_l = 0.5$ are reported for the considered test-case. The main characteristics of this kind of atomization are represented by the simulation: the liquid flows from the inlet over the prefilmer surface, where some waves are generated due to the aerodynamic interaction with gaseous phase flowing above it. Later, the liquid is accumulated at the prefilmer lip (or trailing-edge) forming the so-called *reservoir*. Here, the accumulated liquid is deformed and can eventually detach from the prefilmer. In Fig. 5.9, two different events are shown, in order to provide the reader a brief overview on the main structures that are generated during the primary breakup under the prescribed operating conditions. On the left side, the beginning of a

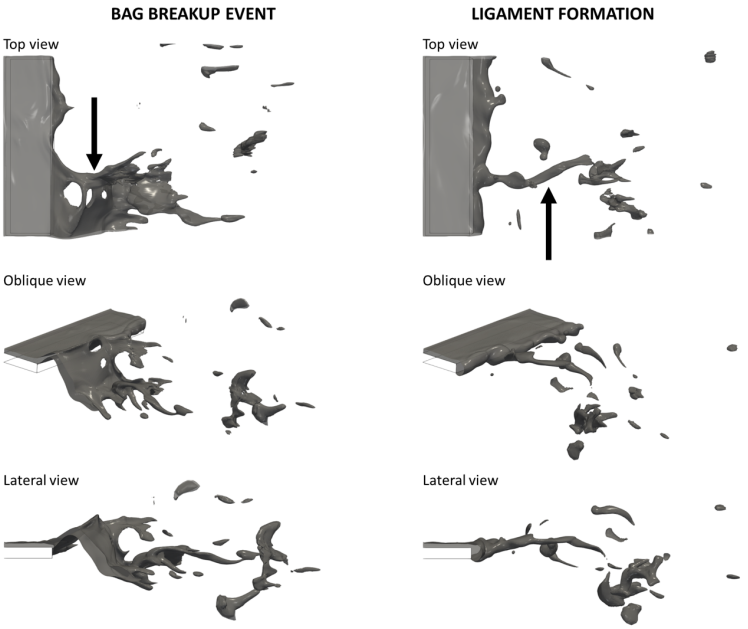

Figure 5.9: Qualitative representation of the investigated phenomenon, using an isosurface at $\alpha_l = 0.5$: bag breakup event on the left, ligament formation on the right.

bag breakup event can be identified: out of the reservoir a bag is formed which subsequently will burst, generating many small droplets [107]. On the right side, the formation of a ligament can be pointed out: ligaments will eventually detach from the reservoir, forming some spherical droplets because of the stabilization effect of the surface tension force.
It is out of the scope of this thesis to describe in detail the atomization process and analyze how a simulation can reproduce the physical phenomena involved in primary breakup. This objective was already very well accomplished in the previous works by Warncke et Al. [107], where `interFoam` is operated as laminar (i.e., DNS), and by Braun et Al. [115], where SPH is used to reproduce in extreme details even the smallest liquid structures (in those two references air velocity was set to 50 m/s, while here the case at 40 m/s was preferred).

From Fig. 5.9, it is clear that the same spatial resolution of [107] and [115] is not achieved by the present calculation and only the largest liquid structures appear with the selected threshold of α_l. Indeed, Fig. 5.9 also shows that the main atomization features highlighted numerically [107, 115, 124, 125] and experimentally [98, 105, 106, 107] can still be identified with a relatively coarser mesh.
The unique shortcoming that can be pointed out from the cited references is the very large amount of computational resources needed to carry out those simulations (approximately 540 k CPUhs in [107] and 3.6 M CPUhs in [115]). Therefore, their direct application to retrieve some spray initial conditions in an engineering context is not yet very attractive, although they surely represent a reference for scientific purposes.
Due to the engineering relevance of this work, a rather coarse mesh is here employed within the LES framework. In this way it is still possible to catch most of liquid structures depicted so far by keeping the computational effort relatively moderate. In fact, about 11 k CPUhs were necessary to run the present simulation for approximately the same physical time of [107, 115].

5.4.2 SMD prediction

In Fig. 5.10 the SMD was computed for discrete planes at a given distance from the prefilmer lip using Eq. 5.9 for the considered timeframe T of LES averaging (planes are reported in Fig. 5.8). The first point of the plot reports the SMD in correspondence of the prefilmer trailing edge (0.0 mm): the predicted value (roughly 255 μm) is comparable with the prefilmer thickness (230 μm). Clearly, there is no point in defining a diameter of a mostly flat, coherent surface of liquid, whereas talking about a characteristic *length* would be more appropriate at this stage. But independently from the chosen nomenclature, such information could still be useful if the mass transfer in the dense region is of interest (see for instance [112]).
At 0.50 mm the computed SMD is even higher and still larger than the prefilmer thickness. Despite the fact that now the liquid as both an upper and a lower interface, theoretically reducing the SMD (as it is not in contact with the prefilmer anymore), a larger value is detected compared to the previous point at 0.00 mm. In fact, the size of the accumulation is larger that the one of the film created over the prefilmer surface and the proposed method correctly detects that.
Already at 1.00 mm, the deformations of the liquid accumulation provide a lower SMD, which indicates the formation of smaller liquid structures, although they could still be attached to the resorvoir (ligaments for

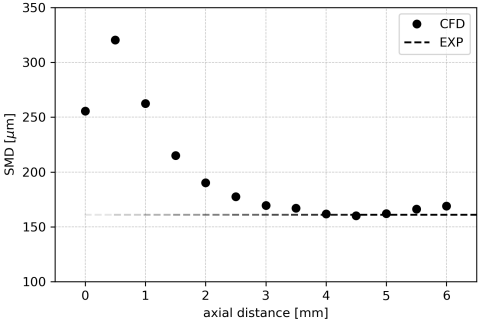

Figure 5.10: Axial variation of the SMD calculated over discrete planes at different distances from the injector (note that experimental datum is referred to the whole investigation window and cannot be attributed to a specific distance from the prefilmer lip, see Sec. 5.3.1).

instance).
By increasing the axial distance from the prefilmer, the beginning of the primary breakup can be pointed out. From 1.5 mm up to 3.00 mm the predicted SMD strongly decreases: here, most of the primary breakup is taking place and smaller and smaller liquid structures are generated. For the sake of completeness, part of the reduction in predicted SMD may also be due to some larger liquid structures flowing out of the considered domain, due to the flapping of the jet and the limited thickness of the region with the finer mesh. Further work will be necessary to understand the ideal size of the refined zone.
Moreover, it is important to note that even at this stages, non-spherical entities can be observed. However, the employed post-processing technique does not yet allow to distinguish between almost spherical droplets and non-spherical structures. This would be possible by exploiting the concept of Mean and Gauss curvatures already discussed in [116]. Anyway, it is important to notice that a reduction in SMD is recovered as expected.
Finally, from 3.00 mm to 6.00 mm, no major variations can be noticed. It indicates that most of the primary breakup takes place before, while here the SMD stabilizes between 160.0 - 170.0 μm. Considering that the variation is limited, any of these planes could be used to derive an initial SMD for a separate dilute spray simulation.
The lower value of SMD (160.13 μm) is reached at a distance of 4.50 mm

from the prefilmer trailing edge while later a slight increase in SMD is recovered. This could be due to the following phenomena:

- coalescence;
- stabilization of deformed liquid structures into spherical droplets (lower amount of interface for the same amount of liquid volume);
- smallest structures flowing out of the considered refined zone;
- diffusion of the interface.

All the cited phenomena could play a role, anyway it is important to highlight again how their effect is limited and would not strongly affect a separate simulation run with such SMD as an initial condition. In the next sections, the SMD value (162.03 μm) computed at a distance of 5.00 mm from the lip will be used for further considerations. Such distance was chosen *a priori*, following the lead of [107] but *a posteriori* selection using the minimum value at 4.50 mm would have been more appropriate. Finally, in order to further validate the approach, the experimental datum is reported in Fig. 5.10. Although the agreement could be considered extremely satisfying, it is worth pointing out how this value is computed from experiments: as described in [105], instantaneous images are taken and spherical entities in the whole sampling window are identified using a dedicated algorithm, storing the detected diameter. Non-spherical liquid structures are instead discarded and not considered in for the calculation of the SMD. Finally, several independent images are analyzed and the SMD is computed. It is not possible to define a single axial distance where the SMD is calculated. A fading line is here plotted, meaning that the indicated value makes more sense moving farther from the trailing edge, where the primary breakup can be assumed to be finished.
For the sake of clarity, the differences with the proposed numerical approach are summarized below:

- in experiments the full domain in considered while here only discrete planes at specified distances are used.
- It is still impossible to distinguish between almost-spherical and non-spherical entities, meaning that all the liquid structures are accounted for the numerical calculation of the SMD.

Regarding the first point, we believe that the plateau shown in Fig. 5.10 indicates that additional breakup is not taking place downstream, making the two dataset comparable. On the second point, the work of Canu et al. [116] could help to address this issue. While small entities are more

likely to have a spherical shape, the larger ones could still present relevant distortion. Identifying and not accounting for the largest non-spherical structures could produce a reduction in the calculated SMD, which would align the result of this work with the slight underprediction already noticed in [115] and [107].
To conclude, we believe that the comparison against experimental data is not completely consistent in this case and we advice the potential reader that the same agreement could not be achieved if the present method was improved. Although, also considering the preliminary validation given in the previous section, this strategy could be already employed to obtain a sufficiently accurate and affordable prediction of the global SMD, to be used as a starting point for a subsequent simulation of the dilute spray.
If the distribution of the SMD is of interest, then Eq. 5.10 can be used in the attempt of recovering the spatial distribution (Fig. 5.11). This information could be useful if a more refined injection is planned (using a non uniform value of SMD) or for validation purposes. In Fig. 5.11,

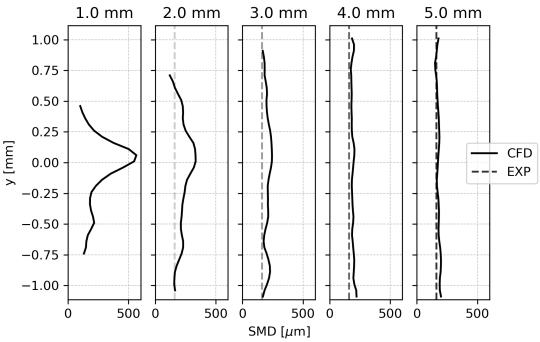

Figure 5.11: SMD distribution along vertical axis at specified distances from prefilmer lip, plotted only where time averaged liquid volume fraction is larger than 0.001 (note that no profile is available from experiments and the experimental line is plotted just for immediate reference.)

y denotes the component normal to the prefilming surface and y = 0.00 mm corresponds to the centre of the prefilmer trailing edge. Each plot is obtained at a certain axial distance from the prefilmer trailing edge (similarly to Fig. 5.10). The z direction in Eq. 5.10, where the integration is performed, corresponds to the z coordinate in Fig. 5.7. In order to discard the points where not enough liquid was sampled, the lines are

plotted only where time-averaged $\alpha_l \geq 0.001$.
At 1.00 mm a large variation of the SMD can be observed along y, revealing that the largest liquid structures are still concentrated close to the prefilmer lip. Later (2.00 and 3.00 mm) this peak starts to disappear. Finally, by analysing the same output at 4.00 and 5.00 mm, the SMD is almost uniformly distributed along the considered height.
Again, it is worth recalling that only a single value of SMD was available from the experiments referred to the whole investigation window. Therefore the experimental line shown in Fig. 5.11 is not meant to directly compare against the CFD data in each point, but only serves as reference to indicate that a fair prediction was obtained.
Finally, it is also worth to comment the evolution of the time-averaged Σ as a function of the distance from the prefilmer. In the experiments carried out in [126] via the Ultra-Small Angle X-Ray Scattering (USAXS) method and in the set of related CFD simulations reported in [127], it was shown that the evolution of the amount of interface can be used to estimate the intact length of the fuel flowing out of an automotive injector. In fact, it was observed that the projected area density increased moving away from the nozzle due to the breakup. In Fig. 5.12 the evolution of the mean Σ is shown on some planes at a specified distance from the injector lip (they are some of the ones shown in Fig. 5.8 and used for the previous analysis). As a difference from the cited works, here the liquid is not

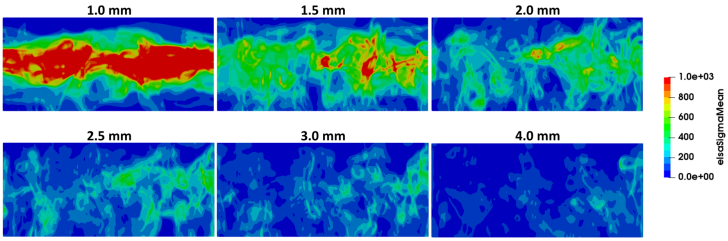

Figure 5.12: Contours of mean Sigma on some of the planes shown in Fig. 5.8.

ejected from the nozzle and slowed down by the surrounding stagnating air, but it is the airflow itself that drags it away from the prefilmer. Therefore, the time-averaged contours of Σ do not to reveal anything about the intact length, since they are merely related to the residence time of liquid at a certain distance from the prefilmer. The closer to the injector,

the higher the residence time due to the liquid accumulation. Probably, some contours of $\overline{\alpha}_l$ would lead to the same observation. Conversely, the plots of the SMD shown above allow to overcome this issue by weighting the amount of interface with the averaged quantity of liquid, helping to estimate the region where the primary breakup occurs.

5.4.3 Curvature evolution

Once that SMD was computed, a step forward would be to extract the spray size distribution: to this aim the curvature of the liquid/gas interface is firstly analyzed. In Fig. 5.13, the curvature distribution is plot over the two instantaneous iso-surfaces already presented in Fig. 5.9. The grey colour identifies the flat sections of the interface, that are mainly

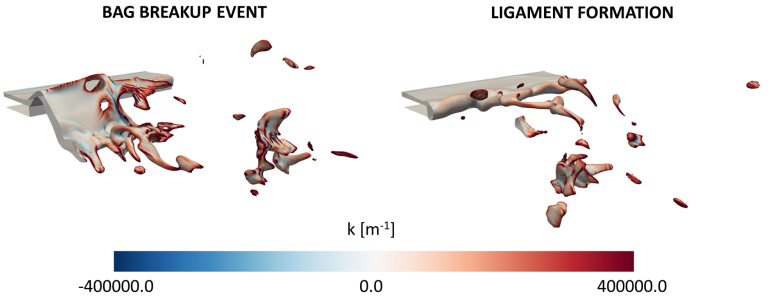

Figure 5.13: Curvature contour on iso-surfaces of $\alpha_l = 0.5$. Bag breakup event on the left, ligamfigent formation on the right.

located over the prefilmer and in some points over the bag (on the left). As expected, red (positive curvature, convex) zones are present where droplets or ligaments are formed, with a darker colour for smaller entities characterized by a larger curvature. It is important to note that also some blue points are visible, where concave surfaces are formed: even small entities, already detached from the prefilmer, can present some concave parts.
Compared to the classical diameter-based description of the spray, a characterization based on curvature allows to continuously analyze the evolution of the liquid, from the initial dense region down to the final formation of dispersed droplets.
In Fig. 5.14, the probability density function of the amount of interface

in classes curvature is plotted for the boxes shown in Fig. 5.8. For the sake of brevity, from now on this kind of plot will be referred as *Surface Curvature Distribution* (SCD) plot. Again, it is worth recalling that only the flow inside the region with the fine mesh is considered (see again Fig. 5.7 and 5.8). In order to better understand the ratio of the surface

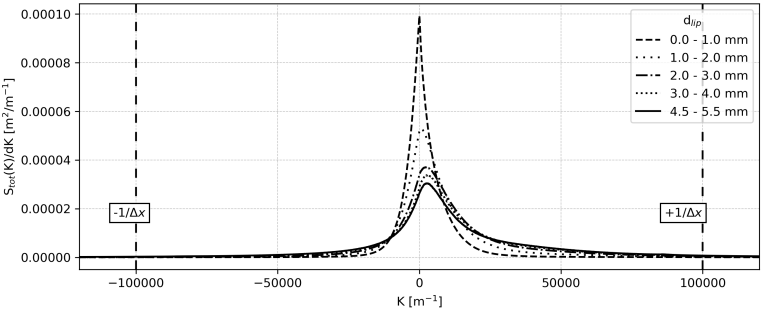

Figure 5.14: Probability density function of the amount of interface per classes of curvature (SCD) for four different boxes at a different distance from the prefilmer edge.

characterized by negative and positive curvature, also the cumulative function of the SCD is reported in Fig. 5.15 for the considered post-processing locations. In the first box, which extends from 0.00 up to 1.00 mm from the prefilmer edge, the peak of surface distribution is located close to k = 0 m^{-1}, meaning that most of the surface is actually flat. Also, both negative and positive values can be observed, which implies that both concave and convex structures can be identified in this area. From Fig. 5.15, it can be observed that they carry almost the same amount of interface, since its cumulative function reports that about the 50% of the total surface can be found for $k \leq 0$ m^{-1}.
Moving the attention 1.00 mm forward the peak moves to a slightly positive value of k, and the positive side presents a larger amount of surface. This is consistent with the advance of the atomization process. Some structures detach from the prefilmer trailing edge and due to the surface tension they tend to reshape into convex.
This trend is confirmed also at the two successive locations (2.00 - 3.00 mm and 3.00 - 4.00 mm), where the peak further moves towards positive values and there is a slight increase in the amount of surface associated with positive values. Moreover, the distribution gets wider and wider,

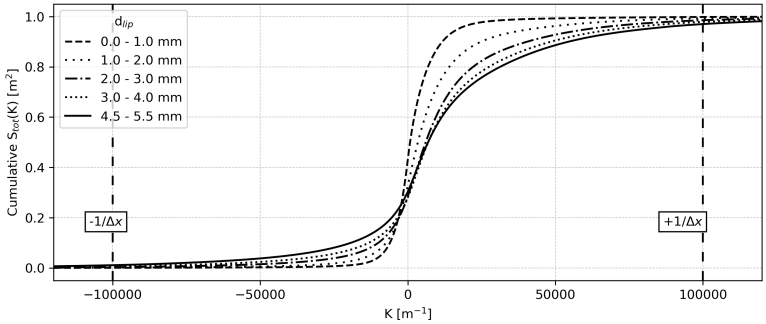

Figure 5.15: Cumulative function of the amount of interface per classes of curvature (SCD) for four different boxes at a different distance from the prefilmer edge.

meaning that more and more surface is *transported* by liquid structures with a larger curvature (both negative and positive). This implies that atomization is occurring and smaller entities are generated, which is also consistent with the observations made in the previous section regarding the SMD.

At the end of the refined zone, thus from 4.50 to 5.50 mm of distance from the injector, the farthest SCD is plotted in Fig. 5.14. While the position of the peak is almost the same of the previous stage, a small tendency can still be seen in the widening of the distribution which was already associated with the presence of smaller structures. Anyway, the similarities with the two previous sampling locations imply that the atomization process is not strongly progressing anymore after 3.00 mm. It is impossible to perfectly define when primary breakup ends, but now it is possible to determine where most of it takes place. It was decided to use the last box (4.50 - 5.50 mm) to further continue the analysis on curvature distribution. To this stage, the SMD value computed at the plane at 5.00 mm was associated (as in [107]), which lies in the middle of the considered box. A different distance can be considered but, given the small variations after 3.00 mm in both the SMD (Sec. 5.4.2) and in the SCD, the effect should be negligible.

5.5 Analysis of the curvature distribution

In the previous sections, the direct description of the spray formation during the primary breakup was accomplished through the measurement of the SCD. However, the SCD is not the traditional method to characterize the spray and it is much more common to use the NDF that provides the number of droplets for each class of diameter. From a technical point of view the NDF is more relevant, as most of the industrial applications are interested in a fully atomized spray. In fact, it is appropriate when the liquid phase is composed of a discrete droplets and each one of these can associated with a single class in terms of diameter. But it is not directly applicable to any zone of the spray that is not a sphere: ligaments, liquid sheets or even oscillating droplets theoretically require some integral process to determine the associated diameter. Recent work [128] has shown the advantage to determine the diameter of any object homeomorphic to a sphere by using topological invariants in the geometry through the Gauss-Bonnet formula. This proposal is very promising but still under development: for the time being, a simpler approach is proposed to build a NDF from the SCD.
As described in Sec. 5.2.2, the NDF can be obtained by transforming the classes of k into classes of diameter: $d_k = 4/k$ under the spherical assumption. Then, the number of droplets for each class can be computed using the amount of surface $\Sigma\, dv = (\Sigma_{min} + \Sigma^{'})\, dv$. However, it was verified that the NDF does not vary substantially if only Σ_{min} is considered, since $\Sigma^{'}$ is small in this case. In a fully atomized spray, composed only by actually spherical droplets this would be sufficient to derive the NDF. In this case, some liquid entities still present some deformed shape, characterized by a locally negative curvature. In a raw way, negative values were simply discarded in this thesis, but this point will be the object of future work within the research group. In a similar way, liquid structures with a very low curvature (e.g., a flat surfaces) populate the NDF with very large droplets. In this case they are not relevant in number, but they still influence the SMD computed through curvature. It is possible that such structures are generated by the sporadic passage of detached large ligaments through the sampling box. An engineering approach is applied then: the NDF was clipped at very high diameters using the SMD computed with Σ shown in Sec. 5.4.2. Following this procedure, in Fig. 5.16 the NDF of the spray is finally shown. The size of droplets varies from 20 μm up to 400 μm, with a large presence of smaller droplets, below 150 μm. At this stage, the NDF can be used in a separate Eulerian-Lagrangian simulation to improve the reliability of a simulation

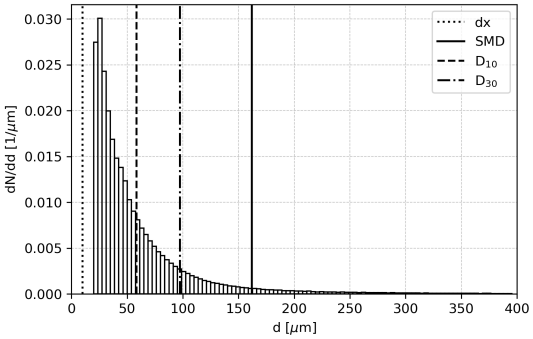

Figure 5.16: Final NDF applying the described post-processing procedure.

under altitude relight conditions, as specified in the previous chapter of this thesis.
Finally, Tab. 5.2 reports a quantitative comparison against the experimental data. An interesting agreement can be pointed out, although

	Experimental	Σ	k clipped
$SMD\,[\mu m]$	161.00	162.03	161.94
$d_{10}\,[\mu m]$	56.80	-	58.35
$d_{30}\,[\mu m]$	97.55	-	97.49
Limits $[\mu m]$	-	-	0.0 - 396.83
Location	full window	plane at 5.00 mm	box from 4.5 to 5.5 mm

Table 5.2: Summary of the main diameters.

some differences already discussed in the post-processing technique may impair such comparison. Indeed, the SMD derived from k was forced to be the same from Σ by cutting the tail of the NDF. Instead, both d_{10} and d_{30} are comparable between experiments and numerical simulation: this suggest that the present method can be improved to remove some raw assumptions, but the overall shape of the NDF is well captured with respect to the experimental one.
Finally, in Fig. 5.17 a sensitivity to the clipping diameter of the NDF is reported. It can be observed that it has quite a large effect on the SMD, whereas the d_{30} and, especially, the d_{10} are not strongly affected by the clipping diameter selection. This result highlight the need of an

alternative approach to estimate the SMD, which in this work was based on the analysis of Σ.

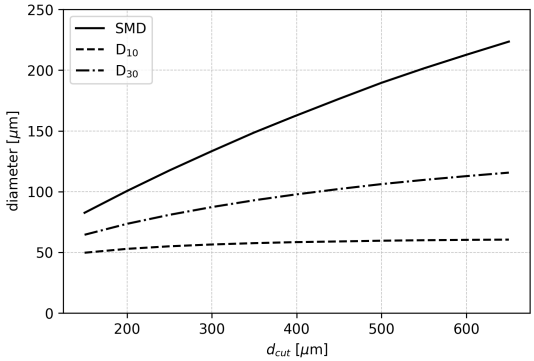

Figure 5.17: Sensitivity of the main diameters to the diameter selected to clip the tail of the NDF.

5.6 Conclusions to Chapter 5

In this chapter, the numerical investigation of a prefilming airblast atomizer was carried out using the coupled ICM-ELSA approach and applying a novel technique to post-process the results based on distributed variables such as the curvature of the liquid interface.
At first, a brief qualitative analysis was carried out, highlighting the fundamental mechanisms of breakup in the considered test case.
Then, the SMD was obtained over discrete planes thanks to the density of interface and the liquid volume fraction. It was shown that most of the SMD reduction (representing the atomization process) took place within the first planes, whereas a sort of plateu was reached downstream. This seems to indicate that the breakup process was already finalized at a given distance from the accumulation point. The value reached in such plateau was also in good agreement with the experimental data, although the reader is warned of possible inconsistencies between the two post-processing procedures.
Later, interface curvature was introduced: both negative and positive values were found, indicating the presence of both convex and concave sections of surface. Closer to the atomizer, the reported distribution was

almost symmetrical and very narrow. Here the peak was located close to $k = 0$, meaning that most of the surface is flat. Downstream, the peak of the PDF moved towards positive values, because of the liquid detachment from the prefilmer trailing edge and progressive reshaping into convex entities. At the same time, the distribution became wider and wider, since more and more droplets of a smaller diameter were created. This is consistent with the progress of the atomization process and with the conclusions drawn thanks to the SMD in the previous section.
Finally, a first attempt to recover the spray NDF was tested, although some improvements are still necessary. Starting from the interface distribution per classes of curvature, negative curvature values were discarded. At this stage, the conversion from SCD to NDF was carried out. The resulting NDF had a quite large SMD, because of a few droplets with very large diameter. In this work, this issue was addressed by clipping the tail of the NDF with the SMD value obtained with Σ. Although questionable, the proposed method provided good results in terms of representative diameters if compared against experimental data.
Future work will be addressed to further validate the approach, for instance by investigating different geometrical configurations or studying different operating conditions reported in Ch. 4.

Conclusions

The design of modern combustion chambers for aero engines cannot exclude a proper evaluation of the altitude relight performances. This is a complex task that can benefit from the use of CFD to reduce the cost of the experimental tests. In this work, a set of numerical tools were presented to tackle different aspects of this problem.
In Ch. 1, the governing equations required to simulate the ignition process were presented. In the attempt of including as much physics as possible, a LES framework was selected. Turbulence and combustion models were used for the sub-grid part of these two phenomena. Similarly, specific models were employed for spray and spark modelling. The study of the KIAI-CORIA rig (Ch. 3) showed that such setup is able to provide a sufficiently accurate prediction of the ignition. Even if many efforts may still be devoted to improve some stages of kernel generation and flame growth, such approach seems to be ready for use in industrial applications. In fact, all the mechanisms leading to flame expansion and stabilization were correctly predicted, as well as the time required to ignite the chamber. Those outputs could be really useful in the final part of the design process, even if the cost of the simulation is still excessive at the beginning, when the geometry is not yet fixed.
In Ch. 2 the problem of ignition probability was faced. Although it can also be computed through brute force LES, the excessive computational effort required simple models to be developed. In this thesis the SPHINTIR model was selected and employed to investigate the KIAI-CORIA rig (Ch. 3). A decent agreement with the experimental data was shown, even if it was obtained with a fine tuning of some of the parameters of the model. After that, the model can be effectively used in the optimization of the spark location in the combustion chamber.
In Ch. 4 the additional issue of spray atomization was analyzed separately. Under altitude relight conditions, the atomization quality is poor and the evaporation rates are quite low. Therefore, the spray is able to travel inside

the combustion chamber until it reaches the confinement. This makes the altitude relight simulations quite sensitive to the initial conditions used to inject the spray. Improved injection strategies are therefore needed to achieve a more realistic prediction.
To this aim, in Ch. 5 an innovative approach was developed, which exploits the density of interface and the interface curvature to compute the NDF at the end of primary breakup. The new strategy, composed by the use of the ELSA model and by an advanced post-processing technique, was validate on a planar prefilmer airblast atomizer. Although many points still need further attention, the strategy seems to be quite effective in retrieving the spray size distribution at the end of the primary breakup.
To conclude, two approaches were successfully used to simulate the ignition process and provide reliable results under ambient conditions. Conversely, it was shown that the liquid fuel distribution may fundamentally impair a possible altitude relight simulation. Therefore, the development of improved approaches for liquid phase handling is needed.
The obvious development of this thesis consists in the validation of all the proposed methods under altitude relight conditions. This future activity should be started backwards, namely from the prediction of the spray initial conditions following the strategy identified in Ch. 5. Quite close operating conditions are found under altitude relight for what concerns the primary atomization. Therefore, it is believed that such simulation should be easily accomplished with a very similar setup and without any further model development effort. Conversely, additional issues must be expected regarding the ignition simulations. In fact, as seen in Ch. 4, the evaporation rate is weak in altitude relight conditions and the effort to model the spray could be relevant. Moreover, the formation of a film of fuel at the walls of the combustor could be important for the ignition and should be carefully included. Finally, ignition simulations should take into account multiple spark attempts, which are fundamental to enable the flame onset under non-favourable ambient conditions. At the present day, no experimental data are available to this purpose (except for some preliminary results on the ISCAR rig presented in Ch. 4), but once available this work could really represent a starting point for a comprehensive approach to design burners optimized for the altitude relight.

Appendix 1

The main advantage of using a commercial solver for the implementation of the SPHINTIR model is the possibility to exploit the pre-existing Lagrangian tracking framework. However, only traditional models are available to track the more common classes of dispersed phases (e.g. fuel droplets, pulverized coal, solid pollutants and so on) and the equations previously shown must be implemented from scratch (step 4 of Sec. 2.4). This was accomplished using User Defined Functions, which allow to modify parts of the code as required by the user. In particular:

- `DEFINE_DPM_DRAG` was used to implement the first term related to the base solution velocity in Eq. 2.6.
- `DEFINE_DPM_BODY_FORCE` instead was exploited to mimic the second randomized term in Eq. 2.6.
- `DEFINE_DPM_LAW` was implemented to solve Eq. 2.7 using a custom scalar to assign the ξ_p variable to tracked particle.

Moreover, additional UDFs were required to manage the single run. The initialization of the spark volume (step 2 of Sec. 2.4) was implemented with a `DEFINE_ON_DEMAND`. The injection of flame particles (step 3 of Sec. 2.4) was handled with a `DEFINE_DPM_INJECTION_INIT` whereas the extinction criterion based on Ka (step 5 of Sec. 2.4) was implemented through a `DEFINE_DPM_SCALAR_UPDATE`. Since nothing in the setup must be changed, a single ANSYS Fluent session was used for a single spark location. Therefore, a `DEFINE_EXECUTE_AT_END` was employed to restart the simulation several times, (thus repeating the steps 2 to 5). An additional `DEFINE_ON_DEMAND` was used to read the external files used to set up the model.
Another advantage of using ANSYS Fluent was the easier interpolation from the *base* simulation to the dedicated grid for ignition probability, since both simulations were carried out within the same software (step 1

of Sec. 2.4).
In this way, a single run was carried out, which is sufficient to determine the ignition probability in a unique spark location under certain conditions. To allow different spark positions to be tested or to carry out a sensitivity on tuning parameters, a dedicated job manager was developed in Python. Moreover, it allows a more efficient parallelization of the different runs. In fact, simulations can be natively run in parallel in ANSYS Fluent using domain decomposition, but this is not very efficient in this case because of the relatively low number of Lagrangian particles tracked and the absence of eulerian equations to be solved. Whereas, it is more efficient to run in parallel several single simulations, exploiting serial Fluent sessions. Moreover, the developed Python manager allows to automatically detect the end of a single run (the duration of a single run may differ) and launch a new one without requiring any user input and thus maximising the efficiency of the approach.
Additional UDFs and Python scripts were developed to prepare and post-process the simulations, but they are not described here for the sake of brevity.

Bibliography

[1] D. Bertini. *High-fidelity prediction of metal temperature in gas turbine combustors using a loosely coupled multiphysics approach.* PhD thesis, Università degli Studi di Firenze, 2019.

[2] EASA. Certification Specifications for Engines. Certification specifications, European Aviation Safety Agency, 2003.

[3] EASA. Turbine Engine Relighting In Flight. Certification Memorandum 1CM-PIFS-010 Issue 01, European Aviation Safety Agency, 2015.

[4] A. H. Lefebvre and D. R. Ballal. *Gas turbine combustion: alternative fuels and emissions.* CRC Press - Taylor & Francis Group, 2010.

[5] J. Marrero-Santiago. *Experimental study of lean aeronautical ignition. Impact of critical parameters on the mechanisms acting along the different ignition phases.* PhD thesis, Université de Normandie, 2018.

[6] R. W. Read, J. W. Rogerson, and S. Hochgreb. Flame Imaging of Gas-Turbine Relight. *AIAA Journal*, 48(9):1916–1927, sep 2010.

[7] L. Rye and C. Wilson. The influence of alternative fuel composition on gas turbine ignition performance. *Fuel*, 96:277–283, 2012.

[8] E. Mastorakos. Forced ignition of turbulent spray flames. *Proceedings of the Combustion Institute*, 36(2):2367–2383, 2017.

[9] R. H. Essenhigh, M. K. Misra, and D. W. Shaw. Ignition of coal particles: A review. *Combustion and Flame*, 77(1):3 – 30, 1989.

[10] E. Mastorakos. Ignition of turbulent non-premixed flames. *Progress in Energy and Combustion Science*, 35(1):57 – 97, 2009.

[11] M. Halstead, L. Kirsch, and C. Quinn. The autoignition of hydrocarbon fuels at high temperatures and pressures—fitting of a mathematical model. *Combustion and Flame*, 30:45 – 60, 1977.

[12] E. Mastorakos, T. Baritaud, and T. Poinsot. Numerical simulations of autoignition in turbulent mixing flows. *Combustion and Flame*, 109(1):198 – 223, 1997.

[13] D. B. Spalding. *Combustion and mass transfer: a textbook with multiple-choice exercises for engineering students*. Elsevier, 2013.

[14] T. Marchione, S. F. Ahmed, and E. Mastorakos. Ignition of turbulent swirling n-heptane spray flames using single and multiple sparks. *Combustion and Flame*, 2009.

[15] J. Marrero-Santiago, F. Collin-Bastiani, E. Riber, G. Cabot, B. Cuenot, and B. Renou. On the mechanisms of flame kernel extinction or survival during aeronautical ignition sequences: Experimental and numerical analysis. *Combustion and Flame*, 222:70–84, dec 2020.

[16] K. Miki, J. Schulz, and S. Menon. Large-eddy simulation of equilibrium plasma-assisted combustion in supersonic flow. *Proceedings of the Combustion Institute*, 32(2):2413 – 2420, 2009.

[17] G. C. Gebel, T. Mosbach, W. Meier, M. Aigner, and S. Le Brun. An Experimental Investigation of Kerosene Droplet Breakup by Laser-Induced Blast Waves. *Journal of Engineering for Gas Turbines and Power*, 135(2), 01 2013. 021505.

[18] F. Collin-Bastiani. *Modeling and Large Eddy Simulation of Two-Phase Ignition in Gas Turbines*. PhD thesis, Université de Toulouse, 2019.

[19] A. Neophytou and E. Mastorakos. Simulations of laminar flame propagation in droplet mists. *Combustion and Flame*, 156(8):1627–1640, 2009.

[20] A. Neophytou, E. S. Richardson, and E. Mastorakos. Spark ignition of turbulent recirculating non-premixed gas and spray flames: A model for predicting ignition probability. *Combustion and Flame*, 159(4):1503–1522, 2012.

[21] E. Garnier, N. Adams, and P. Sagaut. *Large Eddy Simulation for Compressible Flows*. Scientific Computation. Springer Netherlands, Dordrecht, 2009.

[22] T. Poinsot and D. Veynante. *Theoretical and numerical combustion*. Second edition, 2005.

[23] ANSYS Inc. *ANSYS Fluent 2019R1 Theory Guide*. 2019.

[24] F. Nicoud and F. Ducros. Subgrid-scale stress modelling based on the square of the velocity gradient tensor. *Flow, Turbulence and Combustion*, 62(3):183–200, Sep 1999.

[25] D. K. Lilly. A proposed modification of the Germano subgrid-scale closure method. *Physics of Fluids A: Fluid Dynamics*, 4(3):633–635, mar 1992.

[26] B. Cuenot. Gas Turbines and Engine Simulations. In *Advances in Chemical Engineering, Volume 49*, volume 49, pages 273–385. Elsevier Inc., 1 edition, 2016.

[27] O. Colin, F. Ducros, D. Veynante, and T. Poinsot. A thickened flame model for large eddy simulations of turbulent premixed combustion. *Physics of Fluids*, 12(7):1843–1863, jul 2000.

[28] J. P. Legier, T. Poinsot, and D. Veynante. Dynamically thickened flame LES model for premixed and non-premixed turbulent combustion. *Proceedings of the Summer Program, Centre for Turbulence Research*, 2000.

[29] F. Williams. *Combustion Theory: The Fundamental Theory of Chemically Reacting Flow Systems*. Addison-Wesley series in engineering science. Addison-Wesley Publishing Company, 1965.

[30] F. Charlette, C. Meneveau, and D. Veynante. A power-law flame wrinkling model for LES of premixed turbulent combustion Part I: Non-dynamic formulation and initial tests. *Combustion and Flame*, 2002.

[31] F. Charlette, C. Meneveau, and D. Veynante. A power-law flame wrinkling model for LES of premixed turbulent combustion Part II: dynamic formulation. *Combustion and Flame*, 131(1-2):181–197, oct 2002.

[32] D. Barré. *Numerical simulation of ignition in aeronautical combustion chambers*. PhD thesis, Université de Toulouse, 2014.

[33] D. Paulhiac. *Modélisation de la combustion d'un spray dans un bruleur aéronautique*. PhD thesis, Université de Toulouse, 2015.

[34] B. Franzelli, E. Riber, M. Sanjosé, and T. Poinsot. A two-step chemical scheme for kerosene–air premixed flames. *Combustion and Flame*, 157(7):1364–1373, jul 2010.

[35] G. Boudier, L. Gicquel, and T. Poinsot. Effects of mesh resolution on large eddy simulation of reacting flows in complex geometry combustors. *Combustion and Flame*, 155(1-2):196–214, oct 2008.

[36] E. Fernández-Tarrazo, A. L. Sánchez, A. Liñán, and F. A. Williams. A simple one-step chemistry model for partially premixed hydrocarbon combustion. *Combustion and Flame*, 147(1):32 – 38, 2006.

[37] E. Ranzi, A. Frassoldati, A. Stagni, M. Pelucchi, A. Cuoci, and T. Faravelli. Reduced Kinetic Schemes of Complex Reaction Systems: Fossil and Biomass-Derived Transportation Fuels. *International Journal of Chemical Kinetics*, 46(9):512–542, sep 2014.

[38] D. G. Goodwin, R. L. Speth, H. K. Moffat, and B. W. Weber. Cantera: An object-oriented software toolkit for chemical kinetics, thermodynamics, and transport processes. https://www.cantera.org, 2018. Version 2.4.0.

[39] S. A. Morsi and A. J. Alexander. An investigation of particle trajectories in two-phase flow systems. *Journal of Fluid Mechanics*, 55(02):193, sep 1972.

[40] D. Spalding. The combustion of liquid fuels. *Symposium (International) on Combustion*, 4(1):847–864, jan 1953.

[41] B. Abramzon and W. Sirignano. Droplet vaporization model for spray combustion calculations. *International Journal of Heat and Mass Transfer*, 32(9):1605–1618, sep 1989.

[42] W. E. Ranz and W. R. Marshall. Evaporation from drops. Parts I & II. *Chem. Eng. Progr*, 1952.

[43] M. Boileau. *Simulation aux grandes échelles de l'allumage diphasique des foyers aéronautiques*. PhD thesis, Université de Toulouse, 2007.

[44] H. Nomura, Y. Ujiie, H. J. Rath, J. Sato, and M. Kono. Experimental study on high-pressure droplet evaporation using microgravity conditions. *Symposium (International) on Combustion*, 26(1):1267–1273, jan 1996.

[45] L. Mazzei, S. Puggelli, D. Bertini, A. Andreini, B. Facchini, I. Vitale, and A. Santoriello. Numerical and Experimental Investigation on an Effusion-Cooled Lean Burn Aeronautical Combustor: Aerothermal Field and Emissions. *Journal of Engineering for Gas Turbines and Power*, 141(4), 11 2018. 041006.

[46] G. Lacaze, E. Richardson, and T. Poinsot. Large eddy simulation of spark ignition in a turbulent methane jet. *Combustion and Flame*, 156(10):1993–2009, oct 2009.

[47] T. X. Phuoc and F. P. White. Laser-induced spark ignition of CH4/air mixtures. *Combustion and Flame*, 119(3):203–216, 1999.

[48] D. Barré, L. Esclapez, M. Cordier, E. Riber, B. Cuenot, G. Staffelbach, B. Renou, A. Vandel, L. Y. Gicquel, and G. Cabot. Flame propagation in aeronautical swirled multi-burners: Experimental and numerical investigation. *Combustion and Flame*, 161(9):2387–2405, sep 2014.

[49] F. Collin-Bastiani, J. Marrero-Santiago, E. Riber, G. Cabot, B. Renou, and B. Cuenot. A joint experimental and numerical study of ignition in a spray burner. *Proceedings of the Combustion Institute*, 37(4):5047–5055, 2019.

[50] A. Tyliszczak and E. Mastorakos. LES/CMC Predictions of Spark Ignition Probability in a Liquid Fuelled Swirl Combustor. In *51st AIAA Aerospace Sciences Meeting including the New Horizons Forum and Aerospace Exposition*, number January, pages 1–11. American Institute of Aeronautics and Astronautics, jan 2013.

[51] L. Esclapez, E. Riber, and B. Cuenot. Ignition probability of a partially premixed burner using LES. *Proceedings of the Combustion Institute*, 35(3):3133–3141, 2015.

[52] Y. Tang, M. Hassanaly, V. Raman, B. Sforzo, and J. Seitzman. A comprehensive modeling procedure for estimating statistical properties of forced ignition. *Combustion and Flame*, 206:158–176, 2019.

[53] M. P. Sitte, E. Bach, J. Kariuki, H.-J. Bauer, and E. Mastorakos. Simulations and experiments on the ignition probability in turbulent premixed bluff-body flames. *Combustion Theory and Modelling*, 20(3):548–565, may 2016.

[54] M. Cordier, A. Vandel, B. Renou, G. Cabot, M. A. Boukhalfa, and M. Cazalens. Spark Ignition of Confined Swirled Flames: Experimental and Numerical Investigation. In *Volume 1A: Combustion, Fuels and Emissions*, page V01AT04A028. ASME, jun 2013.

[55] E. Machover and E. Mastorakos. Numerical Investigation of the Stochastic Behavior of Light-Round in Annular Non-Premixed Combustors. *Combustion Science and Technology*, 189(9):1467–1485, sep 2017.

[56] E. Machover and E. Mastorakos. Experimental and numerical investigation on spark ignition of linearly arranged non-premixed swirling burners. *Combustion Science and Technology*, 189(8):1326–1353, 2017.

[57] T. Soworka, M. Gerendas, R. L. G. M. Eggels, and E. Mastorakos. Numerical Investigation of Ignition Performance of a Lean Burn Combustor at Sub-Atmospheric Conditions. In *Volume 4A: Combustion, Fuels and Emissions*, page V04AT04A046. ASME, jun 2014.

[58] A. Eyssartier, B. Cuenot, L. Y. Gicquel, and T. Poinsot. Using LES to predict ignition sequences and ignition probability of turbulent two-phase flames. *Combustion and Flame*, 160(7):1191–1207, 2013.

[59] S. F. Ahmed and E. Mastorakos. Spark ignition of lifted turbulent jet flames. *Combustion and Flame*, 2006.

[60] A. Lang, R. Lecourt, and F. Giuliani. Statistical Evaluation of Ignition Phenomena in Turbojet Engines. In *Volume 2: Combustion, Fuels and Emissions, Parts A and B*, pages 985–992. ASME, oct 2010.

[61] R. Lecourt, G. Linassier, and G. Lavergne. Detailed Characterisation of a Swirled Air/Kerosene Spray in Reactive and Non-Reactive Conditions Downstream From an Actual Turbojet Injection System. In *Volume 2: Combustion, Fuels and Emissions, Parts A and B*, pages 185–194. ASME, jan 2011.

[62] L. Esclapez. *Numerical study of ignition and inter-sector flame propagation in gas turbine*. PhD thesis, Université de Toulouse, 2015.

[63] P. Ivancic, E. Luke, E. A. Hassan, T. Ombrello, and D. M. Peterson. Predicting Ignition Probability Using a Backwards-Time Integration Scheme. In *AIAA Scitech 2020 Forum*, number January, pages 1–17, Reston, Virginia, jan 2020. American Institute of Aeronautics and Astronautics.

[64] B. Sforzo, J. Kim, J. Jagoda, and J. Seitzman. Ignition probability in a stratified turbulent flow with a sunken fire igniter. *Journal of Engineering for Gas Turbines and Power*, 137(1), 2015.

[65] B. Sforzo and J. Seitzman. Modeling ignition probability for stratified flows. *Journal of Propulsion and Power*, 33(5):1294–1304, 2017.

[66] S. F. Ahmed. The probabilistic nature of ignition of turbulent highly-strained lean premixed methane-air flames for low-emission engines. *Fuel*, 134:97–106, 2014.

[67] D. Ballal and A. Lefebvre. Flame propagation in heterogeneous mixtures of fuel droplets, fuel vapor and air. *Symposium (International) on Combustion*, 18(1):321–328, 1981.

[68] A. Giusti, M. P. Sitte, G. Borghesi, and E. Mastorakos. Numerical investigation of kerosene single droplet ignition at high-altitude relight conditions. *Fuel*, 225(February):663–670, 2018.

[69] M. Amerighi. *Large Eddy Simulation of the ignition process of a lean spray flame*. Master thesis, Università degli Studi di Firenze, 2020.

[70] J. Marrero-Santiago, A. Verdier, C. Brunet, A. Vandel, G. Godard, G. Cabot, M. Boukhalfa, and B. Renou. Experimental Study of Aeronautical Ignition in a Swirled Confined Jet-Spray Burner. *Journal of Engineering for Gas Turbines and Power*, 140(2):021502, feb 2018.

[71] M. Cordier, A. Vandel, G. Cabot, B. Renou, and A. M. Boukhalfa. Laser-Induced Spark Ignition of Premixed Confined Swirled Flames. *Combustion Science and Technology*, 185(3):379–407, mar 2013.

[72] M. Cordier, A. Vandel, B. Renou, G. Cabot, M. A. Boukhalfa, L. Esclapez, D. Barré, E. Riber, B. Cuenot, and L. Gicquel. Experimental and Numerical Analysis of an Ignition Sequence in a Multiple-Injectors Burner. In *Volume 1A: Combustion, Fuels and Emissions*. American Society of Mechanical Engineers, jun 2013.

[73] F. Shum-Kivan, J. Marrero Santiago, A. Verdier, E. Riber, B. Renou, G. Cabot, and B. Cuenot. Experimental and numerical analysis of a turbulent spray flame structure. *Proceedings of the Combustion Institute*, 36(2):2567–2575, 2017.

[74] A. Verdier, J. Marrero Santiago, A. Vandel, G. Godard, G. Cabot, and B. Renou. Local extinction mechanisms analysis of spray jet flame using high speed diagnostics. *Combustion and Flame*, 193:440–452, jul 2018.

[75] I. A. Mulla, G. Godard, G. Cabot, F. Grisch, and B. Renou. Quantitative imaging of nitric oxide concentration in a turbulent n-heptane spray flame. *Combustion and Flame*, 203:217–229, may 2019.

[76] I. A. Mulla, G. Godard, and B. Renou. Instantaneous planar measurements of nitric oxide concentration in a turbulent n-heptane spray flame. *Combustion and Flame*, 208:451–471, oct 2019.

[77] I. A. Mulla and B. Renou. Simultaneous imaging of soot volume fraction, PAH, and OH in a turbulent n-heptane spray flame. *Combustion and Flame*, 209:452–466, nov 2019.

[78] J. Marrero-Santiago, A. Verdier, A. Vandel, G. Cabot, A. M. Boukhalfa, and B. Renou. Effect of injector spacing in the light-around ignition efficiency and mechanisms in a linear swirled spray burner. *Heat and Mass Transfer*, 55(7):1871–1885, jul 2019.

[79] H.-E. Albrecht, M. Borys, N. Damaschke, and C. Tropea. *Laser Doppler and Phase Doppler Measurement Techniques*. Springer Berlin Heidelberg, Berlin, Heidelberg, 2003.

[80] C. E. Willert and M. Gharib. Digital particle image velocimetry. *Experiments in Fluids*, 1991.

[81] B. Rossow. *Processus photophysiques de molécules organiques fluorescentes et du kérosène applications aux foyers de combustion : applications aux foyers de combustion.* PhD thesis, Université Paris Sud, 2011.

[82] K. Kohse-Höinghaus. Laser techniques for the quantitative detection of reactive intermediates in combustion systems. *Progress in Energy and Combustion Science*, 20(3):203–279, jan 1994.

[83] F. Nicoud, H. B. Toda, O. Cabrit, S. Bose, and J. Lee. Using singular values to build a subgrid-scale model for large eddy simulations. *Physics of Fluids*, 2011.

[84] S. Jerzembeck, N. Peters, P. Pepiot-Desjardins, and H. Pitsch. Laminar burning velocities at high pressure for primary reference fuels and gasoline: Experimental and numerical investigation. *Combustion and Flame*, 2009.

[85] A. Lefebvre and V. McDonell. *Atomization and Sprays, Second Edition.* 2017.

[86] F. Shum-Kivan. *Simulation aux Grandes Echelles de flammes de spray et modélisation de la combustion non-prémlangée.* PhD thesis, Université de Toulouse, 2017.

[87] E. W. Lemmon, M. O. McLinden, and D. G. Friend. *Thermophysical Properties of Fluid Systems.* NIST Chemistry WebBook, NIST Standard Reference Database Number 69. National Institute of Standards and Technology, Gaithersburg MD, 20899, 2019.

[88] T. Mosbach, R. Sadanandan, W. Meier, and R. Eggels. Experimental analysis of altitude relight under realistic conditions using laser and high-speed video techniques. In *Proceedings of the ASME Turbo Expo*, 2010.

[89] M. J. Denton, S. B. Tambe, and S. M. Jeng. Experimental investigation into the high altitude relight of a three-cup combustor sector. In *Proceedings of the ASME Turbo Expo*, 2018.

[90] S. R. Stow, M. Zedda, A. Triantafyllidis, A. Garmory, E. Mastorakos, and T. Mosbach. Conditional Moment Closure LES Modelling of an Aero-Engine Combustor at Relight Conditions. *Volume 2: Combustion, Fuels and Emissions, Parts A and B*, pages 75–89, 2011.

[91] M. Majcherczyk, N. Zarzalis, and F. Turrini. Influence of the Turbulence Length Scale and Intensity on Spark Ignition of Kerosene Jet-A1–Air Mixtures at High Altitude Relight Conditions. In *Volume 4A: Combustion, Fuels and Emissions*, volume 4A, pages 1–9. American Society of Mechanical Engineers, jun 2014.

[92] A.-D. Martinos. SOPRANO D3.5: IGNITION MEASUREMENTS W/O COOLING AT ATMOSPHERIC AND RELIGHT CONDITIONS. Technical report, KIT, 2018.

[93] A.-D. Martinos, L. Palanti, S. Harth, A. Andreini, N. Zarzalis, D. Trimis, and I. Vitale. Analysis of ignition processes at combustors for aero engines at high altitude conditions. In *Proceedings of the European Combustion Meeting – 2019, April 14-17, Lisboa, Portugal*, 2019.

[94] A.-D. Martinos. SOPRANO D3.6: IGNITION MEASUREMENTS WITH COOLING AT ATMOSPHERIC AND RELIGHT CONDITIONS. Technical report, KIT, 2020.

[95] A. Martinos, N. Zarzalis, and S. Harth. Analysis of Ignition Processes at Combustors for Aero Engines at High Altitude Conditions With and Without Effusion Cooling. In *Proceedings of ASME Turbo Expo 2020 Turbomachinery Technical Conference and Exposition*, Virtual, Online, 2020.

[96] F. Menter. Stress-blended eddy simulation (SBES)—A new paradigm in hybrid RANS-LES modeling. *Notes on Numerical Fluid Mechanics and Multidisciplinary Design*, 137:27–37, 2018.

[97] T. Lenzi, L. Palanti, A. Picchi, T. Bacci, L. Mazzei, A. Andreini, and B. Facchini. TIME-RESOLVED FLOW FIELD ANALYSIS OF EFFUSION COOLING SYSTEM WITH REPRESENTATIVE SWIRLING MAIN FLOW. *Journal of Turbomachinery*, pages 1–26, jan 2020.

[98] S. Gepperth, A. Müller, R. Koch, H. Bauer, T. Strömungsmaschinen, and K. Institut. Ligament and Droplet Characteristics in Prefilming Airblast Atomization. In *ICLASS 2012, 12th Triennial International Conference on Liquid Atomization and Spray Systems, Heidelberg, Germany, September 2-6, 2012*, 2012.

[99] L. Palanti. *Development of an evaporation model for the dense spray region in Eulerian-Eulerian multiphase flow simulations.* Master thesis, Università degli Studi di Firenze, 2017.

[100] S. Puggelli. *Towards a unified approach for Large Eddy Simulation of turbulent spray flames.* PhD thesis, Università degli Studi di Firenze, 2018.

[101] C. Dumouchel. On the experimental investigation on primary atomization of liquid streams. *Experiments in fluids*, 45(3):371–422, 2008.

[102] R. Reitz. *Atomization and other breakup regimes of a liquid jet.* PhD thesis, Princeton University, 1978.

[103] D. R. Guildenbecher, C. Lopez-Rivera, and P. E. Sojka. Secondary atomization. *Experiments in Fluids*, 46(3):371–402, 2009.

[104] G. Chaussonnet, S. Gepperth, S. Holz, R. Koch, and H. J. Bauer. Influence of the ambient pressure on the liquid accumulation and on the primary spray in prefilming airblast atomization. *International Journal of Multiphase Flow*, 125:103229, 2020.

[105] S. Gepperth, D. R. Guildenbecher, R. Koch, and H.-J. Bauer. Prefilming primary atomization: Experiments and modeling. In *ILASS – Europe 2010, 23rd Annual Conference on Liquid Atomization and Spray Systems, Brno, Czech Republic, September 2010*, 2010.

[106] S. Gepperth, R. Koch, and H.-J. Bauer. Analysis and Comparison of Primary Droplet Characteristics in the Near Field of a Prefilming Airblast Atomizer. In *Volume 1A: Combustion, Fuels and Emissions*. American Society of Mechanical Engineers, jun 2013.

[107] K. Warncke, S. Gepperth, B. Sauer, A. Sadiki, J. Janicka, R. Koch, and H.-J. Bauer. Experimental and numerical investigation of the primary breakup of an airblasted liquid sheet. *International Journal of Multiphase Flow*, 91:208–224, may 2017.

[108] D. Bertini, L. Mazzei, S. Puggelli, A. Andreini, B. Facchini, L. Bellocci, and A. Santoriello. Numerical and experimental investigation on an effusion-cooled lean burn aeronautical combustor: Aerothermal field and metal temperature. In *Proceedings of the ASME Turbo Expo*, 2018.

[109] B. Sauer, N. Spyrou, A. Sadiki, and J. Janicka. Numerical analysis of the primary breakup under high-altitude relight conditions applying the embedded DNS approach to a generic prefilming airblast atomizer. In *Proceedings of the ASME Turbo Expo*, volume 1 A, 2013.

[110] J. Anez, A. Ahmed, N. Hecht, B. Duret, J. Reveillon, and F. Demoulin. Eulerian–lagrangian spray atomization model coupled with

interface capturing method for diesel injectors. *International Journal of Multiphase Flow*, 113:325 – 342, 2019.

[111] A. Andreini, C. Bianchini, S. Puggelli, and F. X. Demoulin. Development of a turbulent liquid flux model for Eulerian-Eulerian multiphase flow simulations. *International Journal of Multiphase Flow*, 81:88–103, 2016.

[112] L. Palanti, S. Puggelli, A. Andreini, J. Reveillon, B. Duret, and F.-X. Demoulin. An implicit formulation to model the evaporation process in the ELSA framework. *Atomization and Sprays*, 29(12):1043–1069, 2020.

[113] M. Boger, D. Veynante, H. Boughanem, and A. Trouvé. Direct numerical simulation analysis of flame surface density concept for large eddy simulation of turbulent premixed combustion. *Symposium (International) on Combustion*, 27(1):917–925, jan 1998.

[114] S. S. Deshpande, L. Anumolu, and M. F. Trujillo. Evaluating the performance of the two-phase flow solver interFoam. *Computational Science & Discovery*, 5(1):014016, nov 2012.

[115] S. Braun, L. Wieth, S. Holz, T. F. Dauch, M. C. Keller, G. Chaussonnet, S. Gepperth, R. Koch, and H.-J. Bauer. Numerical prediction of air-assisted primary atomization using Smoothed Particle Hydrodynamics. *International Journal of Multiphase Flow*, 114:303–315, may 2019.

[116] R. Canu, S. Puggelli, M. Essadki, B. Duret, T. Menard, M. Massot, J. Reveillon, and F. X. Demoulin. Where does the droplet size distribution come from? *International Journal of Multiphase Flow*, 107:230–245, 2018.

[117] G. Kindlmann, R. Whitaker, T. Tasdizen, and T. Moller. Curvature-based transfer functions for direct volume rendering: methods and applications. In *IEEE Visualization, 2003. VIS 2003.*, pages 513–520, 2003.

[118] T. Ménard, S. Tanguy, and A. Berlemont. Coupling level set/VOF/ghost fluid methods: Validation and application to 3D simulation of the primary break-up of a liquid jet. *International Journal of Multiphase Flow*, 33(5):510–524, may 2007.

[119] E. Mohamed, D. Florence, de Chaisemartin Stéphane, L. Adam, M. Thibault, and M. Marc. Statistical modeling of the gas–liquid interface using geometrical variables: Toward a unified description of the disperse and separated phase flows. *International Journal of Multiphase Flow*, 120:103084, 2019.

[120] J. Brackbill, D. Kothe, and C. Zemach. A continuum method for modeling surface tension. *Journal of Computational Physics*, 100(2):335 – 354, 1992.

[121] K. Warncke, A. Sadiki, and J. Janicka. New insights in the role of turbulence for simulating primary breakup of prefilming airblast atomization. In *ILASS - Europe 2019, 29th European Conference on Liquid Atomization and Spray Systems*, number September, Paris, 2019.

[122] B. Sauer, A. Sadiki, and J. Janicka. Numerical Analysis of the Primary Breakup Applying the Embedded DNS Approach to a Generic Prefilming Airblast Atomizer. *The Journal of Computational Multiphase Flows*, 6(3):179–192, sep 2014.

[123] B. Sauer, A. Sadiki, and J. Janicka. EMBEDDED DNS CONCEPT FOR SIMULATING THE PRIMARY BREAKUP OF AN AIRBLAST ATOMIZER. *Atomization and Sprays*, 26(3):187–215, 2016.

[124] G. Chaussonnet, E. Riber, O. Vermorel, B. Cuenot, S. Gepperth, and R. Koch. Large Eddy Simulation of a prefilming airblast atomizer. In *ILASS – Europe 2013, 25th European Conference on Liquid Atomization and Spray Systems, Chania, Greece, 1-4 September 2013*, number September, pages 1–4, 2013.

[125] G. Chaussonnet, O. Vermorel, E. Riber, and B. Cuenot. A new phenomenological model to predict drop size distribution in Large-Eddy Simulations of airblast atomizers. *International Journal of Multiphase Flow*, 80:29–42, 2016.

[126] A. Kastengren, J. Ilavsky, J. P. Viera, R. Payri, D. Duke, A. Swantek, F. Z. Tilocco, N. Sovis, and C. Powell. Measurements of droplet size in shear-driven atomization using ultra-small angle x-ray scattering. *International Journal of Multiphase Flow*, 92:131–139, jun 2017.

[127] M. Battistoni, G. M. Magnotti, C. L. Genzale, M. Arienti, K. E. Matusik, D. J. Duke, J. Giraldo, J. Ilavsky, A. L. Kastengren, C. F.

Powell, and P. Marti-Aldaravi. Experimental and Computational Investigation of Subcritical Near-Nozzle Spray Structure and Primary Atomization in the Engine Combustion Network Spray D. *SAE International Journal of Fuels and Lubricants*, 11(4):2018–01–0277, apr 2018.

[128] E. Mohamed, D. Florence, d. C. Stéphane, L. Adam, M. Thibault, and M. Marc. Statistical modeling of the gas–liquid interface using geometrical variables: Toward a unified description of the disperse and separated phase flows. *International Journal of Multiphase Flow*, 120:103084, 2019.